Christian Kokail, BSc

Superconducting Properties of Novel High-Pressure Lithium-Sulfur Compounds predicted by Evolutionary Algorithms

MASTER'S THESIS

to achieve the university degree of

Diplom-Ingenieur

Master's degree programme: Technical Physics

submitted to

Graz University of Technology

Supervisor

Ass. Prof. Dr. Lilia Boeri

Institute of Theoretical and Computational Physics

Graz, October 2016

AFFIDAVIT

I declare that I have authored this thesis independently, that I have not used other than the declared sources/resources, and that I have explicitly indicated all material which has been quoted either literally or by content from the sources used. The text document uploaded to TUGRAZonline is identical to the present master‘s thesis.

Date

Signature

Abstract

The theoretical prediction of a superconducting transition temperature of 200 K in high-pressure sulfur-hydride (H_3S) [1], gave a considerable impulse to the design of novel superconductors by means of first-principles calculations. In this work, we investigate the high-pressure lithium-sulfur system up to pressures of 700 GPa [2]. We search for thermodynamically stable phases using methods from evolutionary crystal structure prediction. Furthermore, the superconducting properties of the individual compounds are investigated using density functional linear-response calculations. The simulations showed that, besides the known lithium-sulfide (Li_2S), several new stoichiometries are stable at pressures higher than 20 GPa. Many phases display a high-pressure electride-like behavior with electron-pair localization in the interstitial voids of the lattice. The tendency to interstitial electron localization is a consequence of the orthogonality condition of the valence states to the inner core states of lithium. Thus, this behavior is not observed in H_3S and related hydrogen-chalcogen compounds. The investigation of the electron-phonon properties of the Li-rich phases revealed that superconductivity is suppressed in most compounds, either due to very small electron-phonon coupling matrix elements or by an increased insulating behavior due to hybridization into the lithium p-orbitals. The most striking difference in the electron-phonon properties was observed between two cubic Li_3S compounds, thermodynamically stable in very different pressure regimes. In the simple cubic $Pm\bar{3}m$ phase (stable between 20 and 225 GPa), the relevant states involved in the superconducting pairing are localized in the interstitial space of the lattice. Thus, very small electron-phonon coupling matrix elements are observed. At pressures higher than 640 GPa, a face centered cubic $Fm\bar{3}m$ structure was identified as the stable one. Here, interstitial electron localization is suppressed due to the high coordination of the structure. An analysis of the electron-localization function shows an accumulation of electrons along the lithium-sulfur bonds, giving them a strong covalent character. This phase displays a critical temperature of 50 K at 640 GPa, which increases to 80 K at 500 GPa, where it could exist as a metastable phase [3].

Kurzfassung

Die theoretische Vorhersage von Hochdruck-Schwefelhydrid (H_3S), welches eine supraleitende Sprungtemperatur von 200 K aufweist [1], war ein wesentlicher Impuls für die Entwicklung neuer supraleitender Materialien auf der Grundlage von *Ab-initio*-Rechnungen. Diese Arbeit beschäftigt sich mit Hochdruck-Lithium-Schwefel-Verbindungen, welche bei einem äußeren Druck von bis zu 700 GPa thermodynamisch stabil sind [2]. Um stabile Phasen innerhalb des Lithium-Schwefel Systems aufzufinden, bedienen wir uns Methoden der evolutionären Kristallstrukturvorhersage. Die supraleitenden Eigenschaften der unterschiedlichen Verbindungen werden mittels Linear-Response-Rechnungen auf der Grundlage der Dichtefunktionaltheorie untersucht. Unsere Simulationen zeigen, dass neben dem wohlbekannten Lithiumsulfid (Li_2S), bei Drücken über 20 GPa, mehrere stabile Hochdruck-Stöchiometrien auftreten. Sehr viele der vorhergesagten Verbindungen zeigen ein elektridartiges Verhalten mit lokalisierten Elektronenpaaren in den interstitiellen Hohlräumen des Kristallgitters. Die Tendenz zur Elektronenpaarlokalisation hat ihren Ursprung in der Orthogonalitätsbedingung der Valenzzustände zu den Lithium-Kernzuständen, und ist daher in den Hochdruck-Chalkogenwasserstoffen wie H_3S nicht beobachtbar. Bei einem Großteil der Lithium-dominierten Verbindungen zeigte sich eine Unterdrückung der Supraleitung. Die Ursache hierfür liegt zum Teil in sehr kleinen Elektron-Phonon-Matrixelementen und zum Teil in einem verminderten metallischen Charakter aufgrund der Hybridisierung der Valenzelektronen in die Lithium p-Orbitale. Der markanteste Unterschied in den Elektron-Phonon-Eigenschaften wurde in zwei Hochdruckphasen der Li_3S-Stöchiometrie beobachtet, welche in sehr unterschiedlichen Druckbereichen stabil sind. In der einfach-kubischen $Pm\bar{3}m$-Phase (stabil zwischen 20 und 225 GPa), sind die relevanten Zustände welche an der supraleitenden Paarbildung beteiligt sind, in den interstitiellen Poren des Kristallgitters lokalisiert. Dieser Umstand führt zu geringer Elektron-Phonon-Kopplung und zu einer Unterdrückung der Supraleitung. Bei Drücken über 640 GPa wird eine kubisch-flächenzentrierte $Fm\bar{3}m$-Phase energetisch bevorzugt. Durch die hohe Koordination wird hier die interstitielle Lokalisation der Zustände unterdrückt. Eine Analyse der Elektronenlokalisierungsfunktion zeigt eine Akkumulation der Elektronen entlang der Lithium-Schwefel-Bindungen, wodurch diese einen starken kovalenten Charakter erhalten. Aufgrund dieser Eigenschaften zeigt diese Phase Sprungtemperaturen von 50 K bei einem Druck von 640 GPa, bzw. 80 K bei 500 GPa wo diese Verbindung metastabil existieren könnte [3].

Contents

List of Figures

Chapter 1

Introduction

The prediction of novel superconducting materials from first principles is one of the most challenging tasks within the field of computational material science. While the mechanism driving superconductivity in the cuprates and the iron-pnictides remains still unclear, the electron-phonon mechanism causing superconductivity in "conventional" materials is very well understood, and accessible by theoretical methods. In the last few years, considerable progress has been achieved using different crystal structure prediction techniques, in combination with ab-initio methods for calculating electron-phonon properties of solids. The rapid developments culminated in 2014, with the theoretical prediction of an ultra-dense phase of sulfur-hydride (H_3S), displaying a superconducting transition temperature (T_c) of 203 K at an external pressure of 200 GPa [1]. This broke the record T_c previously held by the cuprates. The discovery received an additional boost, when the theoretical results were confirmed experimentally by Drozdov *et.al.* in Dec. 2014 [4]. This was the first time in the history of superconductivity research that a superconducting material has been predicted completely by ab-inito methods, and later discovered by experiment. The results have risen the hope to attain room temperature superconductivity in hydrogen-dominated compounds, and inspired a lot of people among the community to put their efforts in the ab-inito design of novel materials.

While much progress has been made in discovering high-T_c conventional superconductors in the hydrogen-chalcogens and related compounds, superconductivity in hydrogen-free materials is a largely unexplored field. The aim of this thesis is the investigation of electron-phonon properties of high-pressure **lithium-sulfur** compounds. Lithium is the atom most similar to hydrogen in the periodic table. While other lithium compounds such as Li-H [5], Li-Be [6], Li-B [7] or Li-N [8] have been investigated by other authors, Li-S is a natural choice, because it permits a direct comparison with H-S. Lithium sulfide (Li_2S), which is the only compound known at ambient conditions, has attracted con-

siderable interest in the last few years, due to its potential use as a cathode material in Li-S battery applications [9, 10]. The high pressure behavior of the Li_2S antifluorite structure has been investigated to pressures up to 20 GPa [11]. Apart from this insights, no further high-pressure data on Li-S compounds are available.

This work is divided into four main parts: After the introductory chapter, **Chapter 2** gives an overview of the theoretical concepts for calculating electron-phonon properties of various crystal structures. The first part gives an introduction to density functional theory within the plane-wave pseudopotential framework, followed by a discussion of density functional perturbation theory. Finally, the effects of the electron-phonon interaction on superconductivity are examined in more detail by describing the basic concepts of Migdal-Eliashberg theory.

Chapter 3 gives a detailed description of the evolutionary crystal structure prediction technique, as implemented in the USPEX-code [12, 13, 14]. We discuss how the computational complexity of the crystal structure prediction problem can be reduced by application of intelligent variation operators and the introduction of intermediate local optimization steps. The prediction of thermodynamically stable stoichiometries within binary systems is discussed.

Chapter 4 contains the results of our evolutionary structure search within the Li-S system. We extensively describe the method used for finding thermodynamically stable structures and their associated stability regimes. Special attention will be given to the description of convergence properties in connection with the estimation of formation enthalpies. Finally, we summarize our predictions by discussing the high-pressure phase diagram of the Li-S system and by listing the structural properties of the different phases.

In **Chapter 5** the electron phonon properties of the predicted phases, calculated by density functional linear response methods, are summarized. We give a detailed explanation of the superconducting properties with reference to the unusual chemistry observed in many Li-S compounds. Electronic bands and electron-phonon spectral functions are calculated for the individual structures.

The present thesis is based on our work on high-pressure lithium-sulfur compounds which has been published as a Rapid-Communication in *Physical-Review-B* [2].

1.1 The discovery of high-T_c conventional superconductivity

The first theory of the superconductivity with considerable predictive power was the BCS-theory developed by Bardeen, Cooper and Schrieffer in 1957 [15]. Unlike the Ginzburg-Landau theory based on phenomenological second-order phase transitions [16], BCS theory provides a microscopic description of the superconducting state, regardless of the physical origin of the attractive interaction between the electrons [17]. A complete many-body theory of electron phonon mediated superconductivity based on thermodynamic Green's functions was derived by Migdal and Eliashberg [18, 19]. A detailed description of the ideas underlying Migdal-Eliashberg theory is given in section 2.3.2.

The discovery of ceramic oxide superconductors in 1986 [20] was a major landmark in superconductivity research. Very soon it became obvious that theories based on electron-phonon interaction are not appropriate for describing superconductivity, although phonons may still play an important role [21]. The same is also true for the very recently discovered iron-based superconductors [22, 23]. The record holder in the cuprate material class was identified as the compound $HgBa_2Ca_2Cu_3O_{8+\delta}$ achieving a critical temperature of 138 K at ambient pressure [24].

In 1968, Neil Ashcroft put forward the idea that molecular hydrogen may become a high-T_c conventional superconductor at ultra-high pressures [25]. This work can more or less be seen as the foundation of high-pressure superconductivity research. Indeed, more recent theoretical as well as experimental investigations support the idea of the appearance of a metallic high-T_c phase in compressed hydrogen, with critical temperatures close to room temperature [26, 27, 28, 29, 30]. The high critical temperatures are a consequence of high vibrational frequencies associated with the low mass of the hydrogen atoms, and the strong coupling of conduction electrons to the lattice vibrations. Another prediction by Ashcroft was that hydrogen compounds, sometimes used in hydrogen-storage applications, can attain superconductivity at pressures available in diamond anvil cell experiments [31].

So far, ultra-dense H_3S at 200 GPa remains the record holder for high-T_c conventional superconductivity in hydrogen compounds. It is now completely understood that the spectacular superconducting properties of this compound result from a "constructive interference" of Van-Hove singularities due to flat bands at the Fermi level, large electron phonon coupling matrix elements due to the presence of strong covalent bonds, and high vibrational frequencies due to the low mass of the hydrogen atoms accompanied by large anharmonic effects [32]. Shortly after the discovery of H_3S, superconductivity was found in com-

pressed phosphines, compatible with several metastable hydrogen-phosphorus compounds identified by ab-initio calculations [3, 33, 34, 35].

1.2 Superconductivity in lithium dominated materials

Lithium, being the first alkali-metal in the periodic table, can be considered a prototype free-electron metal at ambient conditions. The question if high-T_c conventional superconductivity can be attained in materials based on lithium, can partly be answered by analyzing the high-pressure behavior of elemental lithium. Although hydrogen and lithium belong to the same column in the periodic table, the presence of core states in lithium produces a totally different high-pressure behavior. The pioneering work of Neaton and Ashcroft [36] revealed that lithium does not follow the naive expectation to become even more free-electron-like at higher pressures. Instead, the electronic structure at high pressures differs significantly from the free-electron-like behavior. Recent theoretical as well as experimental investigations have shown, that with increasing pressure, lithium undergoes a metal to semiconductor to metal transition [37, 38, 39]. This behavior, completely different from hydrogen, is a consequence of increasing *s-p* hybridization and connected localization of valence electrons in the interstitial voids of the lattice [40]. As discussed in [41], lithium can be considered as a high-pressure electride phase.

In 2002, Shimizu *et.al* reported that lithium becomes a superconductor with a critical temperature of 20 K at 48 GPa [42]. This remarkable high value, compared to the transition temperature at ambient pressure, is a consequence of the departure of Li from the free-electron behavior with increasing pressure. The pressure induced *s-p* orbital mixing induces a deformation of the $2s$ Fermi surface, which develops more nested regions [43].

Pressure-induced superconductivity in lithium-dominated compounds has been observed theoretically and experimentally in Be_2Li [44], as well as in $CaLi_2$ [45, 46]. In Be_2Li the increasing electronic localization under pressure leads to a reduced effective dimensionality of the system. The critical temperature was calculated to 2.5 K at an external pressure of 80 GPa. $CaLi_2$ is a Laves-phase with a critical temperature of 1.1 K at ambient pressure [45]. This structure is made up of two elements (Ca and Li) which both display anomalies under pressure. Using evolutionary crystal structure prediction techniques, several new phases were observed at elevated pressures [46]. It was demonstrated that the critical temperature increases to 13 K at a pressure of approximately 80 GPa.

In this work, we investigate the high-pressure Li-S system using methods of evolutionary crystal structure prediction and linear-response calculations for the electron-phonon coupling. We will investigate how the unusual chemistry of lithium influences the superconducting properties of Li-S compounds. As it will turn out, the nature of the underlying core states in lithium produces a completely different behavior, hardly comparable to the sulfur hydrides. In lithium, the orthogonality condition of the valence states to the inner cores states forces the electrons into the interstices. Because superconductivity in high-pressure electride phases is a largely unexplored field, one of the objectives of this thesis is to give new insights on the origin of the superconducting properties of high-pressure alkali-metal compounds.

Chapter 2

Elelctron-Phonon Properties from First Principles

2.1 Introduction to Density Functional Theory

In this section we intend to provide a short overview over the basic concepts of Density Functional Theory (DFT) within the framework of the projected augmented wave method as it is implemented in the VASP-code [47, 48, 49, 50]. In the subsequent sections, pseudopotential methods are discussed, accompanied by a description of methods for sampling the Brilloin-zone for metallic systems.

2.1.1 The density variational principle

In its essential aspects, the following introduction to density functional theory follows the presentation of John Perdew and Stefan Kurth [51]. We start by introducing the many-body Schrödinger equation within the Born-Oppenheimer approximation. This so called adiabatic approximation argues that the effect of the dynamics of the nuclei on the electron quantum many-body problem can be neglected due to the large disparity between the mass of the electrons and the nuclear masses. Throughout the whole work, we will use Hartree atomic units ($\hbar = e = m_e = 1/(4\pi\epsilon_0) = 1$), as well as a shorthand notation for the

coordinates:

$$(\boldsymbol{r}_1\sigma_1,\boldsymbol{r}_2\sigma_2,\ldots,\boldsymbol{r}_N\sigma_N) \to \underline{\underline{\boldsymbol{r}}}$$
$$\sum_{\{\sigma_i\}} \int d^3r_1 d^3r_2 \cdots d^3r_N \to \int d\underline{\underline{r}}$$

The all-electron Hamiltonian within the adiabatic approximation consists of three terms:

$$\hat{\mathcal{H}} = \hat{\mathcal{H}}_{\text{el}} + \hat{\mathcal{H}}_{\text{el-el}} + \hat{\mathcal{H}}_{\text{el-ion}}. \tag{2.1}$$

The term $\hat{\mathcal{H}}_{\text{el}}$ represents the kinetic energy of the electrons:

$$\langle \underline{\underline{\boldsymbol{r}}}| \hat{\mathcal{H}}_{\text{el}} |\Psi\rangle = \left(-\frac{1}{2} \sum_{i=1}^{N} \nabla_i^2 \right) \Psi(\underline{\underline{\boldsymbol{r}}}), \tag{2.2}$$

$\hat{\mathcal{H}}_{\text{el-el}}$ represents the repulsive electron-electron interaction which, in real space, reads

$$\langle \underline{\underline{\boldsymbol{r}}}| \hat{\mathcal{H}}_{\text{el-el}} |\Psi\rangle = \left(\sum_{i,j<i} u(\boldsymbol{r}_i,\boldsymbol{r}_j) \right) \Psi(\underline{\underline{\boldsymbol{r}}}) \quad \text{where} \quad u(\boldsymbol{r}_i,\boldsymbol{r}_j) = \frac{1}{|\boldsymbol{r}_i - \boldsymbol{r}_j|}, \tag{2.3}$$

and $\hat{\mathcal{H}}_{\text{el-ion}}$ is the *external potential*, i.e. the interaction of the electrons with the ions of the lattice.

$$\langle \underline{\underline{\boldsymbol{r}}}| \hat{\mathcal{H}}_{\text{el-ion}} |\Psi\rangle = \left(\sum_{i=1}^{N} v(\boldsymbol{r}_i) \right) \Psi(\underline{\underline{\boldsymbol{r}}}) \quad \text{where} \quad v(\boldsymbol{r}_i) = -\sum_I \frac{Z_I}{|\boldsymbol{r}_i - \boldsymbol{R}_I|}. \tag{2.4}$$

Here Z_I are the atomic numbers and $\boldsymbol{R}_I$ denote the ion-coordinates. The central object in DFT is the electron density for one spin component, *i.e.* the probability density for finding any of the N electrons at position $\boldsymbol{r}$ with spin σ normalized to the total number of electrons in the system. In order to obtain this quantity, one has to sum up the contributions from all the electrons, integrating out the remaining $N-1$ coordinates from the other electrons:

$$n_\sigma(\boldsymbol{r}) = \int d\underline{\underline{r}}\, \Psi^*(\underline{\underline{\boldsymbol{r}}}) \left(\sum_{i=1}^{N} \delta(\boldsymbol{r} - \boldsymbol{r}_i)\delta_{\sigma\sigma_i} \right) \Psi(\underline{\underline{\boldsymbol{r}}}) \tag{2.5}$$
$$= N \sum_{\sigma_2 \ldots \sigma_N} \int d^3r_2 \cdots d^3r_N \, |\Psi(\boldsymbol{r}\sigma,\boldsymbol{r}_2\sigma_2,\ldots,\boldsymbol{r}_N\sigma_N)|^2. \tag{2.6}$$

Equation (2.6) descends from (2.5), because exchanging a pair of quantum numbers $\boldsymbol{r}\sigma$ just produces an irrelevant phase factor. Therefore, all contributions are equivalent. The total energy of the system is obtained from equation

(2.1) multiplying with $\langle\Psi|$ from the left side. The term $\langle\Psi|\,\hat{\mathcal{H}}_{\text{el-ion}}\,|\Psi\rangle$ can be simplified further:

$$E_{\text{el-ion}} = \langle\Psi|\,\hat{\mathcal{H}}_{\text{el-ion}}\,|\Psi\rangle = \sum_{i=1}^{N}\int d\underline{\underline{r}}\;\Psi^*(\underline{\underline{r}})v(\boldsymbol{r}_i)\Psi(\underline{\underline{r}}) = \int d^3r\,v(\boldsymbol{r})n(\boldsymbol{r}). \quad (2.7)$$

Here we used the trivial transformation

$$v(\boldsymbol{r}_i) = \sum_{\sigma}\int d^3r\,v(\boldsymbol{r})\delta(\boldsymbol{r}-\boldsymbol{r}_i)\delta_{\sigma\sigma_i}.$$

The term $n(\boldsymbol{r})$ in Eq. 2.7 represents the total density:

$$n(\boldsymbol{r}) = n_\uparrow(\boldsymbol{r}) + n_\downarrow(\boldsymbol{r})\ . \quad (2.8)$$

From (2.7), it is clear that $E_{\text{el-ion}}$ is a functional of the density ($E_{\text{el-ion}} = E_{\text{el-ion}}[n(\boldsymbol{r})]$), but this doesn't hold for E_{el} and $E_{\text{el-el}}$. However, if $|\Psi\rangle$ is a ground state of an arbitrary system, than E_{el}, $E_{\text{el-el}}$ and thus the total energy are functionals of n_σ. This is a direct consequence of the *Hohenberg and Kohn theorem* which is the foundation of density functional theory. According to this theorem, there is a one-to-one correspondence between the ground-state wave-function and the ground-state electronic charge density. Using this fact, following the approach from Levy [52], we can use the standard Rayleigh-Ritz variational principle to obtain an equivalent density variational principle. To this end the standard variational principle

$$E = \min_{\Psi}\frac{\langle\Psi|\,\hat{\mathcal{H}}\,|\Psi\rangle}{\langle\Psi|\Psi\rangle} \quad (2.9)$$

is modified introducing a two-step process. In the first step we consider all states $|\Psi\rangle$ which yield to given spin dependent densities n_σ, and minimize over those wavefunctions. For the numerator one obtains:

$$\min_{\Psi\to n_\uparrow,n_\downarrow}\langle\Psi|\,\hat{\mathcal{H}}\,|\Psi\rangle = \min_{\Psi\to n_\uparrow,n_\downarrow}\langle\Psi|\,(\hat{\mathcal{H}}_{\text{el}}+\hat{\mathcal{H}}_{\text{el-el}})\,|\Psi\rangle + \int d^3r\,v(\boldsymbol{r})n(\boldsymbol{r}). \quad (2.10)$$

In the minimization process above, we took benefit from the fact that all wavefunctions that yield the same $n(\boldsymbol{r})$ also yield to the same external potential $v(\boldsymbol{r})$. The first term on the right side in (2.10) defines the so called the universal functional $F[n_\uparrow,n_\downarrow]$ which does not depend of the system under study [51]:

$$F[n_\uparrow,n_\downarrow] = \min_{\Psi\to n_\uparrow,n_\downarrow}\langle\Psi|\,(\hat{\mathcal{H}}_{\text{el}}+\hat{\mathcal{H}}_{\text{el-el}})\,|\Psi\rangle = \langle\Psi^{\min}_{n_\sigma}|\,(\hat{\mathcal{H}}_{\text{el}}+\hat{\mathcal{H}}_{\text{el-el}})\,|\Psi^{\min}_{n_\sigma}\rangle\,, \quad (2.11)$$

where $|\Psi^{\min}_{n_\sigma}\rangle$ is the state which delivers the minimum for given densities n_σ. We end up with a energy density-functional that has to be minimized with

respect to all densities in order to obtain the ground-state. The variation is restricted to the condition that the particle number has to be conserved:

$$\frac{\delta}{\delta n_\sigma(\boldsymbol{r}')}\left\{F[n_\uparrow(\boldsymbol{r}),n_\downarrow(\boldsymbol{r})] + \int d^3r\, v(\boldsymbol{r})n(\boldsymbol{r}) - \mu\int d^3r\, n(\boldsymbol{r})\right\} = 0, \tag{2.12}$$

with a Lagrange multiplier μ that turns out to be the chemical potential of the system [51]. Equation (2.12) results into the Euler equations:

$$\frac{\delta F[n_\uparrow,n_\downarrow]}{\delta n_\sigma(\boldsymbol{r})} + v(\boldsymbol{r}) = \mu. \tag{2.13}$$

In the above formulation, we explicitly considered the spin dependence of the charge density. This formulation remains valid for a spin-dependent external potential, such as an external magnetic field.

2.1.2 An auxiliary noninteracting system

We consider an auxiliary system of N noninteracting electrons ($\hat{\mathcal{H}} = \hat{\mathcal{H}}_{\text{el}} + \tilde{\hat{\mathcal{H}}}$) with

$$\tilde{\hat{\mathcal{H}}} = \sum_{i=1}^{N} \tilde{v}(\hat{\boldsymbol{r}}_i). \tag{2.14}$$

The single particle Schrödinger-equations for the orbitals $\psi_{\alpha\sigma}$ read:

$$\left(-\frac{1}{2}\nabla^2 + \tilde{v}(\boldsymbol{r})\right)\psi_{\alpha\sigma}(\boldsymbol{r}) = \varepsilon_{\alpha\sigma}\psi_{\alpha\sigma}(\boldsymbol{r}), \tag{2.15}$$

where α represents a set of quantum numbers and σ is a spin index. The spin-dependent density of such a system is given by

$$n_\sigma(\boldsymbol{r}) = \sum_\alpha f(\varepsilon_{\alpha\sigma})|\psi_{\alpha\sigma}(\boldsymbol{r})|^2, \tag{2.16}$$

in which $f(\varepsilon_{\alpha\sigma})$ denotes the occupation numbers which ensure that only states below the chemical potential are occupied. The universal functional of equation (2.10) reduces to

$$E_{\text{el}}^{(\text{non})}[n_\uparrow,n_\downarrow] = \min_{\Psi\to n_\uparrow,n_\downarrow} \langle\Psi|\,\hat{\mathcal{H}}_{\text{el}}\,|\Psi\rangle = \langle\Phi_{n_\sigma}^{\min}|\,\hat{\mathcal{H}}_{\text{el}}\,|\Phi_{n_\sigma}^{\min}\rangle\,. \tag{2.17}$$

and so the Euler equations (2.13) for the noninteracting system read

$$\frac{\delta E_{\text{el}}^{(\text{non})}[n_\uparrow,n_\downarrow]}{\delta n_\sigma} + \tilde{v}(\boldsymbol{r}) = \mu. \tag{2.18}$$

Because the system is non-interacting, $|\Phi^{\min}_{n_\sigma}\rangle$ can be written as a linear combination of Slater-determinants, constructed from single particle states $|\psi_{\alpha\sigma}\rangle$. In this case, it is easy to verify that the kinetic energy $E^{(\text{non})}_{\text{el}}$ can be written as the sum of the kinetic energy contributions from the occupied states:

$$E^{(\text{non})}_{\text{el}}[n_\uparrow,n_\downarrow] = \sum_{\alpha,\sigma} f(\varepsilon_{\alpha\sigma}) \int d^3r\, \psi^*_{\alpha\sigma}(\boldsymbol{r}) \left(-\frac{1}{2}\nabla^2\right) \psi_{\alpha\sigma}(\boldsymbol{r}). \tag{2.19}$$

In the next step we introduce the Hartree energy, that is the classical interaction energy of the charge distribution $n(\boldsymbol{r})$ [51]:

$$E_{\text{H}}[n(\boldsymbol{r})] = \frac{1}{2} \int d^3r d^3r'\, \frac{n(\boldsymbol{r})n(\boldsymbol{r}')}{|\boldsymbol{r}-\boldsymbol{r}'|}. \tag{2.20}$$

Taking the functional derivative with respect to the density, it can be verified that this produces the classical electrostatic potential of the charge distribution. Now, our intention is to express the total energy according to (2.10) using the quantities of the noninteracting system:

$$\begin{aligned} E &= (E_{\text{el}} + E_{\text{el-el}})[n_\uparrow,n_\downarrow] + E_{\text{el-ion}}[n] \\ &= E^{(\text{non})}_{\text{el}}[n_\uparrow,n_\downarrow] + E_{\text{H}}[n] + E_{\text{el-ion}}[n] + (E_{\text{el}} - E^{(\text{non})}_{\text{el}} + E_{\text{el-el}} - E_{\text{H}})[n_\uparrow,n_\downarrow] \\ &= E^{(\text{non})}_{\text{el}}[n_\uparrow,n_\downarrow] + E_{\text{H}}[n] + E_{\text{el-ion}}[n] + E_{\text{xc}}[n_\uparrow,n_\downarrow]. \end{aligned} \tag{2.21}$$

In equation (2.21), we defined the so called exchange-correlation energy E_{xc}. As it can be seen, E_{xc} is defined to include all the unknown effects omitted from the first three terms in (2.21). Using (2.13) we find

$$\begin{aligned} \mu &= \frac{\delta E^{(\text{non})}_{\text{el}}[n_\uparrow,n_\downarrow]}{\delta n_\sigma} + \frac{\delta E_{\text{H}}[n]}{\delta n_\sigma} + \frac{\delta E_{\text{xc}}[n_\uparrow,n_\downarrow]}{\delta n_\sigma} + v(\boldsymbol{r}) \\ &= \frac{\delta E^{(\text{non})}_{\text{el}}[n_\uparrow,n_\downarrow]}{\delta n_\sigma} + \underbrace{v_{\text{H}}[n] + v^\sigma_{\text{xc}}[n_\uparrow,n_\downarrow] + v(\boldsymbol{r})}_{v^\sigma_{\text{KS}}[n_\uparrow,n_\downarrow;\boldsymbol{r}]}. \end{aligned} \tag{2.22}$$

Comparing (2.22) to (2.18) yields an expression $\tilde{v}$ for the interacting system. Finally, we arrive at the so called Kohn-Sham equations of density functional theory:

$$\left(-\frac{1}{2}\nabla^2 + v^\sigma_{\text{KS}}[n_\uparrow,n_\downarrow;\boldsymbol{r}]\right) \psi_{\alpha\sigma}(\boldsymbol{r}) = \varepsilon_{\alpha\sigma}\psi_{\alpha\sigma}(\boldsymbol{r}). \tag{2.23}$$

In (2.22), we introduced the exchange-correlation potential $v^\sigma_{\text{xc}}[n_\uparrow,n_\downarrow]$. It is important to note that if the exact dependence upon the densities $n_\sigma(\boldsymbol{r})$ where known, equation (2.23) would predict the exact ground-state energy and

densities of the interacting many electron system. In practice, approximations have to be introduced for treating the exchange-correlation term (see below).

Equation (2.23) in combination with (2.16), represents a system of nonlinear differential equations that has to be solved self-consistently. The iteration process is started using a starting density $n_0(\boldsymbol{r})$, which can be an arbitrary strictly positive function, normalized to the total number of electrons in the system [53]. Usually, a linear combination of atomic densities is adopted.

In order to avoid instabilities during the iteration process, a linear mixing scheme is applied, instead of just taking the output density from the previous run. Let i be the actual iteration step, then the new density is obtained from:

$$n^{(i+1)} = \beta n^{(i)} + (1-\beta) n^{(i-1)}, \tag{2.24}$$

where β is chosen to be approximately 0.7. The self-consistency cycle is stopped if the values of $\left|E^{(i)} - E^{(i-1)}\right|$ or $\int d^3r \left|n^{(i)} - n^{(i-1)}\right|$ are falling below user-defined tolerances [53].

At the end of the self-consistency cycle, the obtained density can be used to calculate several groundstate expectation values. The most important turns out to be the total energy of the system, given by Eq. (2.21). This quantity can be used to calculate dynamical properties of the system (see sec. 2.2.1), or to select the lowest energy configuration from several others. In both cases, we have to add an additional term to the energy functional, taking into account the interaction energy of the ions:

$$E_{\text{ion-ion}}(\boldsymbol{R}_1, \boldsymbol{R}_2, \dots) = \sum_{I,J<I} \frac{Z_I Z_J}{|\boldsymbol{R}_I - \boldsymbol{R}_J|} \ . \tag{2.25}$$

Summing up the 2.25 for extended or periodic systems is a nontrivial task. Because of the long ranged Coulomb interaction the sum would converge exceedingly slow. A method widely used in quantum chemistry applications to bypass this problem is the Ewald summation [54, 55].

2.1.3 The exchange-correlation term

The exchange-correlation energy E_{xc} can be divided into two distinct parts, an exchange and a correlation term [51]:

$$E_{\text{xc}}[n_\uparrow, n_\downarrow] = E_{\text{x}}[n_\uparrow, n_\downarrow] + E_{\text{c}}[n_\uparrow, n_\downarrow], \tag{2.26}$$

where E_{x} is defined by

$$E_{\text{x}}[n_\uparrow, n_\downarrow] = \langle \Phi^{\min}_{n_\sigma} | \, \hat{\mathcal{H}}_{\text{el-el}} \, | \Phi^{\min}_{n_\sigma} \rangle - E_{\text{H}}[n] \tag{2.27}$$

which represents the analogue expression to the Hartree-Fock exchange energy [51]. The correlation energy can be calculated by inserting E_{x} into the expression for the total energy. One finds that

$$E_{\mathrm{c}}[n_{\uparrow},n_{\downarrow}] = \langle \Psi^{\mathrm{min}}_{n_\sigma}| \left(\hat{\mathcal{H}}_{\mathrm{el}} + \hat{\mathcal{H}}_{\text{el-el}}\right) |\Psi^{\mathrm{min}}_{n_\sigma}\rangle - \langle \Phi^{\mathrm{min}}_{n_\sigma}| \left(\hat{\mathcal{H}}_{\mathrm{el}} + \hat{\mathcal{H}}_{\text{el-el}}\right) |\Phi^{\mathrm{min}}_{n_\sigma}\rangle \,. \quad (2.28)$$

The great success of density functional theory based methods can be partly attributed to the fact that several very accurate approximations to E_{xc} are available. One of the most widespread approximations is based on the idea that each small fraction of the system contributes the same amount of exchange-correlation energy as an equivalent fraction of a homogeneous electron gas at the same density [56]. This is the so called local density approximation (LDA). In this work, more recently developed generalized gradient approximations (GGA) are applied, where the gradient of the density is taken into account. The most general expression for a GGA energy-functional reads as follows:

$$E^{\mathrm{GGA}}_{\mathrm{xc}}[n_{\uparrow},n_{\downarrow}] = \int d^3r \, f(n_{\uparrow}(\boldsymbol{r}),n_{\downarrow}(\boldsymbol{r}),\nabla n_{\uparrow}(\boldsymbol{r}),\nabla n_{\downarrow}(\boldsymbol{r})). \quad (2.29)$$

In this work, if not mentioned explicitly, we use the Perdew-Burke-Ernzerhof (PBE) exchange correlation functional [57].

2.1.4 Plane waves and pseudopotentials

In the following sections we discuss concepts related with the practical implementation of DFT-codes within the plane-wave pseudopotential scheme. For a more detailed description of the essential aspects, the reader is referred to the explanatory notes presented in [53]. In order to make the statements more clear, and because it is dispensable for the following representation, we will exclude the spin-index from the equations.

In order to solve the Kohn-Sham equations numerically, we have to expand the Kohn-Sham orbitals from equation (2.23), using an appropriate basis set. Because the systems studied in this thesis obey translational symmetry, a plane wave (PW) basis set is a natural choice. Moreover, according to Bloch's theorem, the Kohn-Sham orbitals can be written as a product of a plane wave and a lattice periodic function.

A complete and orthonormal PW basis is given by the set of functions

$$\langle \boldsymbol{r}|\boldsymbol{k}+\boldsymbol{G}\rangle = \frac{1}{\sqrt{V}} e^{i(\boldsymbol{k}+\boldsymbol{G})^T\boldsymbol{r}} \,. \quad (2.30)$$

where V is the crystal volume. In total, for the expansion of the Kohn-Sham orbitals we obtain

$$\psi_{\boldsymbol{k}n}(\boldsymbol{r}) = e^{i\boldsymbol{k}^T\boldsymbol{r}} \sum_{\boldsymbol{G}} c_{\boldsymbol{k}n}(\boldsymbol{G}) e^{i\boldsymbol{G}^T\boldsymbol{r}} \quad \text{with} \quad c_{\boldsymbol{k}n}(\boldsymbol{G}) = \frac{1}{V_\mathrm{u}} \int d^3r \, e^{-i(\boldsymbol{G}+\boldsymbol{k})^T\boldsymbol{r}} \psi_{\boldsymbol{k}n}(\boldsymbol{r}) \ , \tag{2.31}$$

in which n is the band-index, $\boldsymbol{k}$ the Bloch vector, $\boldsymbol{G}$ the reciprocal lattice vectors and V_u the volume of the unit cell. Obviously, it is not possible to employ an infinite PW basis set due to the limited computational resources. In practice, a cutoff energy E_cut has to be introduced such that the expansion (2.31) gets truncated at a wave vector that obeys $\frac{1}{2}|\boldsymbol{k}+\boldsymbol{G}|^2 < E_\mathrm{cut}$.

The wavefunctions describing the valence electrons of the system show strong oscillations in the vicinity of the ion cores due to the orthogonalization to the inner core states [58]. In order to describe these oscillations, an extremely large PW basis would be required, resulting in a high computational effort. In fact, the PW-expansion only becomes practicable, if the atomic *all-electron* potential is replaced by an appropriate *pseudopotential*, effectively eliminating the core states. Within this approximation, the wave functions inside a cutoff radius r_c around the ions are described by much smoother pseudo-wavefunctions, such that a drastically reduced basis set is required. This is a reasonable approximation because the inner core electrons are almost inert and only the valence electrons are chemically active [53]. However, especially at increased pressures where a significant core-valence overlap is present, one has to ensure to include the relevant states in the valence.

The most common pseudopotentials used in DFT applications are *norm conserving* [59] and *ultrasoft* pseudopotentials [60]. In the norm-conserving case, the potential is constructed in such a way, that inside the cutoff-radius r_c the norm of the pseudo wave function is the same to the norm of the corresponding all-electron wave function. In case of ultrasoft pseudopotentials, the norm-conservation condition is relaxed, resulting in larger cutoff-radii r_c and a smaller basis set. In general, a pseudopotential consists of a local and a non-local part [60, 56]:

$$\hat{v}^\xi_\mathrm{PP} = V^\xi_\mathrm{loc}(\hat{r}) + \sum_{nm} D^\xi_{nm} \, |\beta^\xi_n\rangle \, \langle\beta^\xi_m| \, , \tag{2.32}$$

in which the β^ξ_n as well as the coeffitients D^ξ_{nm} determine the pseudopotential for a specific atomic species labeled by ξ. The total electron-ion potential is the sum of all pseudopotentials of the individual atoms. Because of the projector term on the right hand side of equation (2.32), the external potentials acquires

a non-local form in real space [53]:

$$v(\boldsymbol{r},\boldsymbol{r}') = \sum_{l\kappa} v_{\mathrm{PP}}^{\xi}(\boldsymbol{r} - \boldsymbol{R}_l - \boldsymbol{\tau}_\kappa,\boldsymbol{r}' - \boldsymbol{R}_l - \boldsymbol{\tau}_\kappa,). \tag{2.33}$$

Here $\boldsymbol{R}_l$ are the real-space lattice vectors and $\boldsymbol{\tau}_\kappa$ are the coordinates of the atomic species ξ within the unit cell.

An alternative approach to the pseudopotential technique is provided by the *projector augmented-wave* (PAW) method. The method was introduced by Blöchl in 1994 [61], and is closely related to ultrasoft pseudopotentials [62]. In this work, in all calculations performed by the VASP-code, the PAW method was adopted.

Within the PAW method, real space is divided into *augmentation spheres*, centered on the positions of the atoms, labeled by a, and a bonding region between the spheres. One can show that it is possible to define a linear operator $\hat{\mathcal{T}}$, which transforms a set of *smooth* wave functions $\{|\tilde{\psi}_{\boldsymbol{k}n}\rangle\}$ into the real all-electron Kohn-Sham orbitals [63]:

$$|\psi_{\boldsymbol{k}n}\rangle = \hat{\mathcal{T}}\,|\tilde{\psi}_{\boldsymbol{k}n}\rangle\,. \tag{2.34}$$

This operator can be expressed as

$$\hat{\mathcal{T}} = \mathbb{1} + \sum_a \sum_i \left(|\phi_i^a\rangle - |\tilde{\phi}_i^a\rangle\right) \langle\tilde{p}_i^a| \tag{2.35}$$

in which the double sum on the right side has no effect outside the augmentation region, *i.e.* for $|\boldsymbol{r}-\boldsymbol{R}^a| > r_{\mathrm{c}}^a$ [63]. The *partial waves* $\{|\phi_i^a\rangle\}$ form a complete basis inside the spheres and are usually chosen to be eigenstates of the Schrödinger equation for an isolated atom [63]. The corresponding smooth partial waves $\{|\tilde{\phi}_i^a\rangle\}$ are expanded using an appropriate basis like Gaussians or spherical Bessel functions. The set $\{|\tilde{p}_i^a\rangle\}$ are some projector functions which satisfy

$$\sum_i |\tilde{\phi}_i^a\rangle \langle\tilde{p}_i^a| = \mathbb{1}. \tag{2.36}$$

Finally, using the transformation $\hat{\mathcal{T}}$, the Kohn-Sham equation for the smooth wave functions can be cast into the form of a generalized eigenvalue problem:

$$\hat{\mathcal{T}}^\dagger \hat{\mathcal{H}}_{\mathrm{KS}} \hat{\mathcal{T}}\,|\tilde{\psi}_{\boldsymbol{k}n}\rangle = \varepsilon_{\boldsymbol{k}n} \hat{\mathcal{T}}^\dagger \hat{\mathcal{T}}\,|\tilde{\psi}_{\boldsymbol{k}n}\rangle\,. \tag{2.37}$$

The gain of this additional complexity is that the $|\tilde{\psi}_{\boldsymbol{k}n}\rangle$ can be expanded using a comparatively small plane wave basis, which leaves us with a system of linear equations that have to be solved for a particular $\boldsymbol{k}$-point. In practice, the operators appearing in $\hat{\mathcal{H}}_{\mathrm{KS}}$, are transferred to reciprocal space by means of

fast fourier transform (FFT). The Hamiltonian is diagonalized using efficient iterative matrix diagonalization schemes. For a more detailed representation of the PAW-method, as well as for technical instructions on implementation, the reader is referred to [63].

By performing the Fourier transform of the potentials, it turns out that the local part of the pseudopotential, as well as the Hartree-potential diverge at $\boldsymbol{G} = 0$, so one has to exclude the $\boldsymbol{G}$,$\boldsymbol{G}' = 0$ terms from the plane wave expansion in equation (2.37) [53]. However, one can show that if the system is electrically neutral, the sum of the diverging terms is a constant independent of the electron density, hence it can be calculated at the beginning of the self-consistency cycle [53].

2.1.5 Sampling the Brillouin-zone

Due to the Born-van-Kàrmàn boundary conditions, the Bloch vector $\boldsymbol{k}$ is a quasi-continuous variable. In practice, the Kohn-Sham system (2.37) has to be solved for a discrete set of $\boldsymbol{k}$-points within the first Brillouin-zone (BZ). There are different methods for sampling the BZ. The two most common sampling methods are Γ-centered meshes, which include the Γ-point of reciprocal space, as well as Monkhorst-Pack meshes [64], which are shifted away from the origin. Within this approximation, integrals over the BZ are replaced by discrete sums over $\boldsymbol{k}$-points. Usually, the sums are performed over *irreducible* $\boldsymbol{k}$-points in the first BZ by including appropriate weighting factors $w_{\boldsymbol{k}}$. For the charge density this reads as follows:

$$\begin{aligned} n(\boldsymbol{r}) &= \frac{1}{V_{\mathrm{BZ}}} \int_{\mathrm{BZ}} d^3k \left[\sum_n f(\varepsilon_{\boldsymbol{k}n}) \, |\psi_{\boldsymbol{k}n}(\boldsymbol{r})|^2 \right] \\ &\rightarrow \sum_{\boldsymbol{k} \in \mathrm{IBZ}} \sum_n f(\varepsilon_{\boldsymbol{k}n}) w_{\boldsymbol{k}} |\psi_{\boldsymbol{k}n}(\boldsymbol{r})|^2, \end{aligned} \tag{2.38}$$

where V_{BZ} is the Brillouin-zone volume, and IBZ means *irreducible Brilloin-zone*.

The above description shows that within any plane wave DFT-code, there are two parameters that have to be fine-tuned for every calculation, which are the $\boldsymbol{k}$-points sampling and the cutoff energy for the PW expansion. In practice, one tunes this parameters until convergence with respect to the total energy is achieved.

A very important topic is the extension of the described plane wave DFT to metallic systems. For metals, sums over the irreducible part of the BZ converge exceedingly slowly with increasing number of $\boldsymbol{k}$-points. This has to do with the fact that the occupation numbers $f(\varepsilon_{\boldsymbol{k}n})$ drop discontinuously to zero for

eigenvalues above the Fermi level. One possible solution to this problem is to replace this step-function by a *smooth* function, similar to the finite temperature behavior of the Fermi-Dirac distribution. In this so called *smearing* approach, each Kohn-Sham energy value is broadened, so that the local density of states $N_{\mathrm{loc}}(\boldsymbol{r},\varepsilon)$ takes the form [56]:

$$N_{\mathrm{loc}}(\boldsymbol{r},\varepsilon) = \sum_{\boldsymbol{k}\in \mathrm{IBZ}} \sum_{n} \delta^{\sigma}(\varepsilon - \varepsilon_{\boldsymbol{k}n}) w_{\boldsymbol{k}} |\psi_{\boldsymbol{k}n}(\boldsymbol{r})|^2, \tag{2.39}$$

in which $\delta^{\sigma}(x) = \frac{1}{\sigma}\tilde{\delta}(x/\sigma)$ represents a smearing function that converges to the Dirac δ function as σ approaches zero [56]. $\tilde{\delta}(x)$ can be a an arbitrary function that integrates to one. Usually Gaussian-functions, or more sophisticated methods like Mathfessel-Paxton broadening are adopted [65]. The generalization of the electron density (2.38) to metallic systems can be obtained by integrating (2.39) to the Fermi-level [56]:

$$n(\boldsymbol{r}) = \int_{-\infty}^{\varepsilon_{\mathrm{F}}} d\varepsilon\, N_{\mathrm{loc}}(\boldsymbol{r},\varepsilon) = \sum_{\boldsymbol{k}\in \mathrm{IBZ}} \sum_{n} \Theta^{\sigma}(\varepsilon_{\mathrm{F}} - \varepsilon_{\boldsymbol{k}n}) w_{\boldsymbol{k}} |\psi_{\boldsymbol{k}n}(\boldsymbol{r})|^2, \tag{2.40}$$

where $\Theta^{\sigma}(x)$ is a "smeared out" version of the step function.

The most accurate method for dealing with the problem of Brillouin-zone integration in metals is the so called linear *tetrahedron-method* with Blöchl-corrections [66]. Here the term $\varepsilon_{\boldsymbol{k}n}$ is interpolated linearly between 2 $\boldsymbol{k}$-points. Corrections introduced by Blöchl *et.al.* remove the quadratic errors inherent in the linear interpolation scheme.

2.2 Linear response theory

In the following section we discuss how phonon- as well as electron-phonon properties can be obtained within *density functional perturbation theory* (DFPT) [56]. Electron-phonon properties contain the essential information for describing the properties of conventional superconductors, such as the superconducting gap or the critical temperature. The section starts with a summary of the phenomenological theory of phonons, followed by a description of how interatomic force constants are obtained by DFPT.

2.2.1 Phenomenological theory of lattice vibrations

Within the adiabatic approximation introduced in (2.1), only electrons are treated quantum mechanically. The total potential that the ions experience

is given by the energy contribution from the adiabatic Hamiltonian plus the interaction energy among the ions:

$$E_{\mathrm{BO}}(\underline{\boldsymbol{R}}) = E(\underline{\boldsymbol{R}}) + E_{\text{ion-ion}}(\underline{\boldsymbol{R}}). \tag{2.41}$$

Here $E_{\text{ion-ion}}$ was introduced in equation (2.25) and $\underline{\boldsymbol{R}}$ denotes the full ensemble of ion coordinates. $E_{\mathrm{BO}}(\underline{\boldsymbol{R}})$ is often referred to as the *Born-Oppenheimer energy surface* [56]. The atomic coordinates are described by

$$\boldsymbol{R}_{\kappa l} = \boldsymbol{R}_l + \boldsymbol{\tau}_\kappa + \boldsymbol{u}_{\kappa l}, \tag{2.42}$$

in which the $\boldsymbol{R}_l$ are the real space lattice vectors, the $\boldsymbol{\tau}_\kappa$ label the equilibrium positions of the κ-th atom in the unit cell and the $\boldsymbol{u}_{\kappa l}$ are the displacement-vectors from the equilibrium positions.

In the following, we expand the Born-Oppenheimer energy surface around the equilibrium positions of the ions ($\underline{\boldsymbol{u}} = 0$).

$$\begin{aligned} E_{\mathrm{BO}}(\underline{\boldsymbol{R}}) = E_{\mathrm{BO}}(\underline{\boldsymbol{R}})|_{\underline{\boldsymbol{u}}=0} + \sum_{l\kappa\alpha} \left.\frac{\partial E_{\mathrm{BO}}(\underline{\boldsymbol{R}})}{\partial u^\alpha_{\kappa l}}\right|_{\underline{\boldsymbol{u}}=0} u^\alpha_{\kappa l} \\ + \frac{1}{2} \sum_{\substack{l\kappa\alpha \\ l'\kappa'\alpha'}} \left.\frac{\partial^2 E_{\mathrm{BO}}(\underline{\boldsymbol{R}})}{\partial u^\alpha_{\kappa l} \partial u^{\alpha'}_{\kappa' l'}}\right|_{\underline{\boldsymbol{u}}=0} u^\alpha_{\kappa l} u^{\alpha'}_{\kappa' l'} + \cdots \end{aligned} \tag{2.43}$$

where the greek superscripts α and α' represent the cartesian components. The first derivative of the Born-Oppenheimer surface represents the components of the force acting on the atoms labeled by κl

$$F^\alpha_{\kappa l} = -\frac{\partial E_{\mathrm{BO}}(\underline{\boldsymbol{R}})}{\partial u^\alpha_{\kappa l}}. \tag{2.44}$$

The second term on the right side of equation (2.43) vanishes because the expression has to be evaluated at $\underline{\boldsymbol{u}} = 0$. The second order term in the expansion represents the matrix of the interatomic force constants. Since the system obeys translational invariance, the matrix can depend on the indices l and l' only through the difference of the lattice vectors [56]:

$$C^{\alpha\alpha'}_{\kappa\kappa',ll'} = \left.\frac{\partial^2 E_{\mathrm{BO}}(\underline{\boldsymbol{R}})}{\partial u^\alpha_{\kappa l} \partial u^{\alpha'}_{\kappa' l'}}\right|_{\underline{\boldsymbol{u}}=0} = C^{\alpha\alpha'}_{\kappa\kappa'}(\boldsymbol{R}_l - \boldsymbol{R}_{l'}). \tag{2.45}$$

The Fourier transform of this quantity can be written as the derivative with respect to the amplitudes related to a specific phonon wave vector $\boldsymbol{q}$ [56]:

$$C^{\alpha\alpha'}_{\kappa\kappa'}(\boldsymbol{q}) = \sum_l e^{-i\boldsymbol{q}^T \boldsymbol{R}_l} C^{\alpha\alpha'}_{\kappa\kappa'}(\boldsymbol{R}_l) = \frac{1}{N_\mathrm{c}} \left.{}^{-\boldsymbol{q}}\partial^\alpha_\kappa \, {}^{\boldsymbol{q}}\partial^{\alpha'}_{\kappa'} E_{\mathrm{BO}}(\underline{\boldsymbol{R}})\right|_{\underline{\boldsymbol{u}}=0}, \tag{2.46}$$

where we defined the operator ${}^{\boldsymbol{q}}\partial_\kappa^\alpha$ to act like:

$$ {}^{\boldsymbol{q}}\partial_\kappa^\alpha \equiv \sum_l e^{i\boldsymbol{q}^T\boldsymbol{R}_l}\frac{\partial}{\partial u_{\kappa l}^\alpha}. \tag{2.47} $$

In (2.46), N_c denotes the number of unit cells and the prefactor $1/N_\mathrm{c}$ corrects the error from the double summation inherent in (2.46). Eq. (2.47) defines a linear operator for which the standard rules of differentiation apply. The phonon dispersion $\omega_{\boldsymbol{q}\nu}$, where ν is the band index, can be obtained solving the eigenvalue problem for the *dynamical matrix* $D_{\kappa\kappa'}^{\alpha\alpha'}(\boldsymbol{q}) = C_{\kappa\kappa'}^{\alpha\alpha'}(\boldsymbol{q})/\sqrt{M_\kappa M_{\kappa'}}$, in which M_κ is the mass of the κ-th ion:

$$ \sum_{\kappa'\alpha'} D_{\kappa\kappa'}^{\alpha\alpha'}(\boldsymbol{q})c_{\kappa'}^{\alpha'}(\boldsymbol{q}\nu) = \omega_{\boldsymbol{q}\nu}^2 c_\kappa^\alpha(\boldsymbol{q}\nu). \tag{2.48} $$

Here, the $c_\kappa^\alpha(\boldsymbol{q}\nu)$ are the components of the eigenvectors associated to the node $\boldsymbol{q}\nu$. Eq. 2.48 comprises the full information of the phonon spectrum. It can be used to construct the partial phonon density of states for the κ-th atom in the unit cell:

$$ Z(\omega,\kappa\alpha) = \sum_{\boldsymbol{q}\nu} \delta_\sigma(\omega - \omega_{\boldsymbol{q}\nu})|c_\kappa^\alpha(\boldsymbol{q}\nu)|^2. \tag{2.49} $$

In order to obtain the dynamical matrix $D_{\kappa\kappa'}^{\alpha\alpha'}$ within DFT, we first look at the expression for the first derivative of the Born-Oppenheimer energy surface associated with a lattice displacement of wave vector $\boldsymbol{q}$:

$$ {}^{\boldsymbol{q}}\partial_{\kappa'}^{\alpha'} E_\mathrm{BO}(\underline{\boldsymbol{R}}) = \langle\Psi(\underline{\boldsymbol{R}})|\, {}^{\boldsymbol{q}}\partial_{\kappa'}^{\alpha'}\hat{\mathcal{H}}_\mathrm{BO}(\underline{\boldsymbol{R}})\,|\Psi(\underline{\boldsymbol{R}})\rangle\,, \tag{2.50} $$

where we used the Hellmann-Feynman theorem. The Born-Oppenheimer Hamiltonian depends on the atomic coordinates only through the electron-ion interaction term (2.7), and through the ion-ion interaction energy introduced in (2.25). Therefore, the derivative can be written as

$$ {}^{\boldsymbol{q}}\partial_{\kappa'}^{\alpha'} E_\mathrm{BO}(\underline{\boldsymbol{R}}) = \int d^3r\, n(\boldsymbol{r})\, {}^{\boldsymbol{q}}\partial_{\kappa'}^{\alpha'} v(\boldsymbol{r}) + {}^{\boldsymbol{q}}\partial_{\kappa'}^{\alpha'} E_\text{ion-ion}(\underline{\boldsymbol{R}}). \tag{2.51} $$

Finally, using expression (2.45) for the dynamical matrix, we obtain:

$$ \begin{aligned} D_{\kappa\kappa'}^{\alpha\alpha'}(\boldsymbol{q}) = \frac{1}{N_\mathrm{c}\sqrt{M_\kappa M_{\kappa'}}}\Bigg[&\int d^3r\,[{}^{\boldsymbol{q}}\partial_\kappa^\alpha\, n(\boldsymbol{r})]^*\, {}^{\boldsymbol{q}}\partial_{\kappa'}^{\alpha'} v(\boldsymbol{r}) \\ &+ \int d^3r\, n(\boldsymbol{r})\, {}^{-\boldsymbol{q}}\partial_\kappa^\alpha\, {}^{\boldsymbol{q}}\partial_{\kappa'}^{\alpha'} v(\boldsymbol{r}) + {}^{-\boldsymbol{q}}\partial_\kappa^\alpha\, {}^{\boldsymbol{q}}\partial_{\kappa'}^{\alpha'} E_\text{ion-ion}(\underline{\boldsymbol{R}})\Bigg]_{\underline{\boldsymbol{u}}=0}. \end{aligned} \tag{2.52} $$

This expression shows that, in order to obtain the dynamical matrix of the system, we need to calculate the linear response of the electron density to a distortion of the lattice geometry: ${}^{\boldsymbol{q}}\partial^{\alpha}_{\kappa}\, n(\boldsymbol{r})$. In order not to overburden the notation with indices, we did not indicate explicitly the dependence of $n(\boldsymbol{r})$ as well as of $v(\boldsymbol{r})$ on the atomic configuration. The linear response of the density and the external potential can be obtained by means of density functional perturbation theory [56].

2.2.2 Density Functional Perturbation Theory

In the following we will discuss the situation in which all electronic states are either full or empty *i.e.* the density of a spin degenerate system is given by

$$n(\boldsymbol{r}) = 2 \sum_{\boldsymbol{k}\,\in\,\mathrm{BZ}} \sum_{n=1}^{N/2} |\psi_{\boldsymbol{k}n}|^2, \tag{2.53}$$

where N is the total number of electrons and the sum over n extends over all occupied states. The extension to metallic systems requires a few more technical expedients, which are discussed at the end of this section.

The linear response of the density in equation (2.52), can be obtained applying ${}^{\boldsymbol{q}}\partial^{\alpha}_{\kappa}$ to (2.53):

$${}^{\boldsymbol{q}}\partial^{\alpha}_{\kappa}\, n(\boldsymbol{r}) = 4\,\mathrm{Re} \sum_{\boldsymbol{k}n} \psi^{*}_{\boldsymbol{k}n}(\boldsymbol{r})\, {}^{\boldsymbol{q}}\partial^{\alpha}_{\kappa}\, \psi_{\boldsymbol{k}n}(\boldsymbol{r}). \tag{2.54}$$

The variation of the orbital ${}^{\boldsymbol{q}}\partial^{\alpha}_{\kappa}\, \psi_{\boldsymbol{k}n}(\boldsymbol{r})$ is constructed through first-order perturbation theory:

$$|{}^{\boldsymbol{q}}\partial^{\alpha}_{\kappa}\, \psi_{\boldsymbol{k}n}\rangle = \sum_{m} \sum_{\boldsymbol{k}'\,\in\,\mathrm{BZ}} |\psi_{\boldsymbol{k}'m}\rangle\, \frac{\langle \psi_{\boldsymbol{k}'m}|\, {}^{\boldsymbol{q}}\partial^{\alpha}_{\kappa}\, \hat{v}_{\mathrm{KS}}\, |\psi_{\boldsymbol{k}n}\rangle}{\varepsilon_{\boldsymbol{k}n} - \varepsilon_{\boldsymbol{k}'m}}. \tag{2.55}$$

Here, ${}^{\boldsymbol{q}}\partial^{\alpha}_{\kappa}\, \hat{v}_{\mathrm{KS}}$ is the linear response of the Kohn-Sham potential to a lattice distortion with wave vector $\boldsymbol{q}$ [56]:

$${}^{\boldsymbol{q}}\partial^{\alpha}_{\kappa}\, \hat{v}_{\mathrm{KS}}[n;\boldsymbol{r}] = {}^{\boldsymbol{q}}\partial^{\alpha}_{\kappa}\, v(\boldsymbol{r}) + \int d^3r' \frac{{}^{\boldsymbol{q}}\partial^{\alpha}_{\kappa}\, n(\boldsymbol{r})}{|\boldsymbol{r} - \boldsymbol{r}'|} + \left.\frac{dv_{\mathrm{xc}}[n]}{dn}\right|_{n=n(\boldsymbol{r})} {}^{\boldsymbol{q}}\partial^{\alpha}_{\kappa}\, n(\boldsymbol{r}) \tag{2.56}$$

Eq. (2.56) is usually referred to as the *lattice-periodic scattering potential* [67]. Reinserting (2.55) into equation (2.53) leads to the following expression for the variation of the density:

$${}^{\boldsymbol{q}}\partial^{\alpha}_{\kappa}\, n(\boldsymbol{r}) = 4\,\mathrm{Re} \sum_{\substack{\boldsymbol{k}\boldsymbol{k}' \\ \in\,\mathrm{BZ}}} \sum_{n(\mathrm{occ.})m} \psi^{*}_{\boldsymbol{k}n}(\boldsymbol{r})\psi_{\boldsymbol{k}'m}(\boldsymbol{r}) \frac{\langle \psi_{\boldsymbol{k}'m}|\, {}^{\boldsymbol{q}}\partial^{\alpha}_{\kappa}\, \hat{v}_{\mathrm{KS}}\, |\psi_{\boldsymbol{k}n}\rangle}{\varepsilon_{\boldsymbol{k}n} - \varepsilon_{\boldsymbol{k}'m}}. \tag{2.57}$$

Because the sum over $\boldsymbol{k}$ extends over all Bloch vectors in the first BZ, terms with band indices originating from the manifold of occupied states cancel each other, due to the opposite sign from the denominator. Eq. (2.57) will be non-zero only if $|\psi_{\boldsymbol{k}'m}\rangle$ is an empty state, hence the sum over m can be restricted to the subspace of conduction states. Moreover, because of conservation of momentum, the Bloch vector of the final state in the transition matrix element appearing in Eq. (2.57), has to be equal to $\boldsymbol{k}' = \boldsymbol{k} + \boldsymbol{q} + \boldsymbol{G}$, where $\boldsymbol{G}$ is a reciprocal lattice vector [68]. In general, the normal scattering contributions ($\boldsymbol{G} = 0$) are larger than those from Umklapp-scattering, hence only the $\boldsymbol{k} + \boldsymbol{q}$ contribution survives from the sum over $\boldsymbol{k}'$ [56].

Instead of solving (2.57) directly, one can show that it is more convenient to calculate the variation of the Kohn-Sham orbitals through a system of linear equations [56]. To this end, one applies the operator $\hat{\mathcal{H}}_{\mathrm{KS}} - \varepsilon_{\boldsymbol{k}n}$ to the perturbed state (2.55), where the summation is restricted to the conduction space:

$$\begin{aligned}(\hat{\mathcal{H}}_{\mathrm{KS}} - \varepsilon_{\boldsymbol{k}n})\,|^{\boldsymbol{q}}\partial^{\alpha}_{\kappa}\,\psi_{\boldsymbol{k}n}\rangle &= -\underbrace{\sum_{m} |\psi_{\boldsymbol{k}+\boldsymbol{q}\,m}\rangle\,\langle\psi_{\boldsymbol{k}+\boldsymbol{q}\,m}|}_{\hat{P}_{\mathrm{c}}^{\boldsymbol{k}+\boldsymbol{q}}}\,{}^{\boldsymbol{q}}\partial^{\alpha}_{\kappa}\,\hat{v}_{\mathrm{KS}}\,|\psi_{\boldsymbol{k}n}\rangle \\ &= (\hat{P}_{\mathrm{v}}^{\boldsymbol{k}+\boldsymbol{q}} - \mathbb{1})^{\boldsymbol{q}}\partial^{\alpha}_{\kappa}\,\hat{v}_{\mathrm{KS}}\,|\psi_{\boldsymbol{k}n}\rangle\,,\end{aligned} \tag{2.58}$$

where $\hat{P}_{\mathrm{c}}^{\boldsymbol{k}+\boldsymbol{q}}$ and $\hat{P}_{\mathrm{v}}^{\boldsymbol{k}+\boldsymbol{q}}$ are projection operators on the conduction, respectively on the valence space, with respect to the $\boldsymbol{k} + \boldsymbol{q}$ manifold.

The left hand-side of equation (2.58) cannot be inverted directly because the operator therein has a vanishing eigenvalue. This problem can be fixed by adding a projection-operator on the valence space with respect to the $\boldsymbol{k} + \boldsymbol{q}$ manifold [56]. This term has no effect on the solution because $\hat{P}_{\mathrm{v}}^{\boldsymbol{k}+\boldsymbol{q}}\,|^{\boldsymbol{q}}\partial^{\alpha}_{\kappa}\,\psi_{\boldsymbol{k}n}\rangle = 0$, which is obvious from (2.55). The result is often called *Sternheimer equation*:

$$(\hat{\mathcal{H}}_{\mathrm{KS}} + \beta\hat{P}_{\mathrm{v}}^{\boldsymbol{k}+\boldsymbol{q}} - \varepsilon_{\boldsymbol{k}n})\,|^{\boldsymbol{q}}\partial^{\alpha}_{\kappa}\,\psi_{\boldsymbol{k}n}\rangle = (\hat{P}_{\mathrm{v}}^{\boldsymbol{k}+\boldsymbol{q}} - \mathbb{1})^{\boldsymbol{q}}\partial^{\alpha}_{\kappa}\,\hat{v}_{\mathrm{KS}}\,|\psi_{\boldsymbol{k}n}\rangle\,. \tag{2.59}$$

In conclusion, (2.54), (2.56) and (2.59) form a set of equations that have to be solved self-consistently, to obtain the electron density response and the variation of the Kohn-Sham potential caused by the lattice displacements. The major advantage of the above formulation is that perturbations of different periodicity are completely decoupled from each other. Hence, phonon perturbations of different $\boldsymbol{q}$ can be treated independently [56].

It turns out that the elements appearing in the matrix of interatomic force constants (IFC's) (2.46) are rather smooth functions of the phonon wave vector $\boldsymbol{q}$ [56]. This means, that the real-space IFC's, obtained by inverse Fourier

transform:

$$C^{\alpha\alpha'}_{\kappa\kappa'}(\boldsymbol{R}) = \frac{1}{N_\mathrm{c}} \sum_l e^{i\boldsymbol{q}_l^T \boldsymbol{R}} C^{\alpha\alpha'}_{\kappa\kappa'}(\boldsymbol{q}_l), \tag{2.60}$$

show a short-range behavior in real space. Thus, for calculations of phonon dispersions and related properties, the method of Fourier interpolation can be used. Here, dynamical matrices are calculated on a comparatively coarse $\boldsymbol{q}$-point grid. These matrices are transformed to real space (2.60) by means of fast Fourier transform. Once the real space IFC's have been obtained, one can calculate dynamical matrices at an arbitrary $\boldsymbol{q}$-point (independent by the choice of the original grid) in reciprocal space.

The extension of DFPT to metallic systems as implemented in Quantum Espresso, was introduced by de Gironcoli in [69]. Equation (2.56) shows the first order change in the self-consistent potential due to lattice displacements. Atomic displacements lead to shifts in the single particle energies, as well as in the Fermi energy. These shifts must be taken into account explicitly for metallic systems. For the variation of the charge density, introduced in (2.40), one obtains for metals [56]:

$$\begin{aligned} {}^{\boldsymbol{q}}\partial^\alpha_\kappa\, n(\boldsymbol{r}) = &\sum_{\boldsymbol{k}n} \Theta^\sigma_{\mathrm{F},n} \left[\psi^*_{\boldsymbol{k}n}(\boldsymbol{r})\, {}^{\boldsymbol{q}}\partial^\alpha_\kappa\, \psi_{\boldsymbol{k}n}(\boldsymbol{r}) + \text{c.c.}\right] \\ &+ \sum_{\boldsymbol{k}n} |\psi_{\boldsymbol{k}n}(\boldsymbol{r})|^2 \delta^\sigma_{\mathrm{F},n} ({}^{\boldsymbol{q}}\partial^\alpha_\kappa\, \varepsilon_\mathrm{F} - {}^{\boldsymbol{q}}\partial^\alpha_\kappa\, \varepsilon_{\boldsymbol{k}n}). \end{aligned} \tag{2.61}$$

where we used a short-hand notation for the smearing function: $\Theta^\sigma_{\mathrm{F},n} = \Theta^\sigma(\varepsilon_\mathrm{F} - \varepsilon_{\boldsymbol{k}n})$, and analogously for $\delta^\sigma_{\mathrm{F},n}$. The second part of (2.61) contains the variation of the Fermi energy and the single particle energies. Treating the variation of the density in the same manner as described above, one ends up with a modified Sternheimer equation for the system. The equations are solved in the same way as in the non metallic case.

For practical aspects of the implementation of DFPT within the plane wave pseudopotential method, as well as for a more detailed discussion for the treatment of metals, we refer the reader to [56] and [69].

2.3 Electron-phonon interaction and superconductivity

In this section we describe the calculation of superconducting properties like the critical temperature and the superconducting energy gap. In a conventional superconductor, the effective pairing between electrons results from the interplay

between the repulsive Coulomb interaction and the exchange of virtual phonons. The calculation of superconducting properties requires a detailed knowledge of the phonon dispersions and the electronic states involved in the superconducting pairing *i.e.* those at the Fermi level. In this work, we estimate the critical temperature for different compounds by calculating the electron phonon coupling matrix elements with DFPT and using the semi-empirical approach of McMillan, Allen and Dynes [70, 71]. There are several other approaches to this issue, such as first-principles Green's function methods [18, 72, 73] or, more recently, methods based on the extension of density functional theory to the superconducting state (SCDFT) [74, 75].

In the next section we give an introduction to the linearized electron-phonon coupling Hamiltonian, followed by an overview of Migdal-Eliashberg theory of superconductivity.

2.3.1 The electron-phonon coupling Hamiltonion

In order to derive the Hamiltonian that describes the electron-phonon interaction, we expand the Kohn-Sham potential in the collective lattice displacements to linear order:

$$\hat{v}_{\mathrm{KS}} = \hat{v}_{\mathrm{KS}}|_{\underline{\boldsymbol{u}}=0} + \sum_{\kappa\alpha l} \left.\frac{\partial \hat{v}_{\mathrm{KS}}}{\partial u^{\alpha}_{\kappa l}}\right|_{\underline{\boldsymbol{u}}=0} u^{\alpha}_{\kappa l} + \mathcal{O}({u^{\alpha}_{\kappa l}}^2). \tag{2.62}$$

Since the Kohn-Sham potential describes the effective potential of a single-particle Schrödinger equation, the total Hamiltonian of the all-electron system can be seen as the sum of Kohn-Sham single-particle operators which commute pairwise. Therefore, the formalism of second quantization can be used, in the same way as for single particle-operators. One obtains:

$$\hat{\mathcal{H}}_{\text{el-ph}} = \sum_{\kappa\alpha l} \hat{u}^{\alpha}_{\kappa l} \sum_{\boldsymbol{k}\boldsymbol{k}',nn'} \langle \psi_{\boldsymbol{k}'n'}| \left.\frac{\partial \hat{v}_{\mathrm{KS}}}{\partial u^{\alpha}_{\kappa l}}\right|_{\underline{\boldsymbol{u}}=0} |\psi_{\boldsymbol{k}n}\rangle \, \hat{c}^{\dagger}_{\boldsymbol{k}'n'} \hat{c}_{\boldsymbol{k}n}. \tag{2.63}$$

Here $\hat{c}^{\dagger}_{\boldsymbol{k}'n'}$ ($\hat{c}_{\boldsymbol{k}n}$) are creation (destruction) operators for electrons in a Bloch state $\boldsymbol{k}n$, satisfying the standard fermionic commutation relations:

$$[\hat{c}_{\boldsymbol{k}n},\hat{c}^{\dagger}_{\boldsymbol{k}'n'}]_{-\epsilon} = \delta_{\boldsymbol{k}\boldsymbol{k}'}\delta_{nn'} \quad \text{and} \quad [\hat{c}_{\boldsymbol{k}n},\hat{c}_{\boldsymbol{k}'n'}]_{-\epsilon} = [\hat{c}^{\dagger}_{\boldsymbol{k}n},\hat{c}^{\dagger}_{\boldsymbol{k}'n'}]_{-\epsilon} = 0 \tag{2.64}$$

in which $[\hat{A},\hat{B}]_{-\epsilon} = \hat{A}\hat{B} - \epsilon\hat{B}\hat{A}$, and $\epsilon = -1$ for fermions. As before, using conservation of momentum and ignoring the Umklapp scattering processes, only the $\boldsymbol{k}+\boldsymbol{q}$ contribution survives from the sum over $\boldsymbol{k}'$. From elementary theory of phonons it is known that the amplitudes can be expressed as a collective

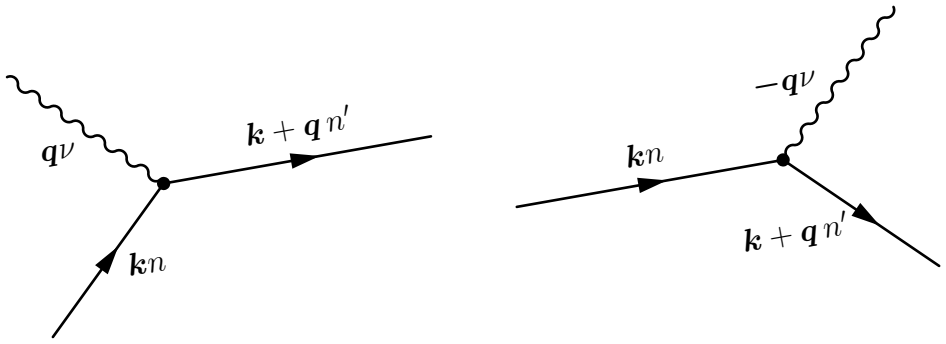

(a) $\hat{c}^\dagger_{\boldsymbol{k}+\boldsymbol{q}\,n'}\hat{c}_{\boldsymbol{k}n}\hat{b}_{\boldsymbol{q}\nu}$ (b) $\hat{c}^\dagger_{\boldsymbol{k}+\boldsymbol{q}\,n'}\hat{c}_{\boldsymbol{k}n}\hat{b}^\dagger_{-\boldsymbol{q}\nu}$

Figure 2.1: Feynman-diagrams describing the terms that appear in the electron-phonon Hamiltonian $\hat{\mathcal{H}}_{\text{el-ph}}$. In the absorpion diagram (a), energy conservation requires that $\varepsilon_{\boldsymbol{k}n} + \omega_{\boldsymbol{q}\nu} = \varepsilon_{\boldsymbol{k}+\boldsymbol{q}\,n'}$; (b) describes the emission of a phonon of wave vector $\boldsymbol{q}$ and energy conservation reads: $\varepsilon_{\boldsymbol{k}n} = \omega_{\boldsymbol{q}\nu} + \varepsilon_{\boldsymbol{k}+\boldsymbol{q}\,n'}$.

creation and destruction of phonons [76]:

$$\hat{u}^\alpha_{\kappa l} = \sum_{\boldsymbol{q}\nu} \frac{1}{\sqrt{N_\text{c} M_\kappa 2\omega_{\boldsymbol{q}\nu}}} c^\alpha_\kappa(\boldsymbol{q}\nu) \left(\hat{b}_{\boldsymbol{q}\nu} + \hat{b}^\dagger_{-\boldsymbol{q}\nu}\right) e^{i\boldsymbol{q}^T\boldsymbol{R}_l} \tag{2.65}$$

where $\hat{b}_{\boldsymbol{q}\nu}$ destroys a phonon of wave vector $\boldsymbol{q}$ in the branch ν. The operators $\hat{b}_{\boldsymbol{q}\nu}$ are describing bosons, hence they are satisfying the commutation relations (2.64) with $\epsilon = +1$. Inserting (2.65) in (2.63) we arrive at the linear electron-phonon coupling Hamiltonian:

$$\hat{\mathcal{H}}_{\text{el-ph}} = \frac{1}{\sqrt{N_\text{c}}} \sum_{\boldsymbol{k},nn'} \sum_{\boldsymbol{q}\nu} g^\nu_{\boldsymbol{k}+\boldsymbol{q}\,n',\boldsymbol{k}n} \hat{c}^\dagger_{\boldsymbol{k}+\boldsymbol{q}\,n'} \hat{c}_{\boldsymbol{k}n} \left(\hat{b}_{\boldsymbol{q}\nu} + \hat{b}^\dagger_{-\boldsymbol{q}\nu}\right), \tag{2.66}$$

where $g^\nu_{\boldsymbol{k}+\boldsymbol{q}\,n',\boldsymbol{k}n}$ are the *screened* electron phonon coupling matrix elements. They describe the scattering of an electron from an initial Kohn-Sham state $|\psi_{\boldsymbol{k}n}\rangle$ to a final state $|\psi_{\boldsymbol{k}+\boldsymbol{q}\,n'}\rangle$ by a phonon of wave vector $\boldsymbol{q}$ and frequency $\omega_{\boldsymbol{q}\nu}$:

$$g^\nu_{\boldsymbol{k}+\boldsymbol{q}\,n',\boldsymbol{k}n} = \sum_{\kappa,\alpha} \frac{1}{\sqrt{M_\kappa 2\omega_{\boldsymbol{q}\nu}}} c^\alpha_\kappa(\boldsymbol{q}\nu) \left\langle \psi_{\boldsymbol{k}+\boldsymbol{q}\,n'} \right| {}^{\boldsymbol{q}}\partial^\alpha_\kappa \, \hat{v}_\text{KS}|_{\underline{\boldsymbol{u}}=0} \left| \psi_{\boldsymbol{k}n} \right\rangle . \tag{2.67}$$

The matrix elements appearing in equation (2.67) are accessible by density functional perturbation theory. Fig. 2.1 shows the Feynman-diagrams describing the electron-phonon interaction.

2.3.2 Migdal-Eliashberg theory

The first complete microscopic theory of electron phonon mediated superconductivity was developed by Bardeen, Cooper and Schrieffer (BCS) in 1957 [15]. In BCS theory, electrons are understood as quasiparticles within the Landau Fermi liquid theory. It is assumed that the effective interaction energy between two quasiparticles of Bloch vectors $\boldsymbol{k}$ and $\boldsymbol{k}'$ is a negative constant, if $\boldsymbol{k}$ and $\boldsymbol{k}'$ are located within a region of width $2\omega_D$ around the Fermi surface, and zero otherwise [17]. Migdal Elishberg theory [77] goes well beyond this approximation including the details of the electron-phonon interaction. The theory provides an accurate treatment of the effects of time retardation of phonon exchange between quasiparticles, as well as of the finite lifetime of quasiparticle states [21]. The theory is accurate to $\mathcal{O}(M^{-\frac{1}{2}})$, where M is the ion mass in electron mass units [78].

In order to construct the theory of strong-coupling superconductivity, the language of thermodynamic Green's functions is adopted. It is convenient to formulate the theory using Nambu-Gor'kov formalism [79] which treats the "normal" and the "pairing" part of the self energy on equal footing [80]. One introduces a two-component field spinor [72]:

$$\hat{\boldsymbol{\Psi}}_{\boldsymbol{k}n} = \begin{pmatrix} \hat{c}_{\boldsymbol{k}n\uparrow} \\ \hat{c}^{\dagger}_{-\boldsymbol{k}n\downarrow} \end{pmatrix}, \tag{2.68}$$

which is used to define a generalized thermodynamic Green's function G [72]:

$$G(\boldsymbol{k}n,\tau) = -\left\langle T_\tau \hat{\boldsymbol{\Psi}}_{\boldsymbol{k}n}(\tau) \hat{\boldsymbol{\Psi}}^{\dagger}_{\boldsymbol{k}n}(0) \right\rangle . \tag{2.69}$$

Here, the expectation value represents the trace over the grand-canonical ensemble, T_τ is the Wick time-ordering symbol in imaginary time τ and the time evolution of the spinors is obtained by

$$\hat{\boldsymbol{\Psi}}_{\boldsymbol{k}n}(\tau) = e^{\hat{\mathcal{H}}\tau} \hat{\boldsymbol{\Psi}}_{\boldsymbol{k}n}(0) e^{-\hat{\mathcal{H}}\tau}, \tag{2.70}$$

in which $\hat{\mathcal{H}}$ represents the total Hamiltonian of the system including electron-electron interactions. Inserting the spinor representation (2.68) into equation (2.69), we see that G takes the form of a generalized 2×2 matrix Green's function:

$$G(\boldsymbol{k}n,\tau) = -\begin{pmatrix} \langle T_\tau \hat{c}_{\boldsymbol{k}n\uparrow}(\tau) \hat{c}^{\dagger}_{\boldsymbol{k}n\uparrow}(0) \rangle & \langle T_\tau \hat{c}_{\boldsymbol{k}n\uparrow}(\tau) \hat{c}_{-\boldsymbol{k}n\downarrow}(0) \rangle \\ \langle T_\tau \hat{c}^{\dagger}_{-\boldsymbol{k}n\downarrow}(\tau) \hat{c}^{\dagger}_{\boldsymbol{k}n\uparrow}(0) \rangle & \langle T_\tau \hat{c}^{\dagger}_{-\boldsymbol{k}n\downarrow}(\tau) \hat{c}_{-\boldsymbol{k}n\downarrow}(0) \rangle \end{pmatrix}. \tag{2.71}$$

Here the diagonal elements are the standard electron quasiparticle propagators, describing single-particle excitations of the system. The off-diagonal elements

can be understood as symmetry-breaking fields which only take finite values in the superconducting state. They are often referred to as the *anamolous* propagators, and describe pairing correlations of the system.

From the trace in equation (2.69), it is straightforward to show that the thermodynamic Green's function has a periodicity of 2β, where $\beta = \frac{1}{k_\mathrm{B}T}$. Here k_B is Boltzmann's constant and T is the absolute temperature. Hence, it is possible to expand the generalized Green's function in a Fourier series:

$$G(\boldsymbol{k}n,\tau) = \frac{1}{\beta}\sum_{j=-\infty}^{\infty} e^{-i\omega_j\tau} G(\boldsymbol{k}n,i\omega_j), \tag{2.72}$$

where $\omega_j = (2j+1)\pi/\beta$ ($j \in \mathbb{Z}$) are the fermion *Matsubara frequencies* which include the temperature T. Due to this expansion, the generalized Green's function depending on Matsubara frequencies can be written as [72]:

$$G(\boldsymbol{k}n,i\omega_j) = \begin{pmatrix} G(\boldsymbol{k}n,i\omega_j) & F(\boldsymbol{k}n,i\omega_j) \\ F^*(\boldsymbol{k}n,i\omega_j) & -G(-\boldsymbol{k}n,-i\omega_j) \end{pmatrix}. \tag{2.73}$$

As before, the $F(\boldsymbol{k}n,i\omega_j)$ take nonzero values only below the critical temperature T_c. As we will see below, those off-diagonal elements are related to the superconducting energy gap.

To get insights into the superconducting state, the next step is to evaluate the matrix Green's function (2.73). This is achieved by using Dyson's equation:

$$G^{-1}(\boldsymbol{k}n,i\omega_j) = G_0^{-1}(\boldsymbol{k}n,i\omega_j) - \Sigma(\boldsymbol{k}n,i\omega_j), \tag{2.74}$$

where $G_0(\boldsymbol{k}n,i\omega_j)$ is the noninteracting propagator, which acquires the well known form:

$$G_0^{-1}(\boldsymbol{k}n,i\omega_j) = i\omega_j\sigma_0 - \varepsilon_{\boldsymbol{k}n}\sigma_3 \tag{2.75}$$

where σ_0 and σ_3 denote Pauli matrices[1]. The chemical potential is set to zero in this equations.

Within Migdal-Eliashberg theory, a number of approximations are introduced in writing the self-energy. In general, the self-energy can be split up into a contribution from the electron phonon interaction and a Coulomb contribution [72]:

$$\Sigma(\boldsymbol{k}n,i\omega_j) = \Sigma_\mathrm{ep}(\boldsymbol{k}n,i\omega_j) + \Sigma_\mathrm{C}(\boldsymbol{k}n,i\omega_j). \tag{2.76}$$

[1]We use the following definition for the Pauli matrices:

$$\sigma_0 = \begin{pmatrix} 1 & 0 \\ 0 & 1 \end{pmatrix},\ \sigma_1 = \begin{pmatrix} 0 & 1 \\ 1 & 0 \end{pmatrix},\ \sigma_2 = \begin{pmatrix} 0 & -i \\ i & 0 \end{pmatrix},\ \sigma_3 = \begin{pmatrix} 1 & 0 \\ 0 & -1 \end{pmatrix}$$

According to Migdal's theorem, it is sufficient to include the first term in the Feynman diagram expansion of the self energy, because all higher terms are on the order of $\lambda\frac{\omega_\mathrm{D}}{\varepsilon_\mathrm{F}}$, where ω_D is a characteristic phonon frequency [78]. Moreover, the self-energy is considered to be diagonal in the band index [72, 81]. This is a reasonable approximation, because the energy scale of the superconducting pairing is small compared to the band separation. Therefore, mixing of different band indices does not have to be taken into consideration. Finally, because Coulomb effects are already included in the diagonal elements of the non-interacting propagator, only off-diagonal elements in the Coulomb contribution to the self-energy are taken into account. Using the approximations discussed in [72, 80, 82, 83, 84], the following expressions for the self-energy contributions are obtained:

$$\Sigma_\mathrm{ep}(\boldsymbol{k}n,i\omega_j) \approx$$

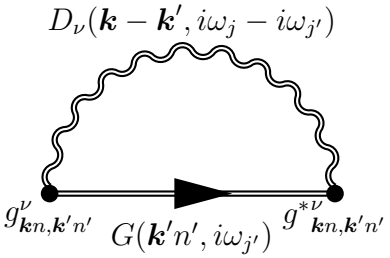

$$= -\frac{1}{\beta}\sum_{\boldsymbol{k}'n',j',\nu} \sigma_3 G(\boldsymbol{k}'n',i\omega_{j'})\sigma_3 |g^{\nu}_{\boldsymbol{k}n,\boldsymbol{k}'n'}|^2 D_\nu(\boldsymbol{k}-\boldsymbol{k}',i\omega_j-i\omega_{j'}), \tag{2.77}$$

and

$$\Sigma_\mathrm{C}(\boldsymbol{k}n,i\omega_j) \approx$$

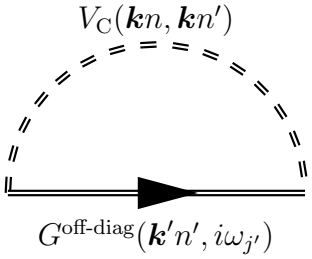

$$= -\frac{1}{\beta}\sum_{\boldsymbol{k}'n',j'} \sigma_3 G^{\text{off-diag}}(\boldsymbol{k}'n',i\omega_{j'})\sigma_3 V_\mathrm{C}(\boldsymbol{k}n,\boldsymbol{k}'n'). \tag{2.78}$$

Equations (2.77) and (2.78) are obtained from standard Feynman rules [85]. In these equations $g^{\nu}_{\boldsymbol{k}n,\boldsymbol{k}'n'}$ are the electron-phonon coupling matrix elements introduced in (2.67). The double wiggly line in 2.77 indicates the dresses phonon propagator: $D_\nu(\boldsymbol{q},i\omega_j) = 2\omega_{\boldsymbol{q}\nu}/[(i\omega_j)^2 - \omega^2_{\boldsymbol{q}\nu}]$. The double-dashed line indicates the screened Coulomb potential $V_\mathrm{C}(\boldsymbol{k}n,\boldsymbol{k}'n')$ between Bloch states $|\psi_{\boldsymbol{k}n}\rangle$ and $|\psi_{\boldsymbol{k}'n'}\rangle$ [72].

In the next step one makes use of the fact that the Pauli matrices form a complete basis set for the space of 2×2 matrices. Hence one can expand the

self-energy in terms of the Pauli matrices using a set of scalar functions as coefficients [83]:

$$\begin{aligned}\Sigma(\boldsymbol{k}n,i\omega_j) = i\omega_j[1 - Z(\boldsymbol{k}n,i\omega_j)]\sigma_0 + \phi(\boldsymbol{k}n,i\omega_j)\sigma_1 + \bar{\phi}(\boldsymbol{k}n,i\omega_j)\sigma_2 \\ + \chi(\boldsymbol{k}n,i\omega_j)\sigma_3.\end{aligned} \tag{2.79}$$

In this expansion, $Z(\boldsymbol{k}n,i\omega_j)$ turns out to be the quasiparticle mass renormalization, $\chi(\boldsymbol{k}n,i\omega_j)$ causes a shift in the single particle energies $\varepsilon_{\boldsymbol{k}n}$, and $\phi(\boldsymbol{k}n,i\omega_j)$ can be seen as the order parameter for the superconducting state. For $\phi = \bar{\phi} = 0$, the system is in the normal state. The gauge can be chosen in such a way that $\bar{\phi} = 0$ [83, 72]. Inserting (2.79) into the Dyson equation and inverting the resulting matrix, one obtains the following expression for the matrix Green's function [72]:

$$\begin{aligned}G(\boldsymbol{k}n,i\omega_j) = -\frac{1}{\Theta(\boldsymbol{k}n,i\omega_j)}\{i\omega_j Z(\boldsymbol{k}n,i\omega_j)\sigma_0 + [\varepsilon_{\boldsymbol{k}n} + \chi(\boldsymbol{k}n,i\omega_j)]\sigma_3 \\ + \phi(\boldsymbol{k}n,i\omega_j)\sigma_1\}\end{aligned} \tag{2.80}$$

in which $\Theta(\boldsymbol{k}n,i\omega_j)$ is the determinant of the inverse Green's function matrix which reads as [72]

$$\Theta(\boldsymbol{k}n,i\omega_j) = [\omega_j Z(\boldsymbol{k}n,i\omega_j)]^2 + [\varepsilon_{\boldsymbol{k}n} + \chi(\boldsymbol{k}n,i\omega_j)]^2 + \phi^2(\boldsymbol{k}n,i\omega_j). \tag{2.81}$$

Finally, one can replace the matrix Green's function in the self-energy equations (2.77) and (2.78) with the expansion (2.80). Equating the coefficients on the two sides results in a set of self consistent equations for the scalar functions introduced. These equations are called *anisotropic Eliashberg equations* [72, 80, 83]:

$$Z(\boldsymbol{k}n,i\omega_j) = 1 + \frac{1}{\beta\omega_j N(\varepsilon_{\mathrm{F}})}\sum_{\boldsymbol{k}'n',j'}\frac{\omega_{j'}Z(\boldsymbol{k}'n',i\omega_{j'})}{\Theta(\boldsymbol{k}'n',i\omega_{j'})}\lambda(\boldsymbol{k}n,\boldsymbol{k}'n',j-j') \tag{2.82}$$

$$\chi(\boldsymbol{k}n,i\omega_j) = -\frac{1}{\beta N(\varepsilon_{\mathrm{F}})}\sum_{\boldsymbol{k}'n',j'}\frac{\varepsilon_{\boldsymbol{k}'n'} + \chi(\boldsymbol{k}'n',i\omega_{j'})}{\Theta(\boldsymbol{k}'n',i\omega_{j'})}\lambda(\boldsymbol{k}n,\boldsymbol{k}'n',j-j') \tag{2.83}$$

$$\begin{aligned}\phi(\boldsymbol{k}n,i\omega_j) = \frac{1}{\beta N(\varepsilon_{\mathrm{F}})}\sum_{\boldsymbol{k}'n',j'}\frac{\phi(\boldsymbol{k}'n',i\omega_{j'})}{\Theta(\boldsymbol{k}'n',i\omega_{j'})} \\ \times[\lambda(\boldsymbol{k}n,\boldsymbol{k}'n',j-j') - N(\varepsilon_{\mathrm{F}})V_{\mathrm{C}}(\boldsymbol{k}n,\boldsymbol{k}'n')].\end{aligned} \tag{2.84}$$

Here $N(\varepsilon_{\mathrm{F}})$ represents the density of states at the Fermi level. Moreover, in equations (2.82)-(2.84) the anisotropic electron-phonon coupling constant $\lambda(\boldsymbol{k}n,\boldsymbol{k}'n',j-j')$ was introduced [72, 80]:

$$\lambda(\boldsymbol{k}n,\boldsymbol{k}'n',j-j') = \int_0^\infty d\omega\frac{2\omega}{(\omega_j-\omega_{j'})^2+\omega^2}\alpha^2F(\boldsymbol{k}n,\boldsymbol{k}'n',\omega) \tag{2.85}$$

in which $\alpha^2F(\boldsymbol{k}n,\boldsymbol{k}'n',\omega)$ is the anisotropic Eliashberg electron-phonon spectral function [72]:

$$\alpha^2F(\boldsymbol{k}n,\boldsymbol{k}'n',\omega) = N(\varepsilon_\mathrm{F})\sum_\nu |g^\nu_{\boldsymbol{k}n,\boldsymbol{k}'n'}|^2\delta(\omega-\omega_{\boldsymbol{k}-\boldsymbol{k}'\nu}). \tag{2.86}$$

The poles of the Green's function (2.80) determine the possible excitation energies of the system. Calculating the poles by setting the denominator to zero provides an expression for the superconducting gap in terms of the order parameter and the quasiparticle renormalization [83]:

$$\Delta(\boldsymbol{k}n,i\omega_j) = \frac{\phi(\boldsymbol{k}n,i\omega_j)}{Z(\boldsymbol{k}n,i\omega_j)}. \tag{2.87}$$

In order to calculate the critical temperature T_c one has to find the temperature where the superconducting gap approaches zero, *i.e.* the highest temperature for which a nontrivial solution is obtained [72].

In practice, it turns out that it is sufficient to confine the important properties of the system to the Fermi surface [80]. This is a reasonable approximation because the energy of the states involved in the superconducting pairing are located in a small energy window around the Fermi surface [72]. Under this approximation the shift in the single-particle energies $\chi(\boldsymbol{k}n,i\omega_j)$ becomes zero, and only two equations are left in the Eliashberg system. Averaging the scalar functions over the Fermi surface results in the *isotropic Eliashberg equations* [72, 21]:

$$Z(i\omega_j) = 1+\frac{\pi}{\beta\omega_j}\sum_{j'}\frac{\omega_{j'}}{\sqrt{\omega_j^2+\Delta^2(i\omega_j)}}\lambda(j-j'), \tag{2.88}$$

$$Z(i\omega_j)\Delta(i\omega_j) = \frac{\pi}{\beta}\sum_{j'}\frac{\Delta(i\omega_{j'})}{\sqrt{\omega_j^2+\Delta^2(i\omega_j)}}[\lambda(j-j')-\mu^\star_\mathrm{C}]. \tag{2.89}$$

In equation (2.89), the term $N(\varepsilon_\mathrm{F})V_\mathrm{C}(\boldsymbol{k}n,\boldsymbol{k}'n')$ has been replaced by the renormalized Coulomb pseudopotential $\mu^\star_\mathrm{C}$. This parameter describes the effective Coulomb interaction between the electrons which is significantly weakened due to retardation effects. Under some approximations [86] $\mu^\star_\mathrm{C}$ is given by

$$\mu^\star_\mathrm{C} = \frac{\mu_\mathrm{C}}{1+\mu_\mathrm{C}\ln(\varepsilon_\mathrm{F}/\omega_\mathrm{cut})}, \tag{2.90}$$

where $\mu_\mathrm{C} = N(\varepsilon_\mathrm{F})\,\langle\langle V_\mathrm{C}(\boldsymbol{k}n,\boldsymbol{k}'n')\rangle\rangle$ is the double Fermi-surface average of the Coulomb transition matrix-elements and ω_cut is a cutoff phonon frequency on the order of 1 eV [72]. In practice the renormalized Coulomb pseudopotential

is taken as a free parameter and is used to fit the superconducting properties to the experimental results.

The auxiliary function $\lambda(j-j')$ is defined analogously to (2.85), with the difference that the Fermi surface averaged Eliashberg function $\alpha^2F(\omega)$ enters the equation. This quantity plays a fundamental role in calculating superconducting properties. If we use the electron-phonon coupling matrix elements derived in equation (2.67), the Fermi surface average of equation (2.86) takes the form

$$\begin{aligned}\alpha^2F(\omega) = \frac{1}{N(\varepsilon_\mathrm{F})}\sum_{\boldsymbol{kq}}\sum_{nn'\nu}|g^\nu_{\boldsymbol{k}n,\boldsymbol{k}+\boldsymbol{q}\,n'}|^2\delta(\omega-\omega_{\boldsymbol{q}\nu}) \\ \times\,\delta(\varepsilon_{\boldsymbol{k}n}-\varepsilon_\mathrm{F})\delta(\varepsilon_{\boldsymbol{k}+\boldsymbol{q}\,n'}-\varepsilon_\mathrm{F}).\end{aligned} \tag{2.91}$$

This function describes the coupling of phonon modes of frequency ω to electronic states at the Fermi level. As pointed out in the following section, it contains the essential information for obtaining the superconducting transition temperature T_c. It is noteworthy that the Eliashberg function (2.91) is related to the phonon linewidths $\gamma_{\boldsymbol{q}\nu}$ which can be derived from Fermi's golden rule [87]:

$$\gamma_{\boldsymbol{q}\nu} = 2\pi\omega_{\boldsymbol{q}\nu}\sum_{\boldsymbol{k}}\sum_{nn'}|g^\nu_{\boldsymbol{k}n,\boldsymbol{k}+\boldsymbol{q}\,n'}|^2\delta(\varepsilon_{\boldsymbol{k}n}-\varepsilon_\mathrm{F})\delta(\varepsilon_{\boldsymbol{k}+\boldsymbol{q}\,n'}-\varepsilon_\mathrm{F}). \tag{2.92}$$

From equation (2.92), it can be seen that the matrix elements $g^\nu_{\boldsymbol{k}n,\boldsymbol{k}+\boldsymbol{q}\,n'}$ are multiplied by a double-delta summation which is referred to as the Fermi surface nesting function. The linewidths take high values if there are parallel regions in the Fermi surface related by a wave vector $\boldsymbol{q}$, together with high electron phonon coupling matrix elements. Using the defined linewidths, the Eliashberg function takes the form:

$$\alpha^2F(\omega) = \frac{1}{2\pi N(\varepsilon_\mathrm{F})}\sum_{\boldsymbol{q}}\sum_{\nu}\frac{\gamma_{\boldsymbol{q}\nu}}{\omega_{\boldsymbol{q}\nu}}\delta(\omega-\omega_{\boldsymbol{q}\nu}) \tag{2.93}$$

2.3.3 Estimation of the critical temperature

In order to calculate the Fermi-surface-averaged Eliashberg function (2.91), one needs a detailed knowledge of the phonon dispersion, the electronic states at the Fermi level, and the electron-phonon coupling matrix elements. The latter are in principle accessible by density functional based methods. As it can be seen from equation (2.67), we need the linear response of the Kohn-Sham potential due to phonon perturbation of wave vector $\boldsymbol{q}$ according to equation (2.56). As pointed out in section 2.2.2, the linear response of the Kohn-Sham potential is an ingredient of density functional perturbation calculations. The

electron-phonon coupling matrix elements, as well as the double integral over the fermi surface (2.91) are calculated in a second step in which a dense $\boldsymbol{k}$-grid is used to sample the Kohn-Sham states.

A detailed review how those matrix elements are calculated in practice has been given by Savrasov *et.al.* in [88, 89]. In this review, calculations are performed within a linear–muffin-tin–orbital basis set. It is shown how the matrix elements (2.67) are obtained directly from the linear response of the Kohn-Sham states, including corrections for the incompleteness of the basis.

In practice, the double delta integral in equation (2.91) is evaluated using several values of Gaussian broadening for the δ-functions. This procedure quickly shows wether the results are converged with respect to $\boldsymbol{k}$-point sampling and the smearing-parameter.

As discussed in the previous section, in order to obtain the critical temperature T_c, in principle the Eliashberg equations (2.82)-(2.84) have to be solved. In this work we use a simplified semi-empirical approach for estimating T_c using the Allen-Dynes [70] modified McMillan [71] formula. The Allen-Dynes modification is based on more than 200 numerical solutions of the Eliashberg equations [21], covering a large range of electron-phonon coupling constants. The resulting expression is:

$$T_\mathrm{c} = \frac{\omega_\mathrm{log}}{1.2 k_\mathrm{B}} \exp\left[-\frac{1.04(1+\lambda)}{\lambda - \mu^\star_\mathrm{C}(1+0.62\lambda)}\right] \tag{2.94}$$

where λ is the electron-phonon coupling constant defined by

$$\lambda = \int_0^\infty d\omega \frac{\alpha^2 F(\omega)}{\omega}, \tag{2.95}$$

and ω_log is the logarithmic average phonon frequency:

$$\omega_\mathrm{log} = \exp\left[\frac{2}{\lambda}\int_0^\infty \frac{\alpha^2 F(\omega)\ln(\omega)}{\omega}\right]. \tag{2.96}$$

As already mentioned, the renormalized Coulomb pseudopotential $\mu^\star_\mathrm{C}$ is used as a parameter taking values between 0.1 and 0.15. Although Eq. (2.94) is based on quantities averaged over the Fermi surface, it provides results in good agreement with experiments [90], even for systems with anisotropic Fermi surfaces [91, 92].

2.4 The electron localization function (ELF)

An extremely useful tool for characterizing chemical bonding in crystals as well as in molecular systems is provided by the electron localization function (ELF)

introduced by Becke and Edgecombe in 1990 [93]. This quantity is based on the conditional same-spin pair probability function and provides a measure of real space electron pair localization.

The starting point of the derivation is an extension of equation (2.6) to the case of two electrons. The expression can be considered as the diagonal element of the second order reduced density matrix:

$$\gamma^{(2)}_{\sigma_1\sigma_2}(\boldsymbol{r}_1,\boldsymbol{r}_2) = N(N-1)\sum_{\sigma_3\ldots\sigma_N}\int d^3r_3\cdots d^3r_N \times |\Psi(\boldsymbol{r}_1\sigma_1,\boldsymbol{r}_2\sigma_2,\ldots,\boldsymbol{r}_N\sigma_N)|^2. \tag{2.97}$$

This gives the probability density of finding an electron at position $\boldsymbol{r}_1$ with spin σ_1 and, simultaneously an electron at position $\boldsymbol{r}_2$ with spin σ_2. If we ignore the fermionic character of the electrons, the latter would just be the product of the spin dependent densities $n_{\sigma_1}(\boldsymbol{r}_1)n_{\sigma_2}(\boldsymbol{r}_2)$. However, because of the Pauli exclusion principle, there is a correlation hole associated to the electrons and thus the probability of finding an electron with the same spin in the vicinity of another electron will be low. The same-spin conditional pair probability function, *i.e.* the probability of finding a spin σ electron at $\boldsymbol{r}_2$, knowing with certainty that a second electron with spin σ is located at $\boldsymbol{r}_1$ is given by [94]:

$$P_\sigma(\boldsymbol{r}_2|\boldsymbol{r}_1) = \frac{\gamma^{(2)}_{\sigma\sigma}(\boldsymbol{r}_1,\boldsymbol{r}_2)}{n_\sigma(\boldsymbol{r}_1)}. \tag{2.98}$$

To obtain the probability density of finding a second electron with the same spin within a sphere of radius s around the reference electron at $\boldsymbol{r}_1$, one can integrate out the angular dependence in $\boldsymbol{r}_2$:

$$p_\sigma(\boldsymbol{r}_1,s) = \frac{1}{4\pi}\int_0^{2\pi} d\varphi \int_0^{\pi} d\vartheta \sin\vartheta\, P_\sigma(\boldsymbol{r}_1 + s\boldsymbol{e}_r|\boldsymbol{r}_1), \tag{2.99}$$

where $\boldsymbol{e}_r = (\sin\vartheta\cos\varphi, \sin\vartheta\sin\varphi, \cos\vartheta)^T$. For small s one can Taylor-expand $P_\sigma(\boldsymbol{r}_1+s\boldsymbol{e}_r|\boldsymbol{r}_1)$ in s. The zero order term vanishes because of the Pauli exclusion principle. Also the first-order term drops out when performing the expansion. We skip the Taylor expansion of (2.99) which can be found in [94] and just state the final result. One obtains

$$p_\sigma(\boldsymbol{r}_1,s) = \frac{1}{3}s^2 C_\sigma(\boldsymbol{r}_1) + \mathcal{O}(s^3) \tag{2.100}$$

where $C_\sigma(\boldsymbol{r}_1)$ is given by

$$C_\sigma(\boldsymbol{r}_1) = \frac{1}{2}\frac{\nabla^2_{\boldsymbol{r}_2}\gamma^{(2)}_{\sigma\sigma}(\boldsymbol{r}_1,\boldsymbol{r}_2)|_{\boldsymbol{r}_2=\boldsymbol{r}_1}}{n_\sigma(\boldsymbol{r}_1)}. \tag{2.101}$$

in which $\nabla_{\boldsymbol{r}_2}$ indicates the nabla operator with respect to the $\boldsymbol{r}_2$-coordinate. The function (2.101) is used to define the electron localization function [93]:

$$\mathrm{ELF}_\sigma(\boldsymbol{r}) = \frac{1}{1 + \{C_\sigma(\boldsymbol{r})/C_\sigma^{\mathrm{h}}[n_\sigma(\boldsymbol{r})]\}^2} \tag{2.102}$$

where $C_\sigma^{\mathrm{h}}[n_\sigma(\boldsymbol{r})]$ denotes the expression (2.101) evaluated for the homogenous electron gas [94, 95]. The ELF takes values between 0.5 and 1, where 1 corresponds to perfect localization and 0.5 corresponds to the homogenous electron gas. In practice, one plots an isocontour at some value between 0.5 and 1 which provides information on electron pair localization.

So far, the derivation of the ELF was very general. Within density functional theory one makes the approximation that the wave-function in (2.97) is a single Slater determinant constructed from Kohn-Sham orbitals. In general it turns out that the ELF is quite insensitive of the method used for obtaining the orbitals, as long as the single-particle wavefunctions involved properly reflect the Pauli exclusion principle [96]. Within the DFT framework, in the absence of magnetic fields and spin orbit coupling [94], the following expression is obtained for $C_\sigma(\boldsymbol{r})$ [95, 96]:

$$C_\sigma(\boldsymbol{r}) = \tau_\sigma(\boldsymbol{r}) - \frac{1}{4}\frac{[\nabla n_\sigma(\boldsymbol{r})]^2}{n_\sigma(\boldsymbol{r})}, \tag{2.103}$$

where $\tau_\sigma(\boldsymbol{r})$ is the kinetic energy density:

$$\tau_\sigma(\boldsymbol{r}) = \sum_{\boldsymbol{k}n} |\nabla \psi_{\boldsymbol{k}n\sigma}(\boldsymbol{r})|^2. \tag{2.104}$$

Eq. (2.103) can be viewed as the eccess kinetic energy density due to the Pauli repulsion [96]. The dominant term in (2.103) is the kinetic energy density (2.104), which takes high values in regions between those where orbitals localize, thus (2.103) indicates the boundaries of electron localization [96].

Chapter 3

Evolutionary Crystal Structure Prediction

Crystal structure prediction from first principles has long been remained a problem of intractable complexity. Until the late 1990's it was generally claimed that it is not possible to predict crystal structures of a given stoichiometry, without additional information from experiment. In the last few years, many attempts have been made to address this problem using different optimization schemes such as simulated annealing [97], metadynamics [98, 99], particle swarm optimization [100] as well as the minima hopping method [101]. Some of the most advanced methods upon this field make use of *evolutionary* or *genetic* algorithms [12, 13, 14, 102, 103, 104, 105].

Evolutionary algorithms for crystal structure prediction are inspired from the basic mechanisms of biological evolution such as selection, mutation and reproduction. A classical simulation starts with an initial *population* of structures, produced randomly, if necessary by using information from previous knowledge. The *individuals* are assessed by a fitness function, which is usually chosen to be the specific enthalpy or the free energy. From the best structures, new *child structures* are produced applying various variation operators (see below). In this sense, the new structures *inherit* the properties from the parent structures which are carried onto the next *generation*. The best individuals from this new generation are again chosen to be parent structures of the next one. The great success of this method can be attributed to the fact that it is not necessary to sample the full energy landscape *i.e.* the full configuration space of geometries. The initial population gradually evolves towards a generation which includes structures close to the global minimum of the energy landscape.

Nowadays, evolutionary algorithms are widely used in the field of crystalography and quantum chemistry. Applications range from prediction of novel high

pressure-phases to applications in drug design in the field of computational pharmaceutics [106]. Recent developments allow the prediction of thermodynamically stable compositions without an initial knowledge of the compound stoichiometry. In the following paragraph we point out two applications of the method and their experimental justification.

3.1 Predictive power of evolutionary crystal structure prediction

Sodium is usually considered an almost perfect free-electron metal at ambient conditions. Calculations performed by Y. Ma *et.al.* predicted that sodium will transform into a transparent insulating phase at pressures of approximately 200 GPa. The emergence of this insulating phase can be attributed to *p-d* hybridization of the valence electrons, and their repulsion by the core states. These results where confirmed experimentally by Eremets *et.al.* [107].

In the hydrogen-sulfur system, at ambient conditions, the only stable compound is molecular H_2S. Calculations by Duan *et.al.* [108] using evolutionary algorithms, revealed the thermodynamical stability of a new H_3S compound at increased pressures. At pressures of 200 GPa, first-principle-calculations indicated that this compound shows a superconducting critical temperature of ~ 200 K. The results where later confirmed by experiments of Drozdov *et.al.* In fact, this was the first example of a *conventional* high-T_c superconductor predicted completely from first principles and later confirmed by experiment.

3.2 Computational complexity of crystal structure prediction

Crystal structure prediction can be considered as an optimization problem, *i.e.* the problem of finding the global minimum of the free-energy landscape. It turns out that a crucial issue in evolutionary algorithms for crystal structure prediction is the representation of the individuals. Unlike ordinary genetic algorithms, where the information contained in the unit cells is mapped to a binary string, modern crystal structure prediction techniques are using real number representations for the atom positions and the cell parameters [109]. For a complete representation we need 6 numbers for the unit cell (3 lattice constants and 3 angles), as well as $3(N-1)$ numbers for the atomic coordinates, where N is the number of atoms in the unit cell. Therefore, the dimensionality

of the search space is given by

$$d = 3N + 3. \tag{3.1}$$

The number of points in the search space can be estimated in the following way: The volume of the unit cell is divided into voxels of volume δ^3, where one voxel represents the space an atom occupies in the unit cell. The number of points C in the energy landscape is than given by the number of ways the N atoms can be distributed over these elements. Taking into account the different types of atoms one finds [14, 109]:

$$C = \binom{V_\mathrm{u}/\delta^3}{N} \prod_\xi \binom{N}{n_\xi}, \tag{3.2}$$

where n_ξ is the number of atoms with atomic species ξ. The number C can be astronomically high, even for small systems. Applying Stirling's formula to (3.2) shows that C grows exponentially with the dimensionality of the system [14]:

$$C \propto e^{\beta d}, \tag{3.3}$$

where β is a system-dependent constant. Eq. (3.3) shows that the scaling of the system with dimensionality is faster than any polynomial, hence the crystal structure prediction problem belongs to the complexity class of NP-hard problems [14, 109].

A tremendous improvement of the situation is achieved including local optimization steps in the algorithm. Within one optimization step, the parameters of the system are adjusted around a local energy minimum, using optimization methods like the conjugate gradient or the quasi-Newton algorithm. After performing local relaxations, certain degrees of freedom of the system such as atomic positions, lattice parameters etc. are no longer uncorrelated, which effectively reduces the possible number of configurations. Fig. 3.1 schematically shows how the energy landscape is reduced due to local relaxations of the individuals. The overwhelming amount of possible configurations C is reduced to physically meaningful crystal structures.

Because of correlations between the parameters of the individuals, the dimensionality (3.1) is reduced to the *intrinsic dimensionality* $d^\star$ [109]:

$$d^\star = 3N + 3 - \kappa, \tag{3.4}$$

where κ, in general, is a non-integer number. The decrease in dimensionality can be significant for some systems. Oganov *et.al.* found a reduction from 99 to 11.6 for $Mg_{16}O_{16}$ [110]. The reduction for more chemically complex systems is less substantial.

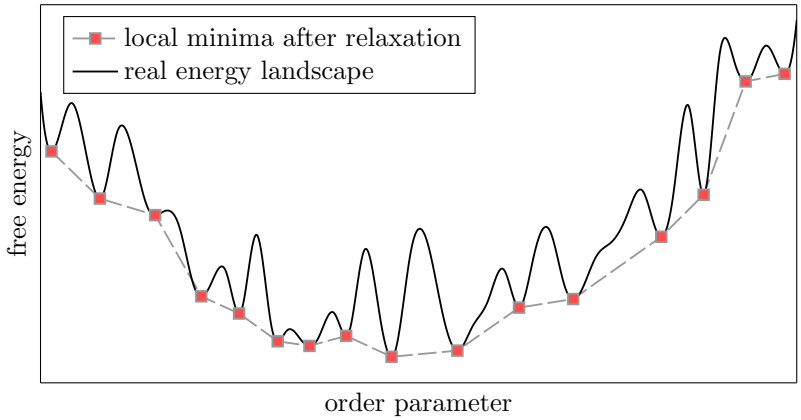

Figure 3.1: Schematic illustration of the energy landscape as a function of one order parameter. The dashed line indicates the reduced landscape due to local relaxation of the individuals. The figure has been taken from [109].

For the evaluation of the fitness function, as well as for the local optimization of the individuals, *ab-inito* methods are used. Since those methods are computationally expensive, efficient evolutionary algorithms should be able to avoid sampling unpromising regions of the energy landscape. This is achieved by an intelligent adaptation of *parent-selection* which generates the new population (*see below*). In conclusion, the minimum thresholds inherent in the intermediate relaxation steps (such as cutoff-energy and $\boldsymbol{k}$-points sampling) turn out to be the main limiting factor for the convergence speed of the algorithm.

3.3 Elements of evolutionary algorithms

As already mentioned, the language for describing the essential elements of evolutionary algorithms is inspired by biological evolution. In the following we summarize the important terms [109]:

- **Individual.** A single point in configuration space (one unit cell).
- **Population (generation).** A set of points in configuration space or of candidate structures for the global minimum. The number of individuals within the set is called population size.
- **Selection.** A process that divides the current population into individuals that are discarded and individuals which form the basis of the next generation.

- **Parents**. A subset of structures from a population that "survived" the selection process. The new generation is created from these structures by means of variation operators.
- **Offspring.** Structures created from parents by means of variation operators.
- **Heredity.** The Heredity operator combines characteristic properties from one ore more parents into an offspring-structure.
- **Mutation.** Mutation operators produce a child structure from a single parent by altering some degrees of freedom.

Fig. 3.2 shows a flowchart of a typical evolutionary algorithm [111]. After initialization of the first population, the structures are relaxed using several *ab-initio* simulation steps with gradually increasing precision. After the first optimization step the selection procedure is applied, resulting in a new population. The individuals in the new population, undergo again the structural relaxation process. The procedure is repeated until convergence with respect to some halting criteria has been achieved.

In the following sections we will describe the elements of the evolutionary algorithm in more detail, going from the top to the bottom of the flowchart in Fig. 3.2.

3.3.1 Initialization and constraints

One of the most important success factors for evolutionary algorithms is the initialization of the initial population. The first set of crystal structures should be characterized by a high diversity, an uniform distribution over the energy landscape and a physically meaningful representations of the individuals.

If there is no previous knowledge from earlier runs or experiment, a common way to initialize the first population is a uniform random generation of crystal structures [12, 109]. In this case, the lattice vectors of the unit cell as well as the positions of the atoms within the cell are chosen randomly. However, such a random initialization produces also unphysical individuals which have to be discarded from the population.

Within the USPEX-code [12], a structure is considered to be unphysical if one of several constraints is violated. First of all, the distance between two atoms should not be less than a user-defined value. Even at extreme pressures, there are no known bonds shorter than 0.5 Å [109]. Second, the length of the lattice vectors should not below a predefined threshold. One can set the shortest lattice vector to the ionic diameter of the largest atom. Furthermore, a structure is

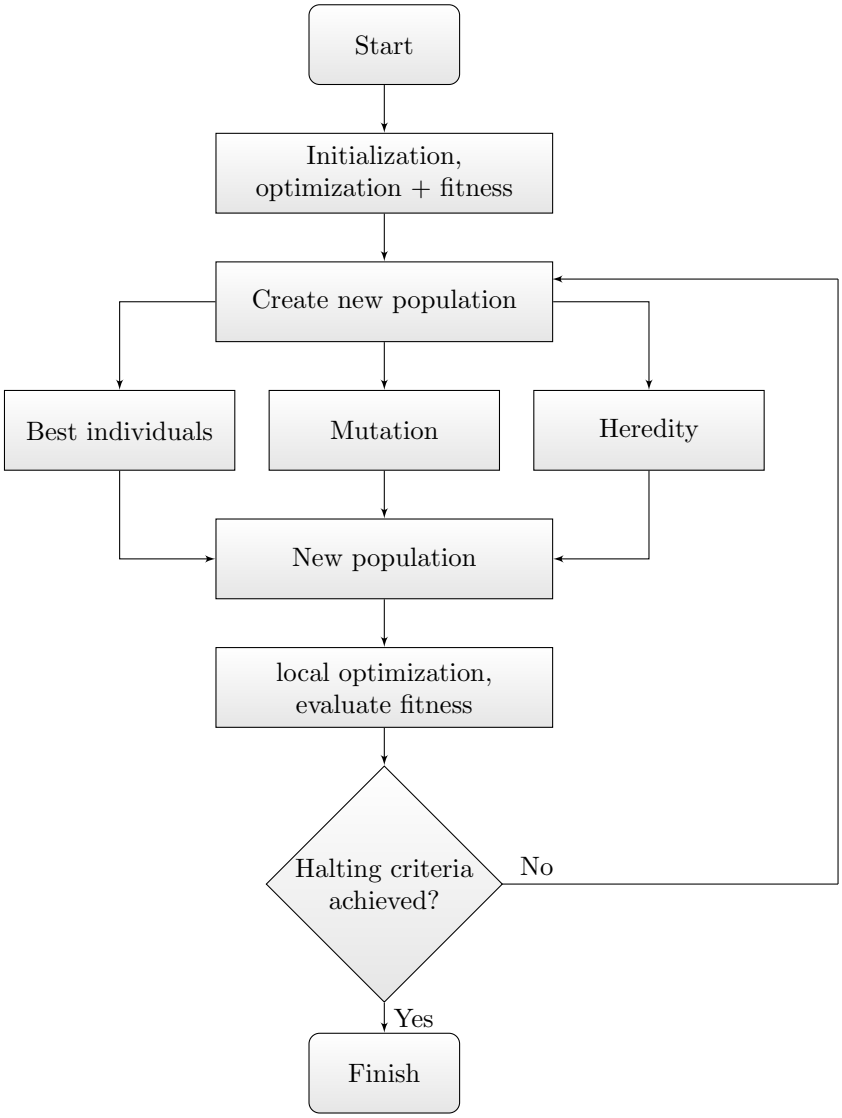

Figure 3.2: Simplified flowchart of typical evolutionary algorithm [111]

considered unphysical, if one of the unit cell angles is too small. Oganov *et.al.* [103] introduced a cell transformation where the lattice vectors are rescaled in such a way, that all angles fall in the (60°,120°)-range.

Random initialization causes a problem for large systems ($N > 20$) [112]. With an increasing number of atoms, randomly-generated structures become more and more similar and disordered. Structures of this type show similar thermodynamic properties and are in general energetically poor [113]. A simple strategy to overcome this problem is *cell splitting* [113]. Here a translational *pseudosymmetry* is introduced splitting the unit cell into subcells that are filled randomly with atoms and vacancies [111].

The method to set up the first population was improved by Lyakhof *et.al.* including the symmetries of the space groups. Within this scheme, the structure is constructed by choosing one of the 230 space groups consistent with the predetermined number of atoms in the unit cell. After rescaling the unit cell to the desired volume, an atom is placed randomly on a general Wyckoff position and the symmetry operations of the space group are applied. If this procedure results in a situation where the distance of two atoms violates the constraint, the atoms are merged into a single atom by averaging the coordinates. This is equivalent to putting a single atom directly into a high-symmetry position and applying the symmetry operations afterwards. During the procedure of adding atoms, one has to ensure not to exceed the desired number of atoms, which involves moving atoms on Wyckoff positions with lower multiplicity. This method has proven to be a significant enhancement for the structure prediction of large systems [111].

3.3.2 Selection and fingerprint functions

One of the crucial steps of evolutionary algorithms turns out to be the selection of appropriate parent structures. The trade-off one has to deal with is that on the one hand, the algorithm should gradually converge to populations comprising structures of higher fitness and on the other hand one has to ensure a high diversity of structures in the population.

A naive way to select parents would just be to take the best structures according to their fitness ranking. However, the best structures of a population are usually located in the same basin of attraction of a local minimum and variation operators will produce individuals close to that basin [113]. Because of this, the population is gradually flooded with structures from the same basin and the algorithm gets trapped in a local minimum. This phenomenon is called *genetic drift* [114], and is a common problem associated with evolutionary and genetic algorithms. One possible solution that maintains a relatively high diversity in the population is the stochastic selection scheme [109]. Here, a relatively large fraction ($\sim 60\%$) of the best individuals is chosen as a possible pool of parent structures. The probability for an individual to be chosen as a parent is proportional to its fitness ranking.

More modern and sophisticated selection schemes are based on *fingerprint functions* [110]. In order to determine the similarity between different individuals reliably, a unique function is needed, which is independent of the crystal structure representation. Moreover, the function should be quite insensitive to numerical errors, and should give a considerable response if two or more atoms are interchanged [109]. The following definition for the fingerprint function was

introduced by Oganov, Valle *et.al.* [109, 110, 112]. The function is related to the radial distribution function and to diffraction spectra [109]:

$$f(R) = \frac{1}{\mathcal{N}} \sum_{\substack{\langle \mu,\nu \rangle \\ \nu \neq \mu}} \frac{Z_\mu Z_\nu}{4\pi R_{\mu\nu}^2} \frac{V_\mathrm{u}}{N} \, \delta_\sigma(R - R_{\mu\nu}) - 1, \tag{3.5}$$

where Z_μ are the atomic numbers for atom μ, $R_{\mu\nu} = |\boldsymbol{R}_\mu - \boldsymbol{R}_\nu|$ is the distance between atoms μ and ν, V_u is the unit cell volume, N is the total number of atoms in the unit cell and $\delta_\sigma(x)$ is a Gaussian function of width σ. The notation $\langle \mu,\nu \rangle$ for the sum index means that the sum over ν is restricted within a cutoff radius around atom μ. The prefactor of the double sum in (3.5) is given by

$$\mathcal{N} = \sum_{\xi,\eta} Z_\xi Z_\eta n_\xi n_\eta, \tag{3.6}$$

where the double sum runs over all distinct atom types and n_ξ denotes the number of atoms with atomic number Z_ξ.

The function (3.5) only depends on interatomic distances and is therefore independent of the representation. In order to compare the fingerprint functions of different structures one introduces a vector $\boldsymbol{v}_\mathrm{FP}$, whose entries correspond to the panel elements of the discretised fingerprint. The i'th vector element is obtained by

$$\{\boldsymbol{v}_\mathrm{FP}\}_i = \frac{1}{D} \int_{iD}^{(i+1)D} f(R) dR, \tag{3.7}$$

where D describes the width of a discretization interval. Eq. (3.7) can be used to define a metric in fingerprint space. Two structures have the same fingerprint if the scalar product of the normalized vectors $\boldsymbol{v}_\mathrm{FP}/\|\boldsymbol{v}_\mathrm{FP}\|$ is equal to one. Therefore, a natural choice for the distance measure between two structures denoted by π_i and π_j, is the cosine metric [109, 113, 112]:

$$d(\pi_i,\pi_j) = 0.5 \left(1 - \frac{\boldsymbol{v}_\mathrm{FP}^T(\pi_i) \boldsymbol{v}_\mathrm{FP}(\pi_j)}{\|\boldsymbol{v}_\mathrm{FP}(\pi_i)\| \|\boldsymbol{v}_\mathrm{FP}(\pi_j)\|} \right). \tag{3.8}$$

Eq. (3.8) takes values between 0 and 1 and provides a "similarity" criteria for the individuals. This distance metric can also be used to define a measure of disorder and diversity for the structures within a population. This is the so called *quasi-entropy* S [109, 110, 112, 113]:

$$S = -\frac{1}{N_\mathrm{pop}^2 - N_\mathrm{pop}} \sum_{i,j \neq i} [1 - d(\pi_i,\pi_j)] \ln[1 - d(\pi_i,\pi_j)], \tag{3.9}$$

where i and j run over all structures within a population and N_{pop} is the number of individuals in the population. High values of the quasi-entropy correspond to a uniform distribution of fingerprint metrics and hence to high diversity in the population. The quasi-entropy can be used as an indicator for premature convergence.

Using the introduced fingerprint metric (3.8), the selection process can be improved significantly. To avoid genetic drift, one just takes different structures and ignores all similar ones [109]. This is achieved by means of the *clustering technique* [111]. Here, the population is divided into a predefined number of groups. Starting from an arbitrary structure π_i, all structures that are located within some threshold distance around π_i are put into a group. The process is repeated for all remaining individuals until all of them belong to some group. If the resulting number of groups differs from the desired one, the threshold distance is modified and the population is reclustered. In the end, the best structure from each group survives into the next generation.

In general it turns out that it is a good idea to keep the best structures from a population unchanged into the next one. Different investigations indicate that this enhances the learning character of the algorithm [109]. However one has to be careful not to take to many structures from the same energy funnel.

3.3.3 Variation operators

Variation operators are used to construct the new population from the selected parent structures, and hence play a crucial role in all evolutionary algorithms. There are basically three different types of variation operators: *Mutation, heredity* and *permutation*.

Mutation operators generate a child structure from a single parent by distorting the atom positions or the lattice vectors. In lattice mutation, the new lattice vectors are obtained applying a symmetric strain matrix [109]:

$$\boldsymbol{a}' = \begin{pmatrix} 1+\epsilon_{11} & \frac{\epsilon_{12}}{2} & \frac{\epsilon_{13}}{2} \\ \frac{\epsilon_{21}}{2} & 1+\epsilon_{22} & \frac{\epsilon_{23}}{2} \\ \frac{\epsilon_{31}}{2} & \frac{\epsilon_{32}}{2} & 1+\epsilon_{33} \end{pmatrix} \boldsymbol{a}. \tag{3.10}$$

Here, the ϵ_{ij} are random numbers from a Gaussian distribution with mean value zero and a user-predefined deviation. Because lattice mutation does not conserve volume, after applying (3.10), the volume is rescaled to V_u. Lattice mutation is used to explore the vicinity of energetically good structures and helps to prevent premature convergence [109].

In recent years, mutation of atomic coordinates has become part of the evolutionary structure prediction technique [112, 113]. Using a projection of the

fingerprint function for single atoms [113], it is possible to calculate the contribution of individual atoms to the total degree of order. In the mutation process, random numbers with a Gaussian distribution are added to the atomic coordinates. For atoms in high-symmetry positions, the width of the Gaussian is smaller, *i.e.* they are influenced less than atoms associated with a low degree of local order. It has been demonstrated that such an "intelligent" distortion of atomic positions can increase the efficiency of the algorithm [113].

Soft mutation represents a powerful variant of the mutation operator and is used as a standard operation in the USPEX code [111]. The underlying principle of this operator was first investigated by Roy *et.al.* in [115]. They discovered that, if a system is located in a local energy minimum, lower-lying minima are usually separated by small energy barriers. Hence, the basic idea of soft mutation is to move the atoms along the direction of the eigenvector of the softest phonon mode, because low-frequency eigenmodes correspond to directions with low curvature in the Born-Oppenheimer energy surface. The amplitude of the ionic displacements is an user-defined parameter, but should be chosen to be of the order of the average bond length [111].

Fortunately, it is not necessary to move the atoms exactly in the direction of to the eigenvector associated with the softest mode [111]. Otherwise, the huge computational effort for calculating the dynamical matrix would by far exceed the gain of the soft-mutation operator. The dynamical matrix can be estimated from the bond-hardness coefficients, which can be calculated from bond lengths and tabulated atomic properties like ionic radii and electronegativity [111]. It turns out that this very crude approximation yields surprisingly good results for the soft mutation operator.

Heredity operators are used to merge the characteristic properties of two or more individuals into one child structure. Within the USPEX-code, the heredity operator combines spatially coherent slabs of two parent structures. In more detail the method works as follows. In the beginning, the atomic positions of the atoms are shifted by a vector $\boldsymbol{w}^{(\mathrm{p})} = x_1^{(\mathrm{p})}\boldsymbol{a}_1^{(\mathrm{p})} + x_2^{(\mathrm{p})}\boldsymbol{a}_2^{(\mathrm{p})} + x_3^{(\mathrm{p})}\boldsymbol{a}_3^{(\mathrm{p})}$, where $\boldsymbol{a}_i^{(\mathrm{p})}$ are the lattice vectors of the parents (p), and $x_i^{(\mathrm{p})}$ are uniformly distributed random numbers from the interval [0,1]. If an atom falls outside the unit cell, it is mapped back to the unit cell, subtracting the corresponding lattice vectors. After this, two planes are constructed, defined by the point $x\boldsymbol{a}_i^{(\mathrm{p})}$, where x is a random number from [0,1] and $\boldsymbol{a}_i^{(\mathrm{p})}$ are randomly chosen lattice vectors, and the two remaining lattice vectors of the corresponding parents. The offspring is formed by the atoms below the plane of the first parent structure, and the atoms above the plane of the second parent structure [13]. In the process of putting the slabs together, the child structure can end up with too few or too many atoms in the unit cell. In this case, atoms are added or removed depending on their local degree of order [113]. As in the case of atomic mutation, atoms

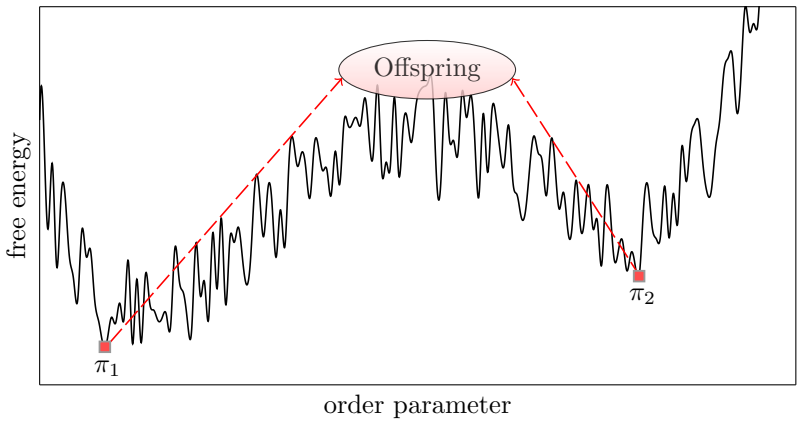

Figure 3.3: Schematic representation of a projection of the energy landscape with two well seperated energy funnels. Combining structures π_1 and π_2 results in an energetically bad offspring. [111]

located in high-symmetry positions are more likely kept. It has also been shown that the performance can be enhanced slicing the parent structures into several slabs of random thickness and using the slabs with the highest average order to construct the child.

The heredity operator can further be improved using the fingerprint metric (3.8). Usually, if structures from different energy funnels are combined, it is very likely that the offspring will be located at a barrier between the two funnels (see Fig. 3.3). This can be avoided by combining only structures by a distance below a given threshold $d_{\mathrm{cut}}(\pi_i,\pi_j)$ [109].

Permutaion operators interchange the chemical identities of two randomly selected atoms, hence this operator has an effect only on systems with at least two different types of atoms. It has been demonstrated that this operator is very useful for systems where chemically similar atoms are present [109].

In practical calculations, the fraction of the population produced by the various variation operators is set manually by the user. It turned out that good convergence properties are obtained by keeping the fraction of heredity-produced structures comparatively high ($\sim 50\%$), an produce more individuals by soft mutation than by lattice mutation operators. In order to maintain the diversity continuously on a high level, a small fraction of structures is produced randomly using space group symmetries.

3.3.4 Halting criteria

As in every iterative method, the evolutionary cycle is repeated until some halting criteria has been achieved. A possible exit condition would be to stop the cycle if a maximum number of generations has been produced. An even better method is to stop if the best structure hasn't changed over a number of generations.

A different approach involves the use of fingerprint functions (3.5) and the quasi-entropy (3.9). One can stop the loop if a certain amount of diversity is reached, or if the diversity of the structures has not changed over a predefined number of generations [109]. Alternatively, one can incorporate previous knowledge from experiment, or from a previous evolutionary run and stop the cycle if all individuals are converged to a single energy funnel. Because the energy funnels that can be reached crucially depend on the initial population, it is advisable to repeat simulations using different starting configurations.

3.4 Extensions for predicting stable stoichiometries

An extension of great relevance is the simultaneous prediction of thermodynamically stable stoichiometries, which is referred to as *variable composition technique* [109]. The basic ideas, as well as guidelines to practical implementation, are outlined in [116, 117].

Obviously, upon discarding the restriction of fixed stoichiometry, the configuration space becomes much more complex. However, with an appropriate extension of selection rules and variation operators, it is possible to obtain results of similar quality as for standard evolutionary structure prediction. One of the early successes of the method was the prediction of stable Fe-Mg compounds in the inner core of the earth [117], in agreement with the work in [118].

The first modification of the standard technique concerns the sampling of structures for the initial population. Here one samples all structures from a range of desired stoichiometries specified in the beginning. It is also possible to partially restrict the range of possible compounds. For instance, for a three-component system (A,B,C), one can sample all stoichiometries of the form: $x\mathrm{A}_{n_\mathrm{A}}\mathrm{B}_{n_\mathrm{B}} + y\mathrm{B}_{n'_\mathrm{B}}\mathrm{C}_{n_\mathrm{C}}$. The most stable structures of to the compounds $\mathrm{A}_{n_\mathrm{A}}\mathrm{B}_{n_\mathrm{B}}$ and $\mathrm{B}_{n'_\mathrm{B}}\mathrm{C}_{n_\mathrm{C}}$, from which all individuals under study can be constructed, are denoted as *boundary phases*. Within the USPEX-code, variable composition

runs can be performed within a desired range for the number of atoms in the unit cell.

Another major modification in the variable-composition technique is that the fitness evaluation as well as the selection process becomes history-dependent. Instead of the free energy, the fitness function is replaced by the free energy of the individual minus the free energy of the most stable boundary phases from the entire pool of sampled structures [109], *i.e.* the new fitness function is the history-dependent formation energy of the structures. Because of the high dimensionality of the search space, the current population is usually insufficient for representing an appropriate subspace for the whole amount of degrees of freedom. Instead, one takes into account all structures from the previous generations, and selects parents after discarding chemically similar structures by means of fingerprint functions [117].

In order to effectively scan the search space, variation operators are modified to no longer preserve the chemical constraints. The permutation operator is changed into a *chemical transmutation* operator that is allowed not only to interchange different types of atoms, but also to transform one atom type into another [109]. For variable-composition runs, a new heredity operator is introduced. First of all, heredity does no longer conserve the stoichiometry. When combing spatially-coherent slabs of two individuals with different stoichiometry, the resulting structure will consist of two chemically different blocks, and a subsequent relaxation will probably cause the structure to decompose into separated phases. Thus, many slices are cut from both parents and combined into one child [117].

3.4.1 Thermodynamically stable phases in a binary system at a given pressure

In this work we will study binary lithium-sulfur compounds at ultrahigh pressures, hence we restrict our discussion to explain how thermodynamically-stable high-pressures binaries can be obtained using the variable composition technique.

In general, for calculations at a fixed pressure, the fitness function characterizing a structure π_i is the enthalpy per atom:

$$H(\pi_i)\left[\frac{\mathrm{eV}}{\mathrm{at.}}\right] = E(\pi_i)\left[\frac{\mathrm{eV}}{\mathrm{at.}}\right] + P\left[\frac{\mathrm{eV}}{\mathrm{\AA}^3}\right] \cdot \frac{V_\mathrm{u}}{N}\left[\frac{\mathrm{\AA}^3}{\mathrm{at.}}\right], \tag{3.11}$$

where $E(\pi_i)$ is the total energy, P is the external pressure and V_u/N is the unit-cell volume divided by the number of atoms in the unit cell. In the end of the

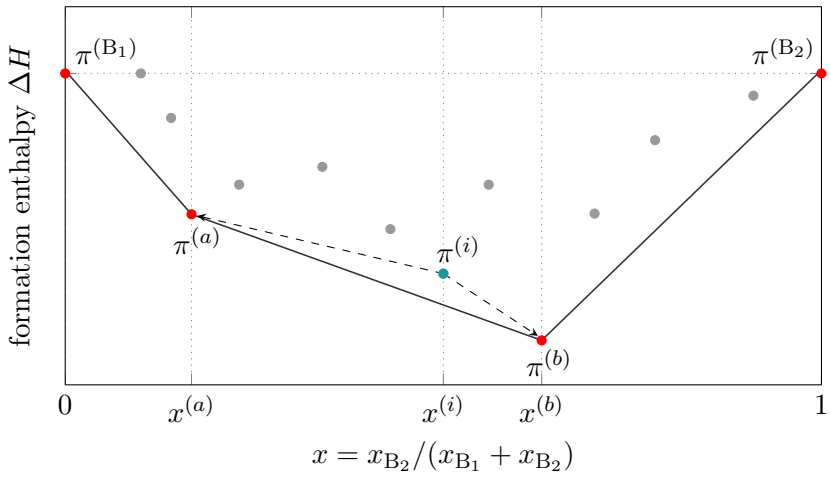

Figure 3.4: Section from a fictitious convex hull. If a structure $\pi^{(i)}$ is located above the convex hull, a linear mixture of phases $\pi^{(a)}$ and $\pi^{(b)}$ will have a lower formation enthalpy.

variable composition simulation process, the formation enthalpy with respect to the boundary phases $\pi^{(\mathrm{B}_1)}$ and $\pi^{(\mathrm{B}_2)}$ is calculated for all structures of all generations. If the stoichiometry of the structure π_i is given by: $x_{\mathrm{B}_1}\mathrm{B}_1 + x_{\mathrm{B}_2}\mathrm{B}_2$, the formation enthalpy is given by:

$$\Delta H(\pi_i) = H(\pi_i) - \frac{x_{\mathrm{B}_1} H(\pi^{(\mathrm{B}_1)}) + x_{\mathrm{B}_2} H(\pi^{(\mathrm{B}_2)})}{x_{\mathrm{B}_1} + x_{\mathrm{B}_2}}. \tag{3.12}$$

All structures for which (3.12) gives a negative value are thermodynamically stable against decomposition into the boundary phases. The data points resulting from this process are plotted against the B_2-content denoted by $x = x_{\mathrm{B}_2}/(x_{\mathrm{B}_1} + x_{\mathrm{B}_2})$. For all data points, for which $\Delta H < 0$, we draw the most convex envelope which is referred to as the *convex hull*. The situation is shown in Fig. 3.4. A sample comprising $N^{(i)}_{\mathrm{f.u.}}$ formula units of structure type $\pi^{(i)}$ will decompose into $N^{(a)}_{\mathrm{f.u.}}$ formula units of $\pi^{(a)}$ and $N^{(b)}_{\mathrm{f.u.}}$ formula units of $\pi^{(b)}$, where the ratio between the number of formula units of the neighboring phases a and b is given by a modified lever principle:

$$\frac{N^{(a)}_{\mathrm{f.u.}}}{N^{(b)}_{\mathrm{f.u.}}} = \frac{x^{(b)} - x}{x - x^{(a)}} \, \frac{x^{(b)}_{\mathrm{B}_2} + x^{(b)}_{\mathrm{B}_1}}{x^{(a)}_{\mathrm{B}_2} + x^{(a)}_{\mathrm{B}_1}}. \tag{3.13}$$

Here, $x^{(b)}_{\mathrm{B}_2}$ and $x^{(b)}_{\mathrm{B}_1}$ denote the number of $B_{1,2}$-units in the phase b. In this way, thermodynamically stable Li-S compounds are identified analyzing the formation enthalpies of all phases.

3.5 Antiseeds

A very efficient way to prevent the algorithm from being "trapped" in a local minimum is the *antiseeds technique*, presented in [111]. In most evolutionary simulations performed in this thesis, we make use of this method. The basic idea is to impose an additional evolutionary pressure on already sampled structures. The method is inspired from metadynamics simulations [111].

In the antiseeds technique the energy landscape is modified adding Gaussian functions to regions of the phase space which have been already sampled in previous runs. The method allows the algorithm to overcome energy barriers if the simulation starts to get trapped in an energy funnel. The parameters W_j and σ_j of the Gaussian depend on the history of the individuals. The fitness function $F(\pi_i,t)$ for the structure π_i at a time t is evaluated through

$$F(\pi_i,t) = F(\pi_i,t=0) + \sum_j W_j \exp\left[-\frac{d(\pi_i,\pi_j)^2}{2\sigma_j^2}\right], \tag{3.14}$$

where W_j is proportional to the fitness variance and σ_j is a user specified constant c_p multiplied with the average pair fingerprint-distance within a population: $\sigma_j = c_p \langle d(\pi_i,\pi_j)\rangle_i$ [111]. The sum runs over all stored antiseed-structures. The analogous of the antiseeds-technique in a classical evolutionary process is the ageing of the individuals. Since (3.14) is time-dependent, the fitness of the individuals is progressively reduced, causing the individuals to "die" after a certain number of generations.

Chapter 4

The Lithium-Sulfur Phase Diagram

In this chapter we outline the evolutionary predictions for the high pressure lithium-sulfur phase diagram. As already discussed in the opening chapter, the lithium-sulfur system is a natural choice for the search of high-T_c conventional superconductors, because lithium has a low mass and is chemically similar to hydrogen. The difference in electronegativity between lithium and sulfur is such that one comes to the conclusion that those atoms will form ionic bonds at ambient pressure. However, it is known that at elevated pressures the s-valence electrons of lithium hybridize into the p-orbitals [40], thus at high pressures we expect the emergence of more covalent bonds.

In this work the Li-S phase digram is investigated to pressures up to 700 GPa. Although this is almost twice the pressure in the inner core of the earth, nowadays such extremely high pressures can be attained experimentally by means of diamond anvil cell experiments [119]. The current world record from 2015 is 750 GPa, achieved in a double-stage diamond anvil cell experiment on osmium [120].

In the following sections, the method for constructing the high pressure phase diagram is outlined and the stability regimes, as well as the crystallographic properties, of the observed phases are discussed. As we will see, several novel high-pressure phases are stabilized at increased pressures. Most of the phases exhibit a metallic behavior, which leaves us with a very large pool of potentially high-T_c superconductors.

4.1 Constructing the phase diagram and computational details

The possible high-pressure stoichiometries within the lithium-sulfur system were explored by means of the USPEX evolutionary crystal structure prediction technique [12, 14, 111], extensively described in chapter 3. The underlying structural relaxations were performed using the VASP code [47, 48, 49, 50] within the generalized gradient approximation [57]. In all calculations the all-electron projector-augmented wave method was employed [61, 62]. In order to avoid core overlap in lithium at high pressures, we used a PAW-potential which treats the $1s$ and $2s$ states as valence.

For constructing the exact phase diagram, we followed a four-step process, accurately described in the following subsections. For practical purposes and because of time limitations, the search space was restricted to phases with maximally 24 atoms per unit cell, as well as to phases with 6 atoms per formula unit.

4.1.1 Investigation of the search space using the variable composition technique

In order to identify thermodynamically stable stoichiometries in the Li-S system, we performed a preliminary scan of the search space using the USPEX variable composition technique described in section 3.4. The runs were executed in the pressure range from 0 to 600 GPa in steps of 50 GPa. In order to keep the search space of a manageable size, the upper limit for the difference between the maximum an minimum number of atoms was set to 4, and several runs were performed using different ranges. In order to sample all possible stoichiometries at the respective pressures, we used pure lithium and sulfur as boundary phases of the system. The following list outlines a representative input-file for a variable composition USPEX run at a pressure of 50 GPa.

The input file 4.1 is divided in several sections, each of which controls a certain subelement of the evolutionary algorithm. The subsection `POPULATION` specifies the number of individuals per generation, the halting criteria and the details of the selection process. In all variable composition runs, a relatively large population size between 50 and 60 individuals was used. In the vast majority of phases, between 15 and 20 generations were produced by the algorithm, until convergence has been achieved. The number of best structures that survive into the next generation was defined to be 15% of the population size. The tag

```
*****************************
*   TYPE OF RUN AND SYSTEM  *
*****************************
USPEX : calculationMethod
301   : calculationType
1     : optType (1=enthalpy)
1     : AutoFrac

% atomType
Li S
% EndAtomType

% numSpecies
1 0
0 1
% EndNumSpecies

6     : minAt
8     : maxAt

*****************************
*         POPULATION        *
*****************************
55    : populationSize
70    : initialPopSize
23    : numGenerations
12    : stopCrit
 0    : reoptOld
 0.6  : bestFrac

*****************************
*     VARIATION OPERATORS   *
*****************************
0.50  : fracGene
0.20  : fracRand
0.20  : fracAtomsMut
0.10  : fracLatMut
```

```
*****************************
*         CONSTRAINTS       *
*****************************
% IonDistances
0.95   1.05
1.05   1.2
% EndDistances

*****************************
*      ANTISEED SETTINGS    *
*****************************
9     : antiSeedsActivation
0.01  : antiSeedsMax
0.005 : antiSeedsSigma

*****************************
* DETAILS OF AB INITIO CALCS *
*****************************
% abinitioCode
1 1 1 1 1
% ENDabinit

% KresolStart
0.15 0.13 0.10 0.07 0.04
% Kresolend

% commandExecutable
mpirun -np (#c) vasp >& out1
mpirun -np (#c) vasp >& out2
mpirun -np (#c) vasp >& out3
mpirun -np (#c) vasp >& out4
mpirun -np (#c) vasp >& out5
% EndExecutable

 0    : whichCluster
 1    : numParallelCalcs
50    : ExternalPressure
```

Figure 4.1: Typical USPEX input file for an evolutionary variable-composition run at an external pressure of 50 GPa. The file is devided into several subsections, each of which controls a certain subelement of the evolutionary algorithm.

`bestFrac` defines the fraction of the current population used to construct the next generation.

The segment `VARIATION OPERATORS` controls the details for the production of the next generation. The tag `fracGene` determines the number of individuals produced by heredity, 20% of the individuals are produced by soft mutation (`fracAtomsMut`) and 10% are generated using lattice mutation. In each generation, 20% of the structures were produced randomly from space groups. These settings were used for all variable and fixed stoichiometry runs. Our investigations revealed that these options exhibit good convergence properties for all investigated systems and pressure regimes.

The `CONSTRAINTS` segment contains a 2×2 matrix, specifying the smallest distance between the different types of atoms; the diagonal elements contain the distances between atoms of the same type. It turned out that these settings are very sensitive to disturbances in the performance of the algorithm, hence they have to be adjusted individually for different systems and pressures.

In order to avoid that the system gets trapped in a local energy funnel, we adopted the antiseeds technique described in section 3.5. In all simulations the automatic antiseeds activation was adopted. Here, after a certain number of generations, all structures within a population are treated as antiseeds.

For the intermediate structural optimizations, 4 consecutive relaxations with increasing precision for the energy, the forces and the $\boldsymbol{k}$-point resolution were adopted. For the first and third relaxation step the conjugate gradient method, for the second and fourth step the quasi-Newton algorithm was used. As a final stage of the process, we performed one self consistent calculation with an energy cutoff of maximally 800 eV and a $\boldsymbol{k}$-point resolution between 0.06 and $0.04\,2\pi/\text{Å}$.

At the end of the variable-composition simulation processes, the formation enthalpy with respect to pure lithium and sulfur was calculated an plotted against the sulfur content. In order to identify possible candidates for thermodynamically stable phases, we analyzed the convex hull (see section 3.4.1) of all data points.

4.1.2 Restricted evolutionary runs at fixed stoichiometry

On the basis of the results of the variable composition runs, described in the previous section, we performed additional evolutionary simulations at fixed composition, for all stoichiometries located on the convex hull. The calculations were performed in 100 GPa intervals starting from 0 GPa. Such simulations

allow a much more precise determination of stable crystal structures at a given stoichimetry.

As in the variable composition runs, we adopted the automatic aniseeds technique to panelize already sampled structures. For all fixed-composition calculations we used a population size of 50 and a maximum number of generations of 20. The maximum and minimum number of atoms were adjusted depending on the number of atoms per formula unit. As an example, for the Li_3S stoichiometry we selected a minimum number of 8 atoms and a maximum number of 20 atoms to sample the phases: Li_6S_2, Li_9S_3, $Li_{12}S_4$ and $Li_{15}S_5$. For all stoichiometries we adjusted the range for the number of atoms in such a way that between 4 to 5 different system sizes are investigated. To further ensure the correctness of the individual simulations we repeated runs at selected pressures with different ranges for the maximum and minimum number of atoms.

For the structural optimization steps we used the same procedure as for the variable composition runs. We used kinetic energy cutoffs up to 800 eV and Monkhorst-Pack $\boldsymbol{k}$-meshes with a resolution of $0.03\,2\pi/\text{Å}$.

4.1.3 Hierarchy of the crystal structures

In order to ensure the correct stability hierarchy, the best 3 structures from each fixed composition run were relaxed further with stricter convergence thresholds. To this end we performed extensive convergence tests with respect to plane-wave cutoff and $\boldsymbol{k}$-points sampling. Some of the results for the most stable high-pressure phases are summarized in the figures 4.10a - 4.11c at the end of this chapter. Here we showed the convergence of the total energy with respect to energy cutoff and the number of $\boldsymbol{k}$-points in the irreducible part of the first Brillouin zone. All plots correspond to a external pressure of 500 GPa. We used the Monkhorst-Pack scheme for generating the $\boldsymbol{k}$-meshes, as well as Γ-centered $\boldsymbol{k}$-point grids for phases crystallizing in the hexagonal and trigonal crystal systems. For a better readability we adjusted the width of the bins on the energy axis to be 2 meV on the cutoff-axis, and 0.5 meV on the $\boldsymbol{k}$-points axis. The results show that for the vast majority of phases, an energy cutoff of 1200 eV leads to a total energy convergence better than 1 meV/at.

In order to estimate reliable values for the formation enthalpy, we ensured that all forces are converged to values better than 1 meV/Å. For all investigated structures, we obtained a diagonal and isotropic stress tensor, with fluctuations in the diagonal elements smaller than 0.5 kbar. The diagonal elements of the stress tensor were used to estimate the enthalpy of the structures using equation (3.12).

4.1.4 Analytical determination of structural phase transitions

In order to evaluate the pressures where structural phase transition occur, the phases resulting from the process described in section 4.1.3 were relaxed further using the predetermined convergence parameters in pressure intervals of 50 or 100 GPa. The total energy versus volume data $E(V)$ were fit to a Birch-Murnaghan equation of state [121, 122]:

$$E(V) = E_0 + \frac{9V_0B_0}{16}\left\{\left[\left(\frac{V_0}{V}\right)^{\frac{2}{3}} - 1\right]^3 B_0' + \left[\left(\frac{V_0}{V}\right)^{\frac{2}{3}} - 1\right]^2 \left[6 - 4\left(\frac{V_0}{V}\right)^{\frac{2}{3}}\right]\right\}. \tag{4.1}$$

The pressure versus volume dependence can be obtained from (4.1) by taking the derivative with respect to volume:

$$P(V) = -\frac{\partial E}{\partial V} = \frac{3B_0}{2}\left[\left(\frac{V_0}{V}\right)^{\frac{7}{3}} - \left(\frac{V_0}{V}\right)^{\frac{5}{3}}\right] \times \left\{1 + \frac{3}{4}(B_0' - 4)\left[\left(\frac{V_0}{V}\right)^{\frac{2}{3}} - 1\right]\right\}, \tag{4.2}$$

where V_0 is some reference volume in [Å^3/at.], B_0 represents the bulk modulus, and $B_0' = \partial B_0/\partial P$. In order to obtain an analytical expression for the enthalpy versus pressure $H(P)$, we calculated the corresponding volumes for a set of desired pressures by numerically searching for the zeros of Eq. 4.2. Subsequently, the expression $H(P)$ was used to accurately determine the stability regimes of the different phases.

4.2 Analysis of the Li-S phase diagram

4.2.1 Predictions for elemental lithium and sulfur

Before discussing the novel phases predicted by our evolutionary search, show that our calculations reproduce accurately literature results for elemental lithium and sulfur, as well as for the only known stable lithium-sulfur compound Li_2S.

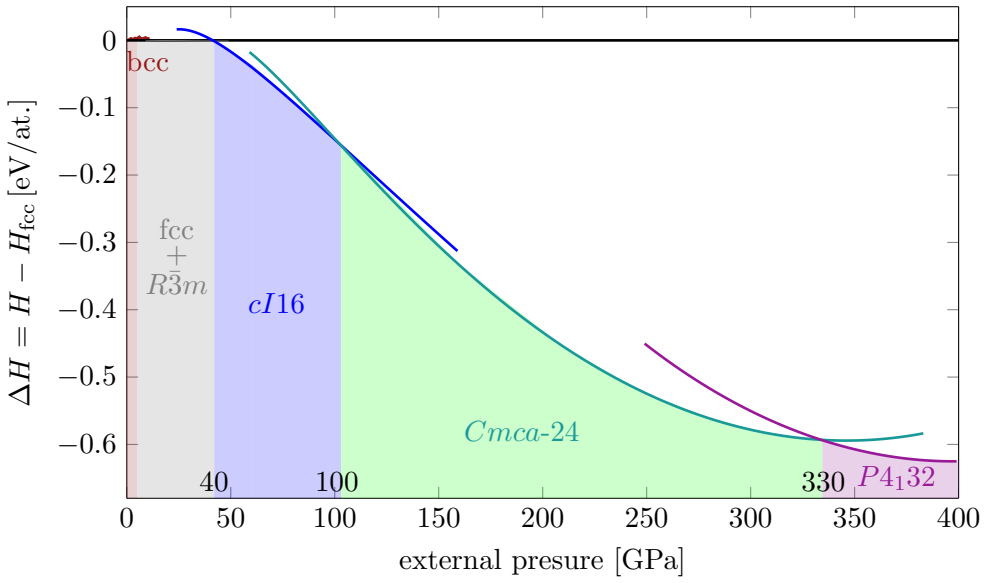

Figure 4.2: Enthalpy difference of the different lithium phases with respect to the fcc phase, calculated from fitting the data to a Birch-Murnaghan eqution of state.

For elemental lithium, we performed extensive fixed-composition evolutionary runs in pressure intervals of 50 GPa. To identify thermodynamically stable phases, we applied the process described in section 4.1.3 and 4.1.4. The results essentially reproduce the predictions in [123]. Fig. 4.2 shows the predicted high-pressure phase diagram of elemental lithium. The standard bcc-phase gets destabilized at very low pressures, and transforms into an fcc structure. In the pressure interval from 20 to 40 GPa, the difference in energy between the fcc phase and the trigonal $R\bar{3}m$ phase is less than 1 meV/at., which is smaller than our calculation accuracy. At 40 GPa we observe a transition to a cubic $cI16$-phase (space group $I\bar{4}3d$) with 16 atoms per unit cell. The existence of this structure was confirmed experimentally in [37]. The structure can easily be derived from the bcc lattice: The bcc lattice can be seen as a packing of non-intersecting cylinders running along the [111]-directions. A shift of the cylinders along their axis lowers the symmetry to $I\bar{4}3d$ and changes the coordination of the structure. The $cI16$ structure remains stable up to 100 GPa, where a $Cmca$-24-structure with 24 atoms in the unit cell takes over. This structure, previously predicted by other ab-initio calculations [38], can be seen as helical chains of lithium atoms, running along the long unit cell axis. Within our restrictions, we found this phase to be the most stable up to a pressure of 330 GPa. However, more recent calculations, using a larger number of atoms in the unit cell reveal the existence of two new phases in the pressure regime from 60 to 270 GPa. Using a particle swarm optimization technique, Jian Lv *et.al.*

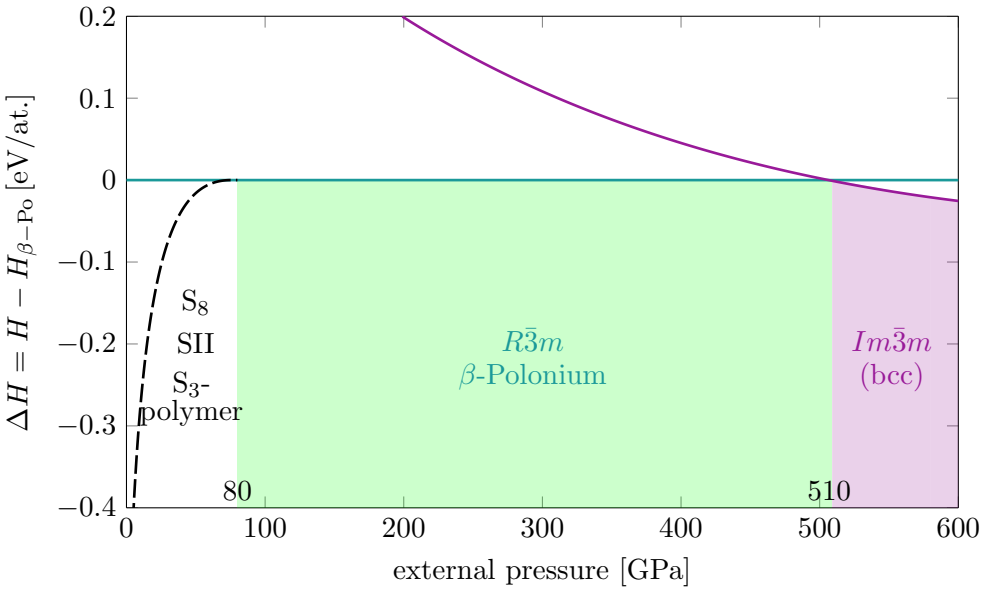

Figure 4.3: Enthalpy difference of the different sulfur phases with respect to the β-polonium phase, calculated from fitting the data to a Birch-Murnaghan eqution of state.

[39] predicted an *Aba*2-40 structure (60 to 80 GPa), and a *Cmca*-56 structure (80-270 GPa) to be more stable than *Cmca*-24. According to Jian Lv *et.al* [39], the *Cmca*-56 structure can be described as a alternated stacking of *Cmca*-24 structures with intermediate layers of the $P4_2/mbc$ type. We conclude that the difference in enthalpies are too small to affect the convex hull at high pressures. The stability range of the *Aba*2-40 is comparatively small, hence it can be ignored for the subsequent investigations. At a pressure of 330 GPa, we observe a transition to cubic $P4_132$ phase with 4 atoms per unit cell. This structure was extensively investigated in [123]. The phase displays interstitial localization of electron pairs as observed in the other Li-phases in certain pressure regimes. Our investigations suggest that this phase remains the most stable up to pressures of at least 700 GPa [2].

The high-pressure behavior of elemental sulfur is one of the most complex of all elements. There are still many open questions concerning the exact stability regimes and structural details [124]. In order to investigate the sulfur phase diagram in the pressure regime from 0 to 100 GPa, we performed USPEX fixed composition runs with steps of 10 GPa. The resulting lowest enthalpy structures were relaxed further with stricter convergence thresholds and fitted to a Birch-Murnaghan equation of state. The resulting phase diagram is shown in Fig. 4.3. At ambient pressure, we observed the well known α-sulfur phase consisting of S_8 molecular rings. Because of the large volume inside the rings,

this phase is very unstable upon compression and transforms into a polymeric phase consisting of spiral trigonal chains [2]. In reference [12], this is referred to as the SII-phase. At pressures of approximately 20 GPa we predicted a phase consisting of polymers made up from S_3 molecules as the most stable [2]. Structurally, this phase is related to the *bco*-type high pressure allotrope of sulfur [124]. Above 80 GPa our simulations repeatedly confirmed the stability of the β-Polonium structure, whose existence has been confirmed in several experiments [125]. Despite many attempts, we could not confirm the stability of the base centered orthorhombic (bco) type structure, whose stability regime has been measured experimentally to lie within 83 and 162(5) GPa [126, 125]. At pressures of approximately 510 GPa, the β-Po structure continuously transforms into a bcc structure, stable up to the highest pressure investigated. This is consistent with previous calculations [127]. The β-Po polonium phase is a superconductor with a maximum transition temperature of 17 K at 200 GPa [128].

4.2.2 Predictions for Li_2S

The only stable compound known in the lithium-sulfur system is Li2S, crystallizing in a cubic $Fm\bar{3}m$ antifluorite structure. This material has attracted great interest in the last years, due to possible applications as a nano structured [9] or liquid [10] cathode material in battery applications. On the other hand, there is very little available knowledge on the high-pressure phase transitions in Li_2S.

Our variable-composition evolutionary simulations predicted correctly the Li_2S as the most stable structure at ambient pressure. The variable composition runs, preformed at 0 GPa, suggest that Li_2S is the only stable stoichiometry at ambient conditions. The lattice constant obtained from the structural relaxation process of $a = 5.711$ Å matches very closely the experimental observations [129].

Grzechnik *et.al.* detected a reversible antifluorite to anticotunnite phase transition at 12 GPa using Raman spectroscopy and synchrotron angle- dispersive powder X-ray diffraction [11]. In good agreement with this observation, our simulations confirmed the existence of the *Pnma* anticotunnite structure [2]. We were able to locate the transition pressure at 13 GPa. According to our calculations, the *Pnma* structure continuously transforms into a Ni_2In-type structure of space group $P6_3/mmc$ at a pressure of approximately 25 GPa [2]. This structure is an insulator until 221 GPa, where it is metalized by band overlap [2]. Fig. 4.4 shows the band gap as a function of external pressure. The calculations were performed using a kinetic energy cutoff of 1200 eV and $25 \times 25 \times 25$ Γ-centered $\boldsymbol{k}$-point grid for sampling the first Brilloin zone.

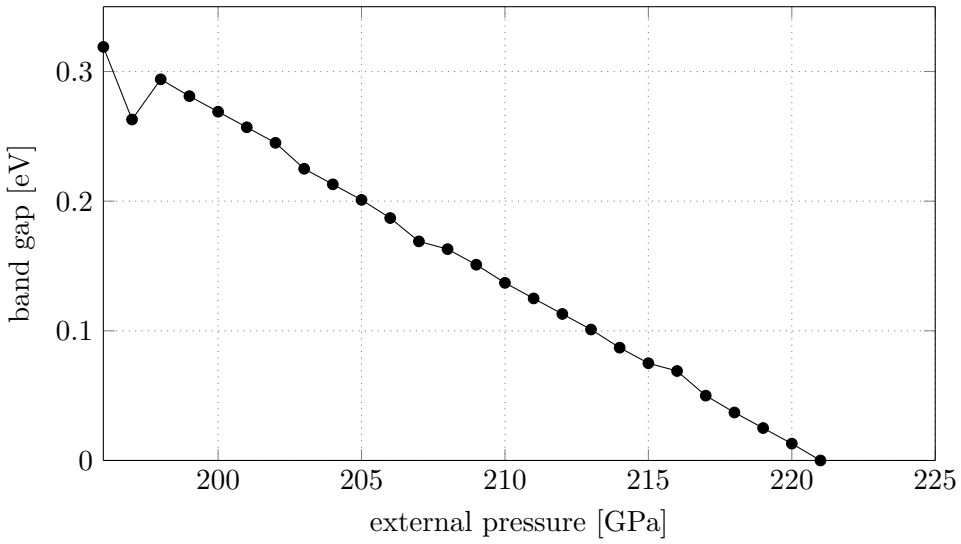

Figure 4.4: band gap against external pressure for Li_2S $P6_3/mmc$

It is noteworthy that, the observed phase transitions in Li_2S are consistent with transition sequences observed in other alkali metal sulfides like Na_2S and K_2S [130, 131]. The reversible antifluorite to anticotunnite transition is also observed in the closely related compound Li_2O [132]. A feature of this transition is that it shows a relatively large hystereses upon pressure reversal [132, 11].

4.2.3 Stability regimes and structural properties of novel high pressure Li-S compounds

The calculations performed within the variable structure prediction scheme revealed that for pressures higher than 20 GPa, several new Li-S compounds are stabilized [2]. Fig. 4.5 shows the predicted convex hulls for pressures of 0, 50, 100 and 500 GPa, including metastable phases. The formation enthalpies for the points located on the convex hulls were calculated using the analytical expression for the Birch-Murnaghan equation of state. The convex hulls indicate that within the Li-S system we find a deep formation enthalpy funnel ($\sim$ -2.3 eV/at. for $P = 100$ GPa), which means that Li-S compounds are in general energetically preferable against the boundary phases. For pressures smaller than 100 GPa, we observed several Li-rich stoichiometries like Li_7S and Li_9S. Those phases are formed by intercalating sulfur into a lithium matrix. Structures of this kind are of minor interest for further investigations of electron-phonon properties due to rare occurrence of strong covalent Li-S bonds. Thus, these structures are discarded through our restrictions of maximally 6 atoms per formula unit. In general it was discovered that phases of this type have no

significant influence on the predicted convex hulls.

As already mentioned, the transition pressures between different phases within a given stoichiometry were calculated sorting the lowest enthalpy structures according to their fitness, and fitting the data to an equation-of-state [2]. As a representative example, we show the results of this process for Li_3S in Fig. 4.6.

In the end we obtained the phase diagram in Fig. 4.7, showing the stability regimes of the different Li-S compounds in the pressure range from 0 to 700 GPa [2]. In order to determine pressures where the individual structures become thermodynamically stable, we calculated convex hulls in pressure intervals of 1 GPa, using the analytic Birch-Murnaghan equation of states, and determining the pressures where the phases start to occur on the convex hull. It can be seen that most of the phases exhibit a metallic behavior. We are thus left with a large pool of potentially superconducting structures. The electron-phonon properties of the observed structures are further investigated in chapter 5. In the following, we outline the most important crystallographic properties of the structures, starting the discussion from the Li-rich side. In figures 4.8 and 4.9, we plotted the electron localization functions of all predicted Li-S compounds at an ELF-isovalue of 0.65.

For Li_5S, we observed structures in the orthorhombic space group. Li_5S $Cmmm$ (12 atoms per unit cell) starts to appear on the convex hull at a pressure of 15 GPa. This is a very open structure, displaying a weakly metallic behavior. Hence, this structure is not investigated further in the following sections. At a pressure of $\sim$130 GPa, the $Cmmm$ structure transforms in a more closely packed $Immm$ structure, which is thermodynamically stable over a very large pressure range until 650 GPa, where it disappears from the convex hull. The electron localization function of this structure shows well separated maxima around the centers of the tetragonal faces, indicating localized interstitial electron pairs. The electron-phonon properties of this structure are discussed in more detail below [2].

The Li_4S stoichiometry only gets stabilized at extreme pressures ($P > 290$ GPa). This phase crystallizes in the trigonal crystal system with 10 atoms per unit cell, and is structurally related to Li_2S $P6_3/mmc$. Due to the low symmetry and poorly metallic behavior, this structure is not investigated further. However, we keep this phase on the convex hull because it has a strong influence on the stability regimes of the other phases [2].

The Li_3S compound is of particular interest for our investigations because it has the same stoichiometry as the high-T_c compound H_3S. Starting from a pressure of 20 GPa, Li_3S is present on the convex hull up to the highest pressure investigated. Below 225 GPa, the structure identified as the most stable is of the simple cubic $Pm\bar{3}m$-type (see Fig. 4.6) [2]. The unit cell of this structure

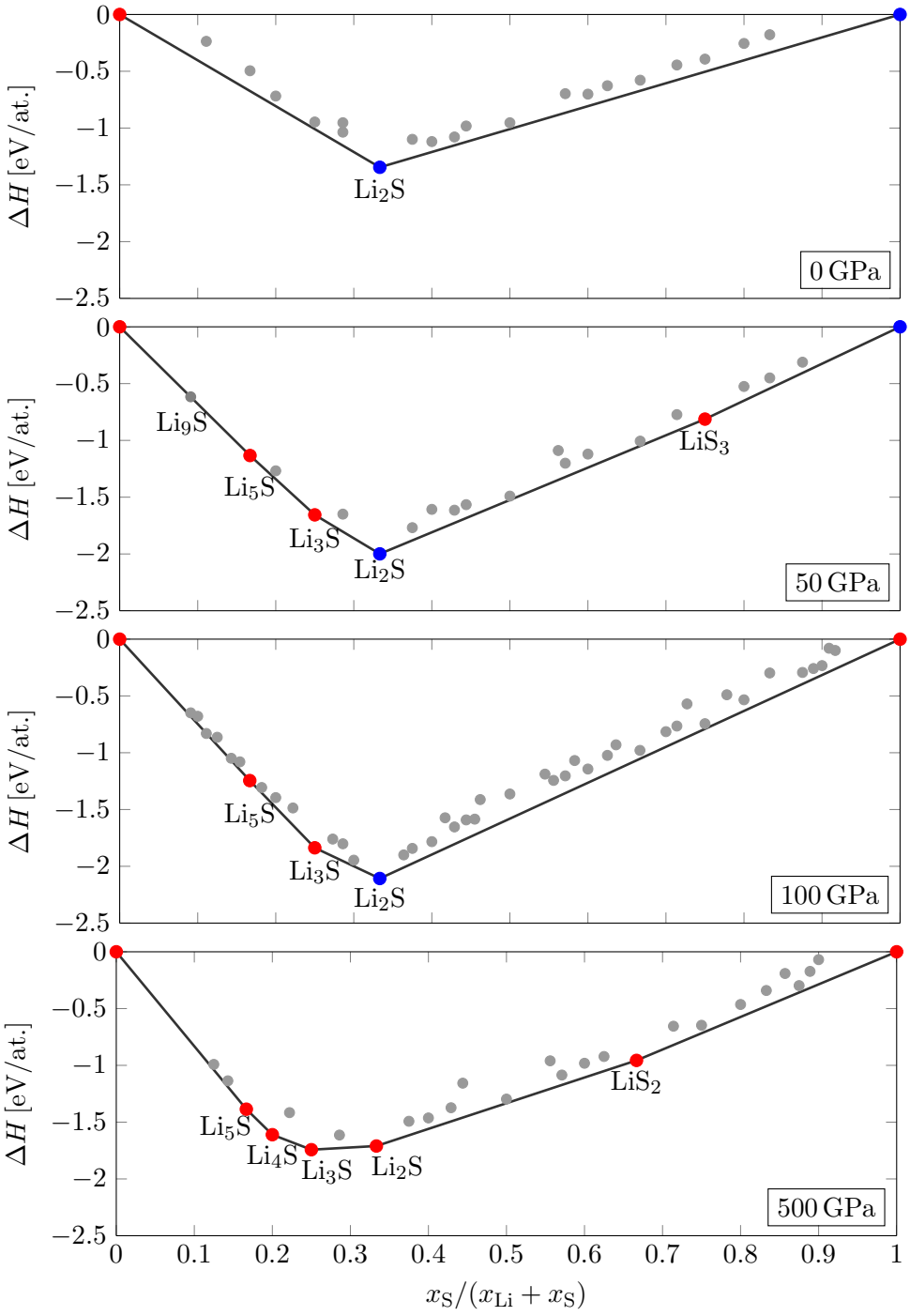

Figure 4.5: Convex hulls at pressures of 0,50,100 and 500 GPa. Red points indicate metallic, blue points nonmetallic, and gray points metastable phases.

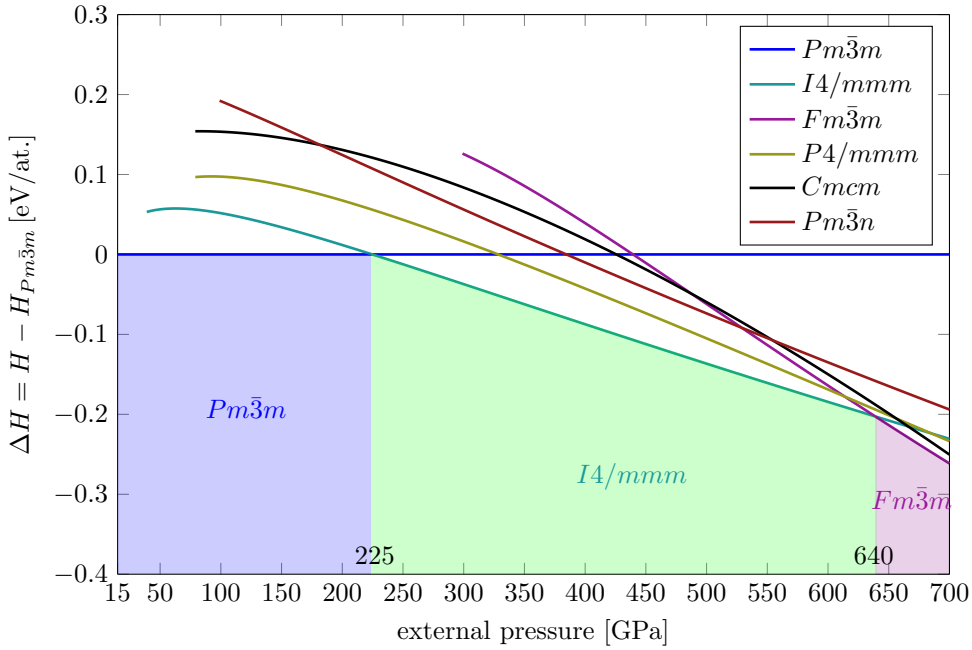

Figure 4.6: Enthalpy difference of the different Li_3S phases with respect to the $Pm\bar{3}m$ phase, calculated fitting the data to a Birch-Murnaghan eqution of state.

can be viewed as a cube where the Li atoms occupy the face centered positions, and S atoms are located at the cube corners, thus all atoms are sitting at the surface of the unit cell. As shown in Fig. 4.8, the large empty spaces are localization-attractors for interstitial electron pairs. We observe strong maxima in the ELF close to 1, corresponding to almost perfect localization. This issue is analyzed further in the subsequent sections. At 225 GPa, the $Pm\bar{3}m$ is destabilized towards a tetragonal $I4/mmm$ structure [2]. This unit cell can be described as a stacking of three simple cubic structures, in which the one in the middle is shifted by a distance of $\sqrt{3}a/2$ along the cube diagonal, where a is the short lattice parameter in the tetragonal cell. Besides the different symmetry properties, the similar interatomic distances and the tendency to interstitial charge localization relates this structure closely to the $Pm\bar{3}m$ [2]. The $I4/mmm$ structure, stable in a wide pressure range between 225 and 640 GPa, finally transforms into a high symmetry face centered cubic Li_3Bi like structure (space group: $Fm\bar{3}m$) [2]. The same structure has been reported theoretically and experimentally in the Li-N system [133]. As we will see in the following, the electronic properties of this structure are profoundly different compared to the properties of the $Pm\bar{3}m$ and $I4/mmm$ phases. This can be attributed to the high coordination and the associated suppression of interstitial electron pairs. As it can be seen from Fig. 4.8, the electron localization function

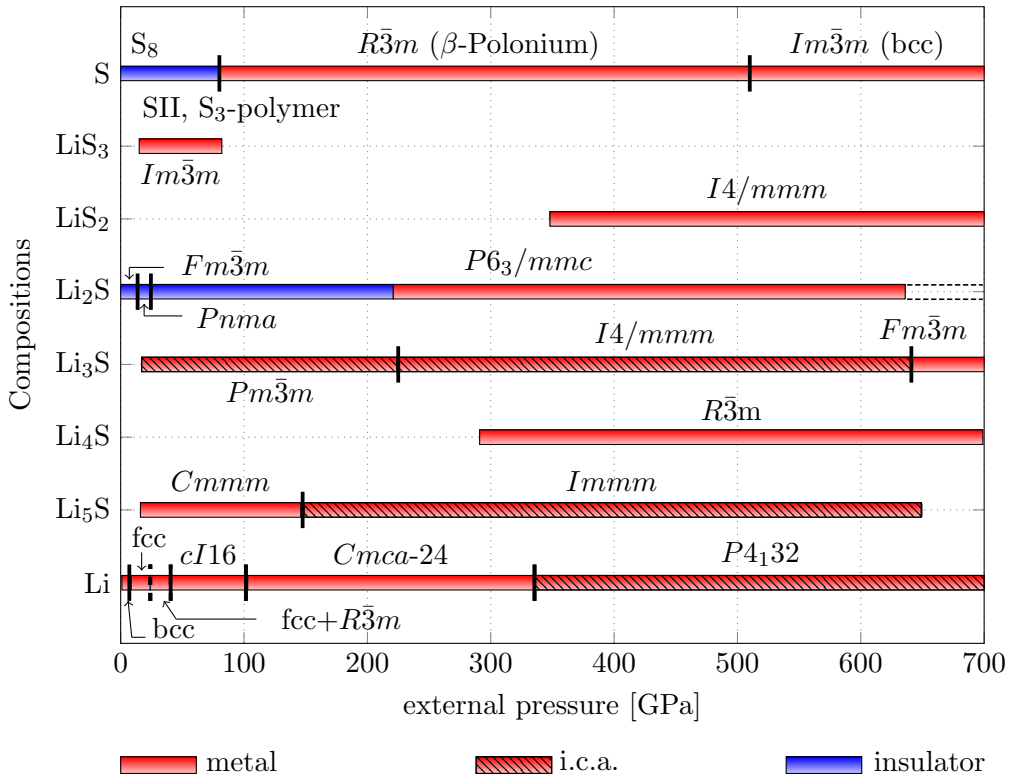

Figure 4.7: Phase diagram of the lithium-sulfur system predicted via ab-initio evolutionary search. The red shaded bars (i.c.a.) indicate metallic phases with tendency to interstitial charge accumalution. The figure is taken from [2]

shows isolated maxima accumulating along the long lithium sulfur bonds, giving them a strong covalent character [2].

On the sulfur-rich side we observed the stoichiometries LiS_2 and LiS_3, stable in two totally different pressure ranges. LiS_2, crystallizing in the tetragonal crystal system with space group $I4/mmm$, appears on the convex hull for pressures higher than 350 GPa [2]. The isocontour of the electron localization functions (Fig. 4.9) indicates that the charge is mainly localized between the sulfur atoms, forming a network in the sulfur sublattice. Thus, as we will see later in more detail, the dynamical properties of this phase are dominated from the sulfur phonons.

The LiS_3 phase is stabilized in a comparatively small pressure range between 20 and 80 GPa. This phase crystallizes in the same $Im\bar{3}m$ structure as the high-T_c H_3S, with the difference that lithium occupies the 2a Wyckoff positions of sulfur, and sulfur the 4i positions of hydrogen [2]. As in the LiS_2 case, it may be assumed that the dynamical properties of tis structure are essentially

determined by the sulfur sublattice.

In order to provide more detailed information on the structural properties, table 4.1 summarizes the Wyckoff-positions and the lattice constants of the observed phases at selected pressures.

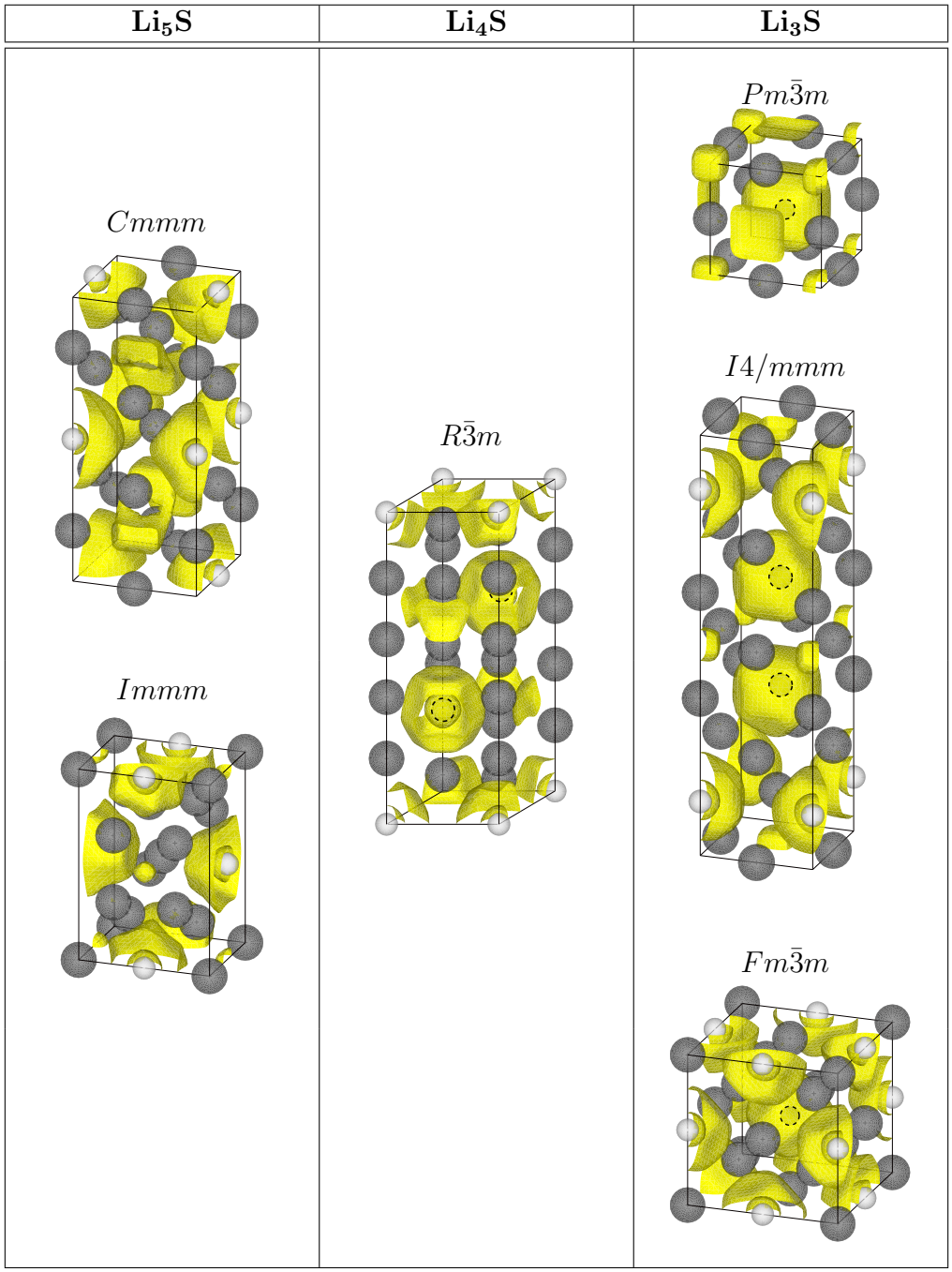

Figure 4.8: Evolutionarily predicted crystal structures for the stoichiometries Li_5S, Li_4S and Li_3S decorated with isocontours of the electron localization function at an isovalue of 0.65. Black spheres denote lithium atoms and white spheres denote sulfur atoms. The phases are shown in relative scale to each other.

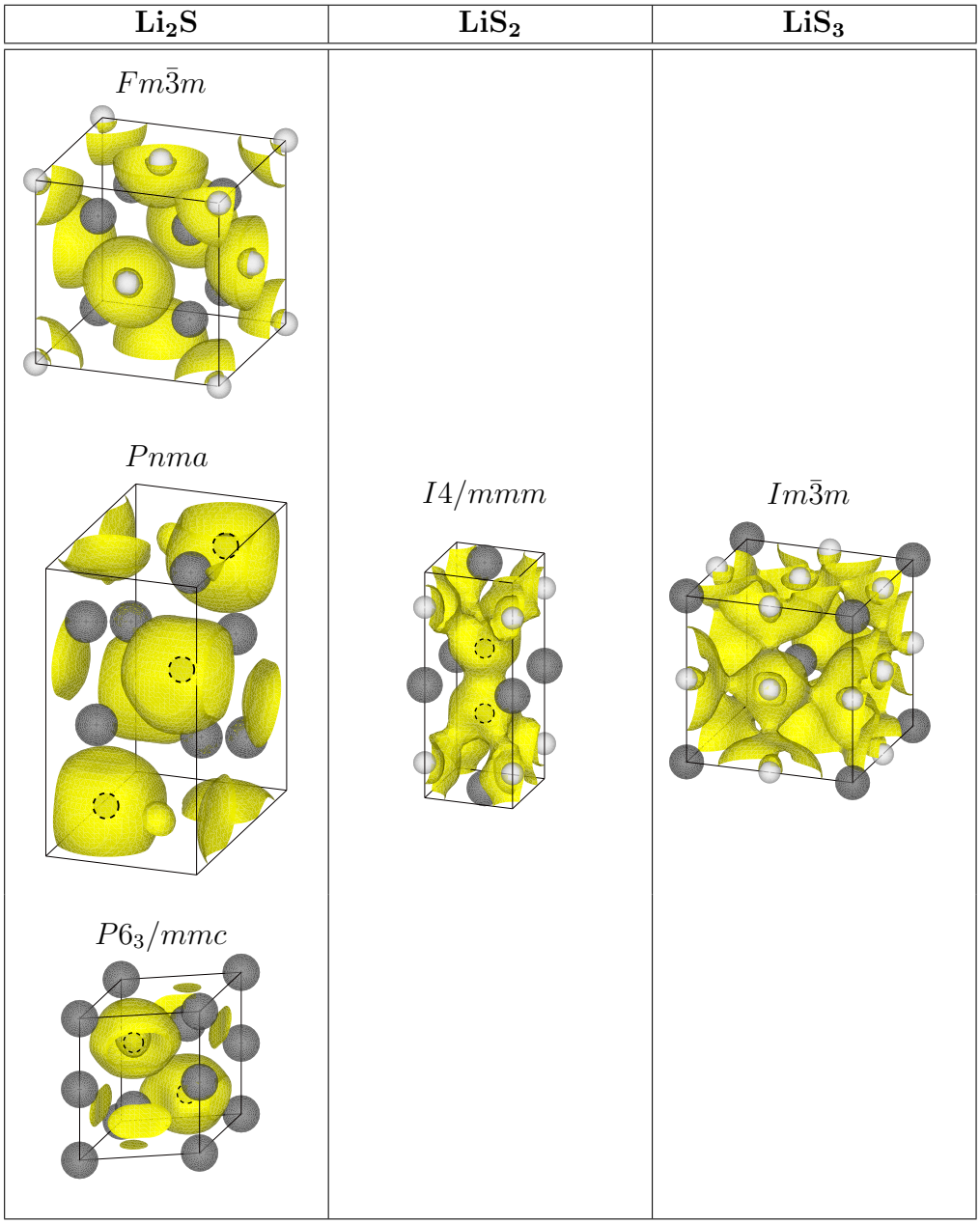

Figure 4.9: Evolutionarily predicted crystal structures for the stoichiometries Li_2S, LiS_2 and LiS_3 decorated with isocontours of the electron localization function at an isovalue of 0.65. Black spheres denote lithium atoms and white spheres denote sulfur atoms. The phases are shown in relative scale to each other.

Table 4.1: Wyckoff position and structural properties of all predicted Li-S compounds. For all presented phases, the angles between the lattice vectors are determined by the space group. Wyckoff symbols are denoted in round brackets. (The table is taken from the supplementary material in [2])

		x	y	z	**lattice parameters**
$\mathbf{Li_5S}$	***Cmmm* (100 GPa)**				
	Li(1) (4h)	0.344	0	$\frac{1}{2}$	$a = 7.457$ Å
	Li(2) (2d)	0	0	$\frac{1}{2}$	$b = 3.196$ Å
	Li(3) (4g)	-0.177	0	0	$c = 3.247$ Å
	S (2b)	$\frac{1}{2}$	0	0	
	***Immm* (500 GPa)**				
	Li(1) (8n)	-0.325	-0.265	0	$a = 4.939$ Å
	Li(2) (2a)	0	0	0	$b = 3.390$ Å
	S (2d)	$\frac{1}{2}$	0	$\frac{1}{2}$	$c = 2.542$ Å
$\mathbf{Li_4S}$	***R*$\bar{3}$*m* (500 GPa)**				
	Li(1) (6c)	0	0	-0.408	$a = 2.766$ Å
	Li(2) (6c)	0	0	0.211	$c = 8.174$ Å
	S (3a)	0	0	0	
$\mathbf{Li_3S}$	***Pm*$\bar{3}$*m***				
	Li (3d)	$\frac{1}{2}$	0	0	$a(100\,\text{GPa}) = 3.003$ Å
	S (1b)	$\frac{1}{2}$	$\frac{1}{2}$	$\frac{1}{2}$	$a(500\,\text{GPa}) = 2.504$ Å
	***I*4/*mmm* (500 GPa)**				
	Li(1) (4d)	0	$\frac{1}{2}$	$\frac{1}{4}$	$a = 2.589$ Å
	Li(2) (4e)	0	0	-0.372	$c = 9.245$ Å
	Li(3) (4c)	0	$\frac{1}{2}$	0	
	S (4e)	0	0	0.128	
	***Fm*$\bar{3}$*m* (500 GPa)**				
	Li(1) (4a)	0	0	0	$a = 3.929$ Å
	Li(2) (8c)	$\frac{1}{4}$	$\frac{1}{4}$	$\frac{1}{4}$	
	S (4b)	$\frac{1}{2}$	$\frac{1}{2}$	$\frac{1}{2}$	

Continued on next page

			x	y	z	**lattice parameters**
$\mathbf{Li_2S}$	$\boldsymbol{Fm\bar{3}m}$ **(0 GPa)**					
	Li	(8c)	$\frac{1}{4}$	$\frac{1}{4}$	$\frac{1}{4}$	$a = 5.711$ Å
	S	(4a)	0	0	0	
	$\boldsymbol{Pnma}$ **(20 GPa)**					
	Li(1)	(4c)	-0.347	$\frac{1}{4}$	0.072	$a = 5.414$ Å
	Li(2)	(4c)	-0.472	$\frac{1}{4}$	-0.306	$b = 3.442$ Å
	S	(4c)	-0.253	$\frac{1}{4}$	0.393	$c = 6.480$ Å
	$\boldsymbol{P6_3/mmc}$ **(100 GPa)**					
	Li(1)	(2a)	0	0	0	$a = 3.398$ Å
	Li(2)	(2d)	$\frac{1}{3}$	$\frac{2}{3}$	$\frac{3}{4}$	$c = 4.355$ Å
	S	(2c)	$\frac{1}{3}$	$\frac{2}{3}$	$\frac{1}{4}$	
$\mathbf{LiS_2}$	$\boldsymbol{Immm}$ **(500 GPa)**					
	Li	(2a)	0	0	0	$a = 2.269$ Å
	S	(4i)	0	0	-0.345	$c = 5.829$ Å
$\mathbf{LiS_3}$	$\boldsymbol{Im\bar{3}m}$ **(100 GPa)**					
	Li	(2a)	0	0	0	$a = 4.219$ Å
	S	(6b)	0	$\frac{1}{2}$	$\frac{1}{2}$	

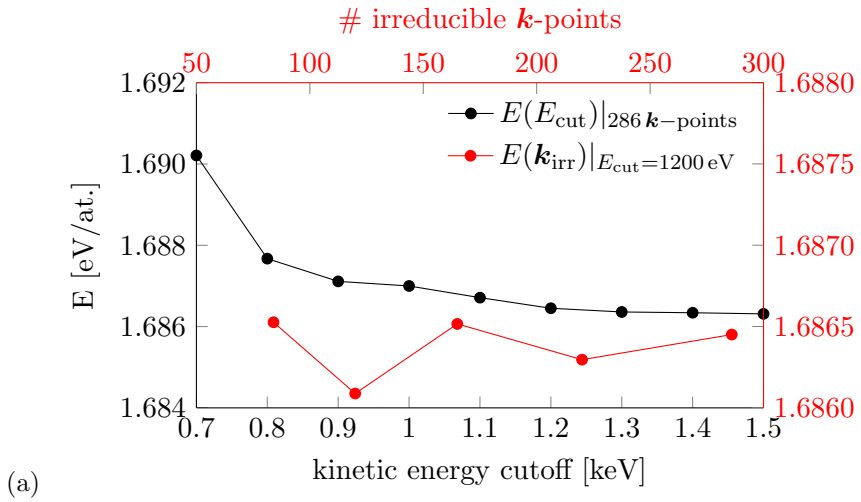

(a)

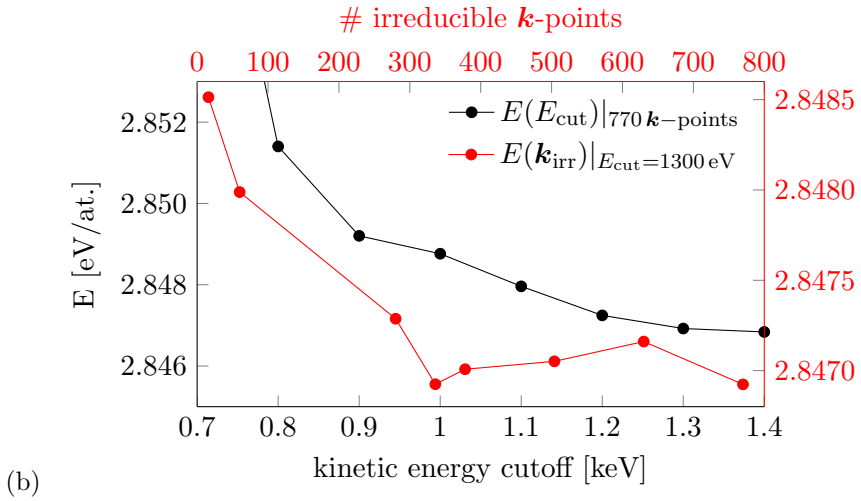

(b)

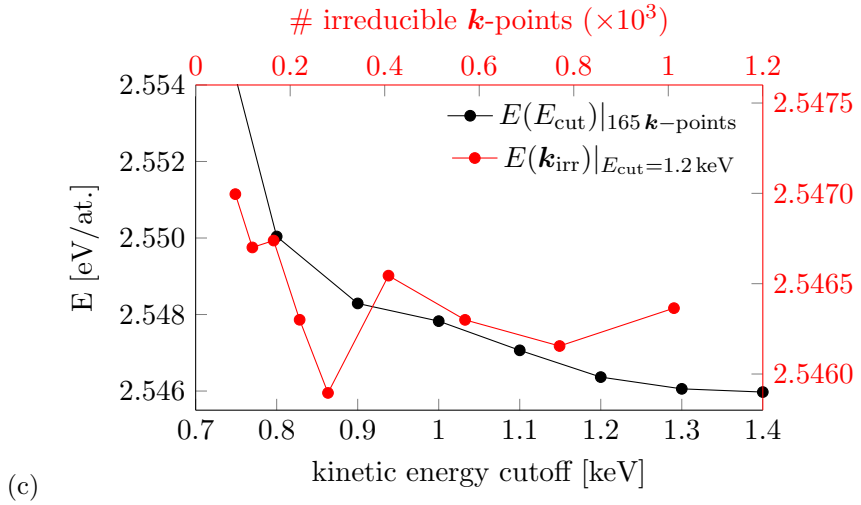

(c)

Figure 4.10: Energy cutoff and $\boldsymbol{k}$-point convergence for (a) Li ($P4_132$), (b) Li_5S ($Immm$) and (c) Li_3S ($Fm\bar{3}m$) at 500 GPa

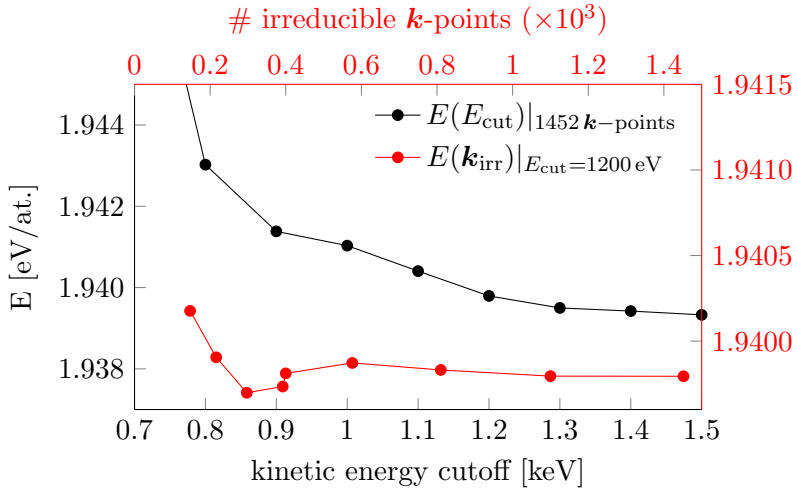

(a)

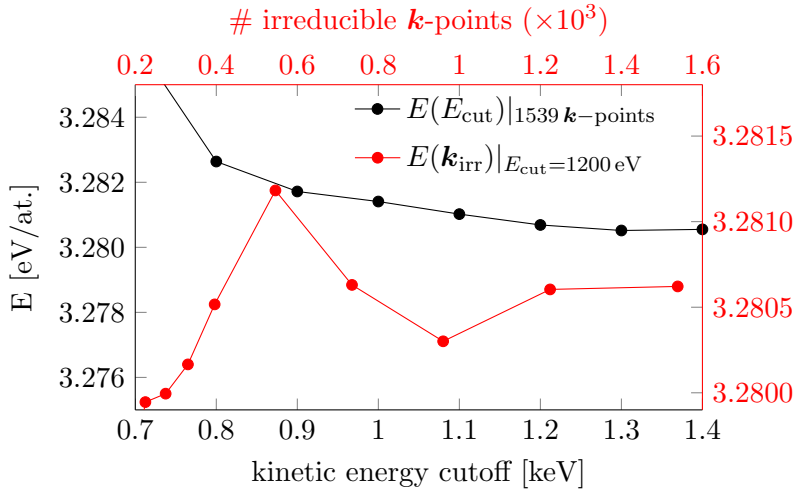

(b)

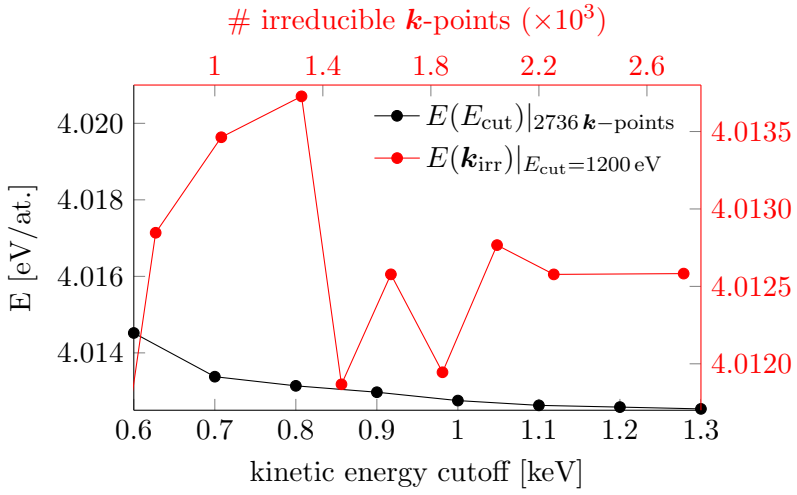

(c)

Figure 4.11: Energy cutoff and $\boldsymbol{k}$-point convergence for (a) Li_2S ($P6_3/mmc$), (b) LiS_2 ($I4/mmm$) and (c) β-Polonium sulfur at 500 GPa

Chapter 5

Electron-Phonon Properties of High-Pressure Li-S Phases

In this chapter we analyze the high-pressure compounds using density functional linear response calculations, as discussed in section 2.2. Furthermore, electronic band structures are calculated for all structures of interest. The goal of this chapter is to give an overview of the superconducting properties of high-pressure lithium-sulfur phases, as well as to explain their microscopic origin. We will partly answer the question if high-pressure compounds based on lithium are a promising choice for the search of high-T_c conventional superconductors.

The chapter is divided into three parts: In the first section we outline the physics of high-pressure lithium compounds, which underlies their fascinating properties. The second part presents a summary of the obtained properties and their relation to high-pressure hydrides. As we will see, there is a fundamental counter-intuitive difference to high-pressure hydrides that is not explainable by simple arguments based on the different ionic masses of lithium and hydrogen. In the last part we give an extensive explanation of the observed properties analyzing the electronic structures and the electron-phonon spectral functions.

5.1 Origin of the underlying physical properties

In the search for high-T_c lithium-sulfur compounds that are related to the observed high pressure hydrides, we focus on the Li-rich phases such as Li_5S, Li_3S and Li_2S. Obviously, it is of particular interest to analyze the Li_3S phases, because they have the same stoichiometry and electron count as the record

superconductor H_3S. In these phases, the electronic as well as the dynamical properties are largely determined by Li sublattice. As it can be seen from equation (2.94), the superconducting critical temperature implicitly depends on the mass of the ions through the logarithmic average phonon frequency. Hence, Li-rich solids fulfill at least one of the conditions, necessary to observe high superconducting transition temperatures, *i.e.* due to the small Li mass, they have large vibrational frequencies. Besides this very important condition the nature of the electronic states at the Fermi level and their intrinsic coupling to phonons plays a crucial role in order to observe conventional superconductivity. The behavior of those quantities, can be partially understood by analyzing the high-pressure properties of elemental lithium. The following very general discussion largely applies also to other alkali metals [41, 107, 123, 134].

5.1.1 Interstitial electron localization and *s*-*p* hybridization

As outlined in the opening chapter, although lithium and hydrogen have been assigned a common column in the periodic table, they display profoundly different chemical properties. Lithium, which can be considered a prototype free-electron metal, becomes more insulating under pressure, running through a metal to semiconductor to metal transition [39, 37]. This counter-intuitive behavior can be explained by *s*-*p* hybridization of the valence electrons and their associated localization into the interstitial voids of the lattice. In fact, at high pressures the alkali metals can be considered as high-pressure electrides [41]. Within some approximations these very unusual materials can be seen as ionic crystals, in which the anions are effectively replaced by interstitial electron pairs.

The increasing tendency to *s*-*p* hybridization has been investigated in [41], using ab-initio methods mimicking the external pressure using a compressed helium lattice. The reason for using helium is that it is a chemically very inert element, displaying a minimal orbital overlap even at very high pressures. This model has also been used to investigate the tendency to interstitial charge localization (see below). The *s*-*p* hybridization in lithium can easily be explained by the orthogonality condition of the $2s$ and $2p$ orbitals. The $2p$ orbitals have no nodes in the radial part of the wave functions, whereas the $2s$ orbitals have nodes. As pressure is applied reducing the lattice constant of the auxiliary helium lattice, the $2s$ as well as the $2p$ states rise in energy, but the $2p$ states rise less steeply. This is because, when the spatial extend of the wave-function is reduced due to compression, the kinetic energy of the $2p$ states rise less steeply than the energy of the $2s$ states. At a certain point, the $2p$ level drops below the $2s$ level, and electrons are transferred into the p states. A related argument for reaching

this conclusion is that the $2s$ orbitals always have a larger electron density far away from the nucleus. Therefore the $2s$ states are more destabilized upon compression [40]. Within the helium-containment model mentioned above, it has been shown that the transition pressure for lithium, where the $2p$ state falls below the $2s$ state, is achieved at approximately 100 GPa [41]. It has to be mentioned that $2s$-$2p$ hybridization usually is accompanied by an increasingly insulating behavior, which can lead to suppression of high-T_c conventional superconductivity. This is because hybridization with the p orbitals leads to a deformation of the $2s$ Fermi surface, which causes deviations from the free-electron like behavior.

In order to explain the tendency to interstitial charge localization observed in high-pressure Li-S compounds (Fig. 4.8), one can make use of a simplified model in which the localized electron pairs are viewed as *interstitial quasi-atoms*, having their own quantized energy levels [41]. Although the shape of the interstitial voids differ significantly from a sphere, Miao *et.al* [41] have shown that the low-lying eigenstates of the interstitial quasi-atoms are very well described by a "spherical container model", where the potential inside the sphere is zero, and infinite outside. Treating the corresponding eigenvalue problem is a straightforward task in quantum mechanics, and the solution can even be obtained in arbitrary dimensions [135]. The radial part of the wavefunctions are given by spherical Bessel functions, and the energy levels, depending on a principal and an orbital quantum number (n,l), can be written as follows [41]:

$$E(n,l) = z_{n,l}^2 \frac{2\pi^2}{R^2} \tag{5.1}$$

where R is the radius of the potential sphere and $z_{n,l}$ are dimensionless constants which represent the zeros of the Bessel functions. An important question is how to choose the radius R of the interstitial space in order to model correctly the energy levels of the quasi-atom. A very reasonable approach was suggested in [41]. Here a single vacancy is included in the helium-containment model which represents the interstitial quasi atom, and the radius R is written in terms of the atomic distance between the helium atoms D_0 and a cutoff radius R_c:

$$R = D_0 - R_c. \tag{5.2}$$

The radius R_c is adjusted so that the $1s$ energy of the spherical container model exactly reproduces the energy of the helium vacancy model with one electron in the interstitial space. Having specified the value of R at a certain pressure, one can compare the valence energies of the atom under study (Li), with the $1s$-state energy of the interstitial quasi-atom. For Li, as pressure is increased, the valence states of Li as well as the states of the interstitial

quasi atom both rise in energy. However, at some point (in the helium-cavity experiment approximately at 80 GPa [41]) the energy of the valence states in Li exceeds the $1s$ energy of the spherical container model, and the valence charge is transferred into the interstitial space. On can think that the electrons have less effective space on the Li sites, hence the increase in kinetic energy forces them into the interstices. This mechanism is denoted as avoided core-valence overlap because the orthogonality condition to the core-states prevents the valence electrons to maintain on the Li sites.

Obviously, the ionization potential has a large influence for the appearance of interstitial electron pairs. The more weakly valence electron are bound to an atom, the more easy it is for them to get transferred to the interstitial voids [41]. Furthermore, it has been demonstrated that high-pressure electrides are more likely observed if the s and p valence electrons are moving around a relatively incompressible core [41]. This is one of the main reasons why the high-pressure phases of lithium and sodium display an electride-like behavior. It has been demonstrated in [41] that the increase in energy is greatest for the s-orbitals, less for the p-orbitals and even less for the d-orbitals. In general, the energy dependence of the d-orbitals is relatively flat in a wide pressure range. This is the reason why some of the heavy elements with high ionization potentials don't form high-pressure electrides [41]. As pressure is increased the valence s-electrons are transferred into the next available d-orbital [41]. However, potassium (K) is an exception due to pressure induced s-band ferromagnetism [136].

In the following sections we will try to relate the exceptional behavior of the observed high-pressure Li-S compounds to their dynamical properties. We will see how the formation of interstitial electron pairs an the s-p hybridization effects the superconducting pairing.

5.2 Computational details

The dynamical properties of the predicted Li-S phases were calculated using density functional perturbation theory, as implemented in Quantum Espresso [137]. To model the correct high-pressure behavior of lithium as well as sulfur, we used ultrasoft pseudopotentials with semi-core states in the valence, generated with the Rappe-Rabe-Kaxiras-Joannopoulos method [138]. Lattice relaxations at selected pressures displayed good agreement for the lattice constants with the structures relaxed within the Vasp-code using the projector augmented wave method. In order to treat exchange and correlation effects, we used the same PBE functional within the generalized gradient approximation as in the Vasp runs.

As described below in more detail, we performed calculations at representative pressures of 100 and 500 GPa. At those pressures, several tests confirmed that the kinetic energy cutoffs of 80 Ryd ($\sim$ 1100 eV) for the wave functions, as well as 800 Ryd for the charge density gave reasonable convergence properties. We adopted an 8×8×8 Γ-centered $\boldsymbol{k}$-point grid for sampling the first Brillouin-zone and approximated the δ-functions by Gaussians using a smearing width of 0.01 Ryd. The smearing was estimated comparing the density of states at the Fermi level to calculations with the linear tetrahedron method with Blöchl-corrections.

The dynamical properties were calculated using a 8×8×8 $\boldsymbol{q}$-point mesh for sampling the Brillouin-zone. In order to calculate the phonon density of states we used the Fourier-interpolation technique described in section 2.2.2.

In order to calculate the electron phonon coupling matrix elements, we have used meshes with up to 38×38×38 $\boldsymbol{k}$-points for sampling the electronic states at the Fermi level. To find an appropriate smearing width to approximate the double δ-integral in Eq. (2.91), several calculations using different $\boldsymbol{k}$-grids were performed, using different parameters for the Gaussian smearing.

5.3 Summary of superconducting properties

Fig. 4.7 shows that there are fundamentally three different pressure regimes in the predicted high-pressure phase diagram of the lithium-sulfur system [2]:

i.) A low-pressure regime ($P < 15$ GPa), where Li_2S is the only stable compound.

ii.) An intermediate-pressure regime ($P < 200$ GPa) where new structures are stabilized. In this regime we observe the bcc LiS_3 structure, which disappears from the convex hull at a pressure of 80 GPa.

iii.) A high-pressure regime starting from 200 GPa up to the highest pressure investigated. Within this pressure range, new structures and stoichiometries are stabilized.

Since linear response calculations within the framework of density functional perturbation theory are computationally very demanding, we restrict all calculations to two representative pressures of 100 and 500 GPa and perform all calculations for phases that are stable at this pressures or in the immediate vicinity [2]. This also gives the opportunity to compare the different phases against each other. Table 5.1 summarizes our findings for all investigated Li-S compounds. The table includes the most important properties such as the logarithmic average phonon frequency, the electron-phonon coupling constant

Table 5.1: Superconducting properties of the metallic Li-S phases taken from [2]. Critical temperatures are estimated from Eq. (2.94), with $\mu^\star = 0.1$. P represents the external pressure; $\omega_{\log}$ is the logarithmic avarage phonon frequency according to Eq. (2.96); λ represents the electron phonon coupling constant (2.95); $\tilde{N}(\varepsilon_{\mathrm{F}})$ is the density of states at the Fermi level in states/Ry devided by the number of atoms in the unit cell; $\eta = \lambda/\tilde{N}(\varepsilon_{\mathrm{F}})$ represents the lattice contribution to the electron phonon coupling. The data for H_3S are taken from reference [139].

Composition	P (GPa)	$\omega_{\log}$ (K)	λ	T_{c} (K)	$\tilde{N}(0)$	$\eta = \lambda/\tilde{N}(0)$
Li_3S ($Pm\bar{3}m$)	100	754	0.08	0.0	0.62	0.13
LiS_3 ($Im\bar{3}m$)	100	409	0.52	5.4	1.45	0.36
Li ($P4_132$)	500	546	0.40	2.2	0.25	1.64
Li_5S ($Immm$)	500	420	0.53	8.6	0.48	1.10
Li_3S ($Pm\bar{3}m$)	500	702	0.25	0.0	0.67	0.37
Li_3S ($Fm\bar{3}m$)	500	773	1.43	80.0	1.67	0.85
Li_3S ($Fm\bar{3}m$)	600	826	1.01	55.9	1.30	0.78
Li_3S ($Fm\bar{3}m$)	640	842	0.90	50.1	1.20	0.75
Li_2S ($P6_3/mmc$)	500	374	0.22	0.0	0.27	0.85
LiS_2 ($I4/mmm$)	500	494	0.54	7.6	1.35	0.40
H_3S ($Im\bar{3}m$)	200	1200	2.40	180	1.83	1.31
Li_3S^{H} ($Fm\bar{3}m$)	500	1156	1.43	169	1.67	0.86

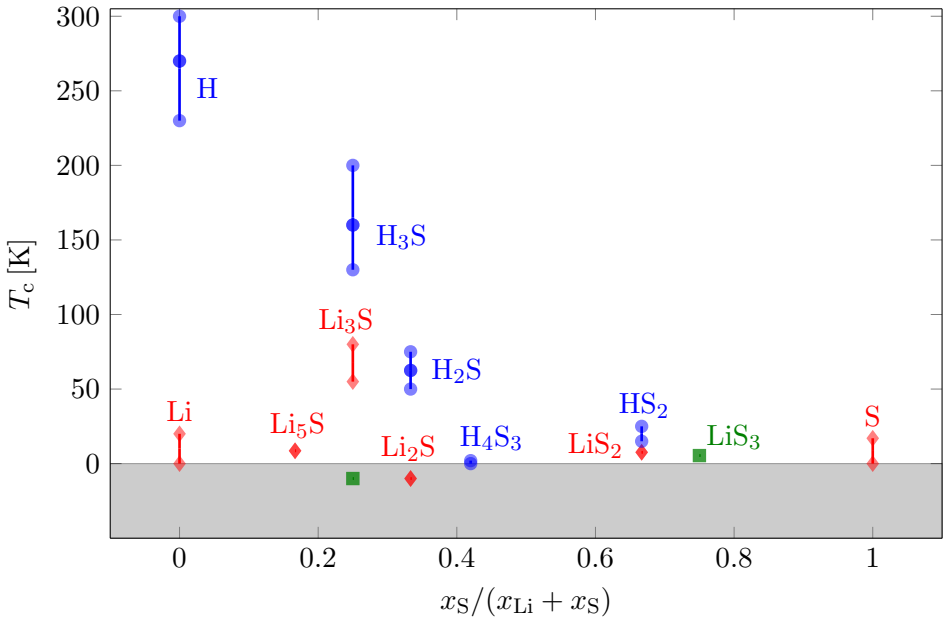

Figure 5.1: Calculated critical temperatures of Li-S compounds. The red symbols correspond to the high-pressure compounds (500 GPa); Green symbols denote intermediate pressure compounds (100 GPa); Blue symbols represent values for high-pressure hydrides as well as for elemental hydrogen, taken from the literature [140, 141]. Values inside the gray bar, plotted in the negative direction denote phases with no superconductivity. The errorbars indicate pressure variations in T_c with respect to presseure, when known. The figure is taken from [2].

and the critical temperature calculated via equations (2.94), (2.95) and (2.96). The Fermi energy is set to zero in the following considerations. The simplified Hopfield expression for the electron-phonon coupling constant:

$$\lambda = \frac{N(0)I^2}{M\omega^2} = N(0)\eta \tag{5.3}$$

where $N(0)$ is the DOS at the Fermi level, I is an average electron-phonon matrix element and $M\omega^2$ is an average lattice force constant, suggests to separate the electron-phonon coupling into a purely electronic contribution, given by the DOS at the Fermi level, and a contribution related to the crystal lattice given by η [2]. The corresponding values for η are shown in the last column of Table 5.1. In order to compare the properties to those of the hydrides, the lower section of table 5.1 includes literature values for H_3S.

Fig. 5.1 shows that only very few phases display a finite critical temperature. It is very peculiar that especially Li-rich compounds such as Li_5S, Li_3S ($Pm\bar{3}m$), as

well as high-pressure phases of pure lithium display T_c's two orders of magnitude smaller than observed for the hydrides. The only real high-T_c compound predicted by our evolutionary search is Li_3S, stabilized at pressures higher than 640 GPa [2]. At 500 GPa, the critical temperature is about 80 K. As it can be seen, we performed additional calculations at 600 and 640 GPa to investigate how the superconducting properties evolve with pressure. One observes decreasing critical temperatures that can be attributed to the decreasing DOS at the Fermi level. As it can be seen from table 5.1, the DOS at the Fermi level decreases by approximately 30% in the pressure range from 500 to 640 GPa where this structure gets stabilized. The lattice contribution to the electron-phonon coupling constant only decreases by approximately 10%.

In order to prove that this structure is directly comparable to the hydrides, we performed one calculation at 500 GPa, where we replaced the lithium by hydrogen atoms. This phase is denoted as Li_3S^H in Table 5.1. The observed critical temperature is 170 K, which is comparable to that of H_3S. However, it has to kept in mind that the pressure necessary to stabilize this structure is approximately three times higher than the corresponding pressure for the hydrides [2]. This issue is discussed in more detail in the following sections.

Looking at the properties of the other Li-rich phases, one comes to the conclusion that there is a fundamental difference in the physics underlying the electron-phonon coupling. Indeed, the extremely low critical temperatures of these phases are not explainable by a mass effect. Considering the fact that the phonon frequencies are inversely proportional to the ionic masses, one can estimate the ratio in the T_c's between hydrides and Li-rich compounds to be approximately [2]

$$\sqrt{\frac{M_{\mathrm{Li}}}{M_{\mathrm{H}}}} \simeq 2.6. \tag{5.4}$$

Obviously, as it is evident from Table 5.1, this is not the main limiting effect, responsible for the suppression of superconductivity. We will clear up this question in the following by analyzing the electronic structures, as well as the electron phonon spectral functions.

On the sulfur-rich side, both phases, LiS_2 as well as LiS_3 display moderate critical temperatures. Here the dynamical properties are dominated by S-sublattice, thus these phases are not related directly to the hydrides.

5.4 Electronic structures and Eliashberg spectral functions

In the following we will explain the origin of the observed properties in more detail, starting the discussion from Li-rich side. The band structures and the electron-phonon spectral functions are taken from the supplementary material in [2].

5.4.1 Analysis of the Li-rich high-pressure phases Li and Li_5S

According to our calculations (see Table 5.1), Li as well as Li_5S display a very small, but finite critical temperature of 2.2 and 8.6 K at 500 GPa respectively. The reason can be deduced directly by analyzing the different contributions to the electron-phonon coupling constant. Table 5.1 shows that the high pressure structures of Li and Li_5S have the highest lattice contribution to λ among all phases investigated. The reason for the suppressed superconductivity is the very low density of states at the Fermi level due to the pressure induced *s-p* charge transfer.

In Fig. 5.2a and 5.2b we plotted the band structures and the density of states for the high-pressure phases of Li and Li_5S. In addition to the total DOS, we also depicted the state-resolved, or projected, DOS (PDOS). In general this quantity is defined by

$$N_\mu(\varepsilon) = \sum_{\boldsymbol{k}\in \mathrm{IBZ}} \sum_n |\langle \phi_\mu | \psi_{\boldsymbol{k}n} \rangle|^2 w_{\boldsymbol{k}} \delta^\sigma(\varepsilon - \varepsilon_{\boldsymbol{k}n}) \tag{5.5}$$

in which $w_{\boldsymbol{k}}$ are weighting factors describing the multiplicity of the $\boldsymbol{k}$-points, $\psi_{\boldsymbol{k}n}$ are the Kohn-Sham orbitals, and $\delta^\sigma(x)$ are gaussian-smeared delta functions as introduced in Eq. (2.39). The ϕ_μ are properly chosen localized functions, whose overlap with the Kohn-Sham orbitals is given by the scalar product $\langle \phi_\mu | \psi_{\boldsymbol{k}n} \rangle$. In this way, the total DOS can be projected on different angular momentum channels, as well as on different atomic sites. In Fig. 5.2a we plotted the *s*, *p* and *d* contributions of Li ($P4_132$) to the total DOS. It has to be mentioned that the electronic properties of this structure were investigated earlier in a work from Ma *et.al.* [123]. The Li_5S $Immm$-structure includes two non-equivalent Li-atoms in the basis. In Fig. 5.2b we plotted the partial *p* and *d* contributions of the two Li-atoms as well as for S.

Fig. 5.2a shows that the Li $P4_132$ structure is a metal with a very low density of states at the Fermi level. In the whole energy range, the states are dominated

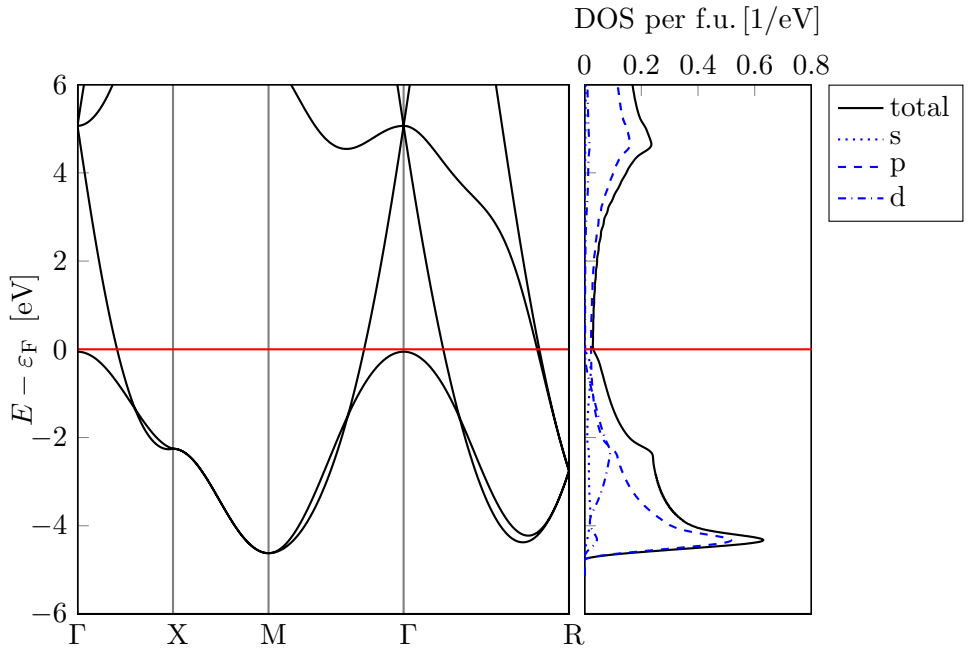

(a) **Li ($P4_132$)** at 500 GPa

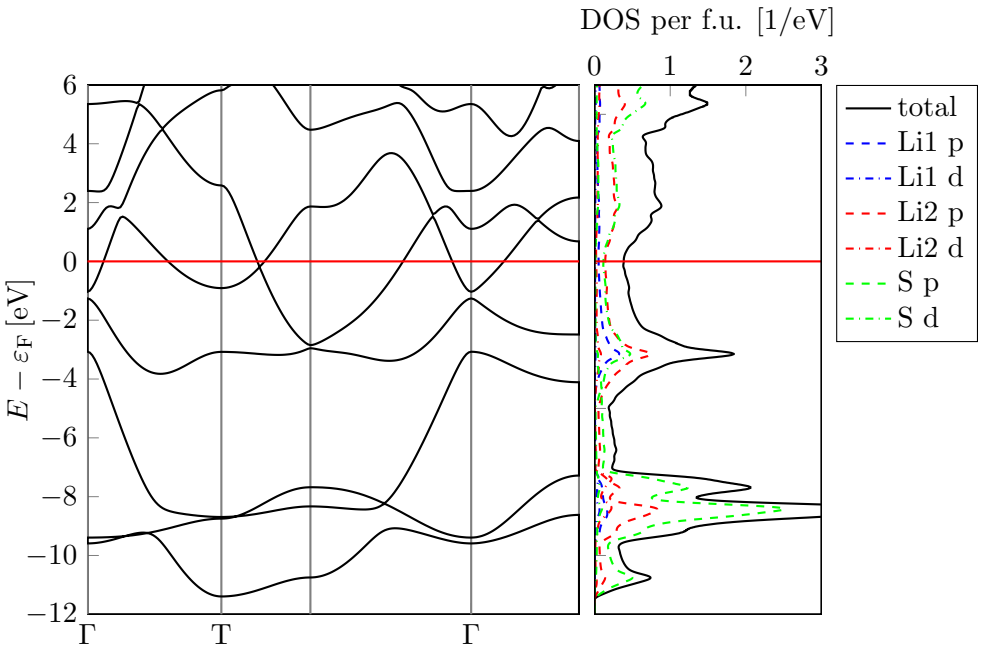

(b) **Li_5S ($Immm$)** at 500 GPa

Figure 5.2: Electronic band structures and total, as well as projected DOS on differnt angular momentum channels for Li ($P4_132$) and Li_5S ($Immm$) at 500 GPa.

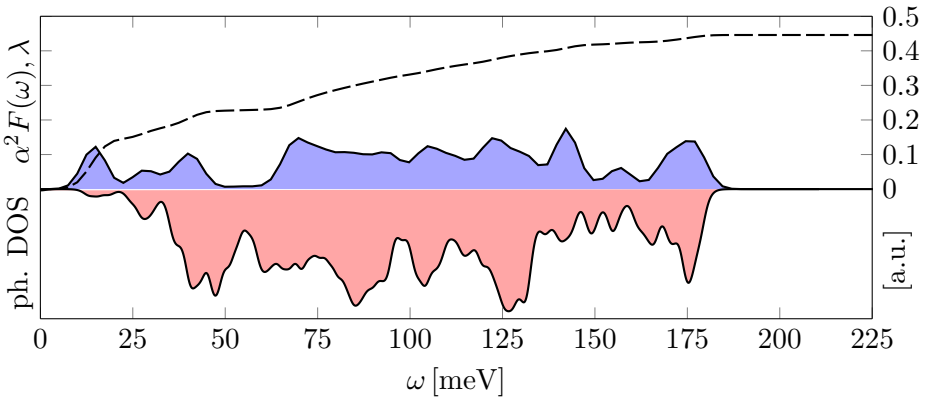

(a) **Li ($P4_132$)** at 500 GPa

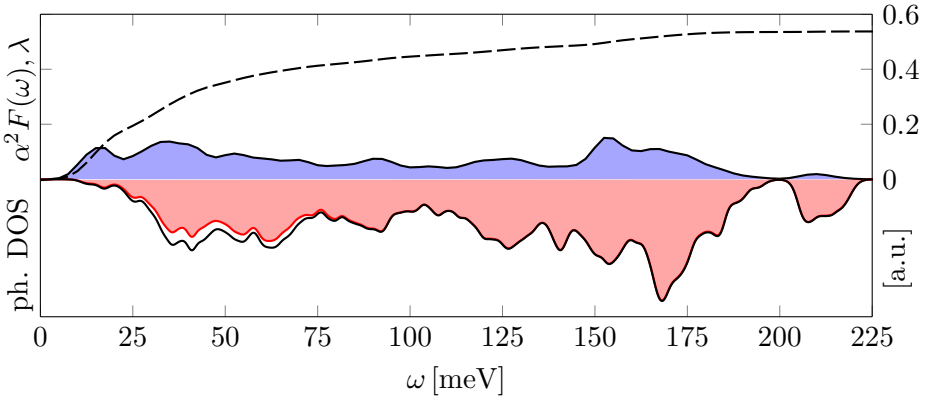

(b) **Li_5S ($Immm$)** at 500 GPa

Figure 5.3: Eliashberg electron phonon spectral functions (blue) and total DOS, as well as partial Li-contribution to the phonon DOS (red) for Li ($P4_132$) and Li_5S($Immm$) at 500 GPa. The dashed curve represents the electron phonon coupling constant, integrated up to frequeny ω.

by the p contributions. Looking at the bands at the Fermi level, it is obvious that due to the pressure-induced s-p hybridization, there is no trace of the free-electron behavior at ambient conditions. Fig. 5.3a shows the Eliashberg spectral function according to Eq. (2.91) and the phonon density of states. The dashed line represents the electron phonon coupling constant as a function of frequency according to Eq. (2.95). The normalization of the Eliashberg function is chosen so that Eq. (2.95) is satisfied. Due to small density of states at the Femi level, the Eliashberg function $\alpha^2F(\omega)$ displays very small values over the whole spectral range [2].

Also for Li_5S, Fig. 5.2b shows that Li p-states are dominating at the Fermi level. Fig. 5.3b shows the Eliashberg function and the total as well as the

partial phonon density of states for Li. It can be seen that the dynamical properties are dominated by the Li sublattice. In conclusion, the situation is very similar as it is for elemental lithium.

5.4.2 Li_3S compounds at 500 GPa: $Pm\bar{3}m$ vs. $Fm\bar{3}m$

Interestingly, the most striking difference in the superconducting properties was observed between the low-pressure $Pm\bar{3}m$ and the high-pressure $Fm\bar{3}m$ structures of Li_3S [2]. In order to compare the electron-phonon characteristics, we present the results at a pressure of 500 GPa, where both structures are dynamically stable. We also investigated the electron-phonon properties of the simple-cubic $Pm\bar{3}m$ structure in its stability regime at 100 GPa. The calculations showed that all superconducting properties are suppressed at this pressure.

Table 5.1 shows that the $Pm\bar{3}m$ structure exhibits an extremely low electron-phonon coupling constant of $\lambda = 0.08$ at 100 GPa, which slightly increases with pressure, reaching a value of $\lambda = 0.25$ at 500 GPa. Due to the low electron phonon-coupling, superconductivity is completely suppressed in this phase. On the other hand, the high-T_c $Fm\bar{3}m$ structure displays a high electron-phonon coupling constant of $\lambda = 1.43$ at 500 GPa and $\lambda = 0.90$ at 640 GPa where it has the lowest formation enthalpy. For $Fm\bar{3}m$, large superconducting transition temperatures are observed at all pressures investigated. With respect to our findings for the high-pressure phases of elemental Li and Li_5S, Table 5.1 shows that there is a large difference in the lattice contribution to the electron-phonon coupling constant. The suppressed superconductivity in the $Pm\bar{3}m$ structure is only partially caused by the low DOS at the Fermi level. The underlying reason for this significant difference in the superconducting properties between the low- and high-pressure Li_3S phases, can be attributed to the different nature of the electronic states involved in the superconducting pairing [2].

Eq. (2.91) shows that the important states that are involved in the superconducting pairing are those at the Fermi level. If these sates have a large intrinsic coupling to phonons, as it is in covalently bound solids, large values of η and thus large λ-values will be observed [2]. In Fig. 5.4a and 5.4b we plotted the band structures, as well as the total and the projected density of states on the different angular momentum channels. Fig. 5.4a shows that the three bands located below the Fermi level can be mostly attributed to sulfur states. The band with the positive curvature that crosses the Fermi level can no longer be assigned uniquely to specific atomic contributions by analyzing the projected density of states. As we will see below, this band can be identified as an *interstitial band*, corresponding to interstitially localized electrons in real space.

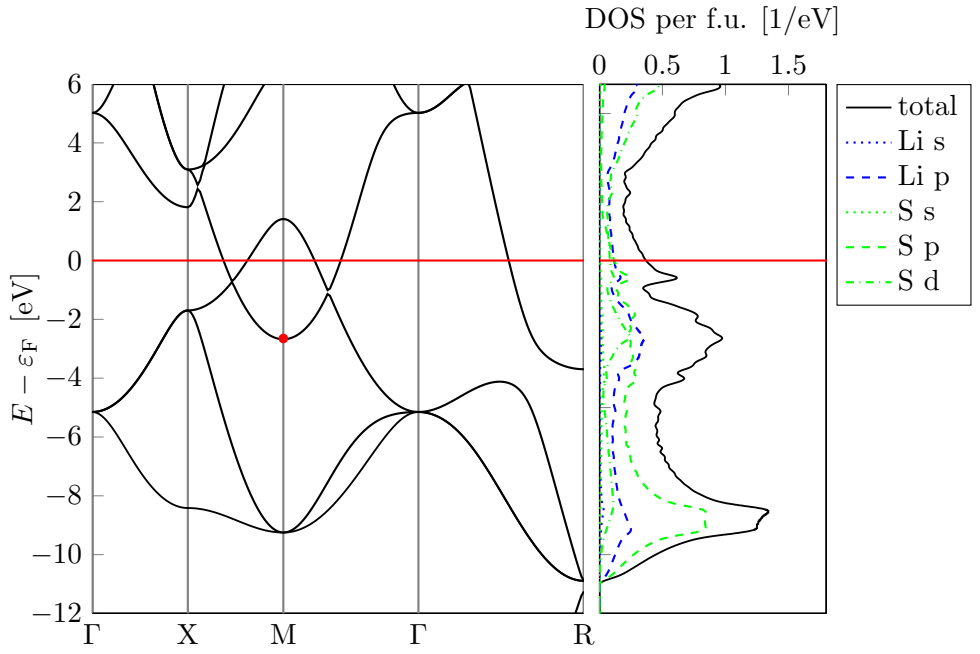

(a) **Li_3S ($Pm\bar{3}m$)** at 500 GPa

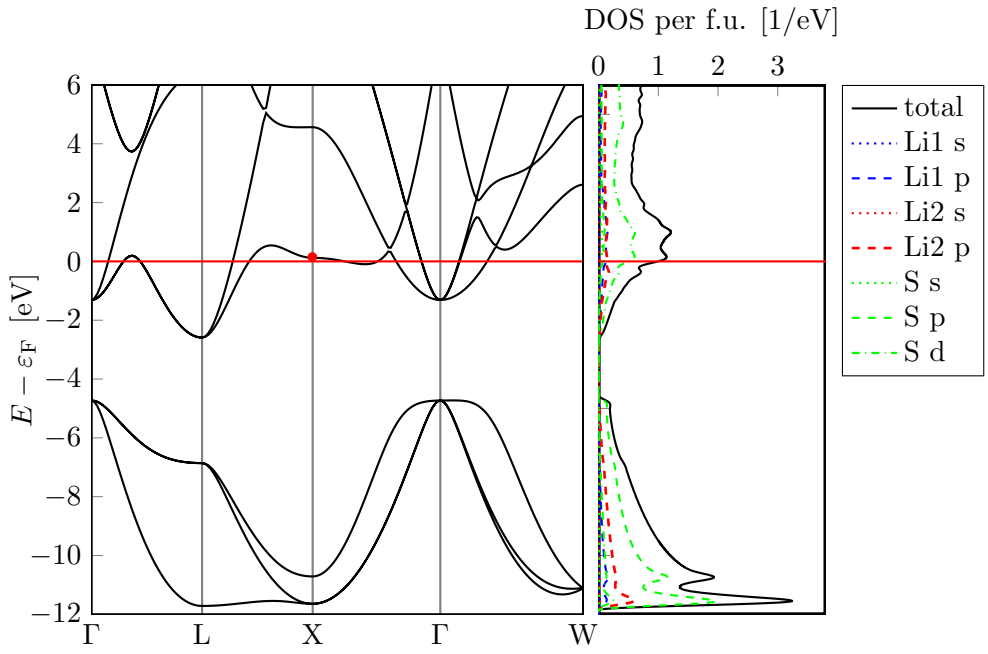

(b) **Li_3S ($Fm\bar{3}m$)** at 500 GPa

Figure 5.4: Electronic band structures and total, as well as projected DOS on differnt angular momentum channels for Li_3S ($Pm\bar{3}m$) and Li_3S ($Fm\bar{3}m$) at 500 GPa. The red points indicate states for which Kohn-Sham orbitals are plotted in Fig. 5.6.

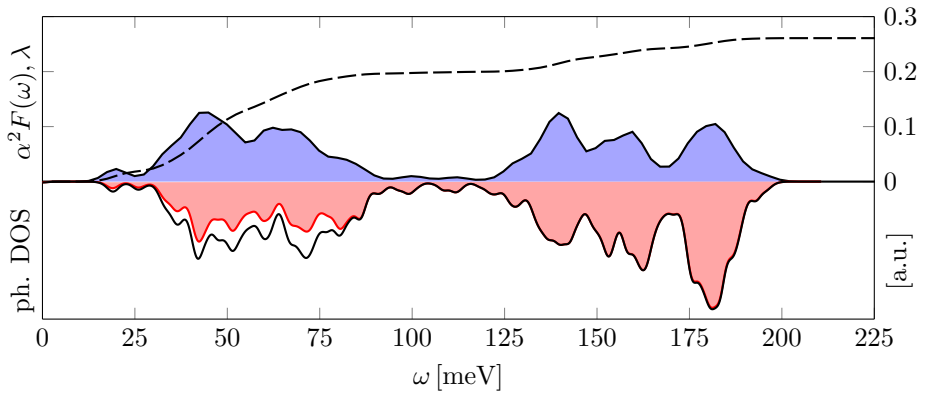

(a) **Li_3S ($Pm\bar{3}m$)** at 500 GPa

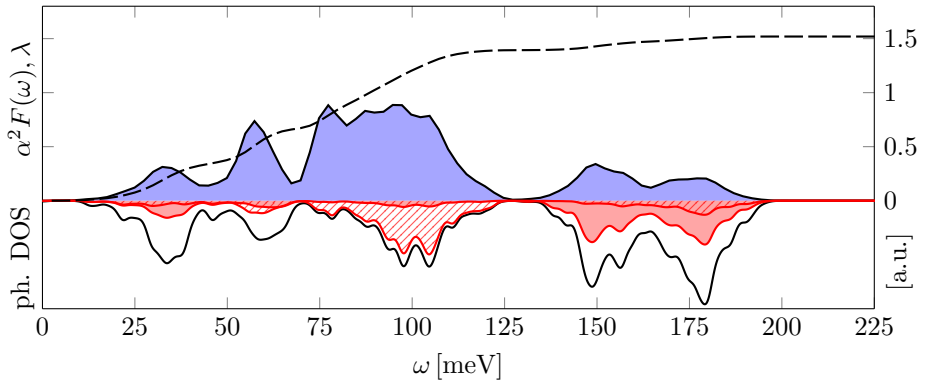

(b) **Li_3S ($Fm\bar{3}m$)** at 500 GPa

Figure 5.5: Eliashberg electron phonon spectral functions (blue) and total DOS, as well as partial Li-contribution to the phonon DOS (red) for Li_3S ($Pm\bar{3}m$) and Li_3S($Fm\bar{3}m$) at 500 GPa. The dashed curve represents the electron phonon coupling constant, integrated up to frequeny ω; The striped red function in the lower panel represent the Li2 contribution to the phonon DOS.

The $Fm\bar{3}m$ structure can be seen as layered system of alternating two-dimensional lithium and lithium-sulfur layers. Therefore there are two non-equivalent lithium atoms in the unit cell, denoted as Li1 and Li2. There are 8 atoms of the Li1 type inside the fcc cube (see Fig. 4.8). The Li2 atoms occupy the cube corners and the face centered positions within the fcc unit cell. Fig. 5.4b shows that the structure displays a comparatively high DOS at the Fermi level due low-curvature bands around the Fermi level - a situation similar as in the high-T_c H_3S compound.

Fig. 5.5a and 5.5b show the Eliashberg electron-phonon spectral functions and the partial DOS's for the two phases at a pressure of 500 GPa. Both

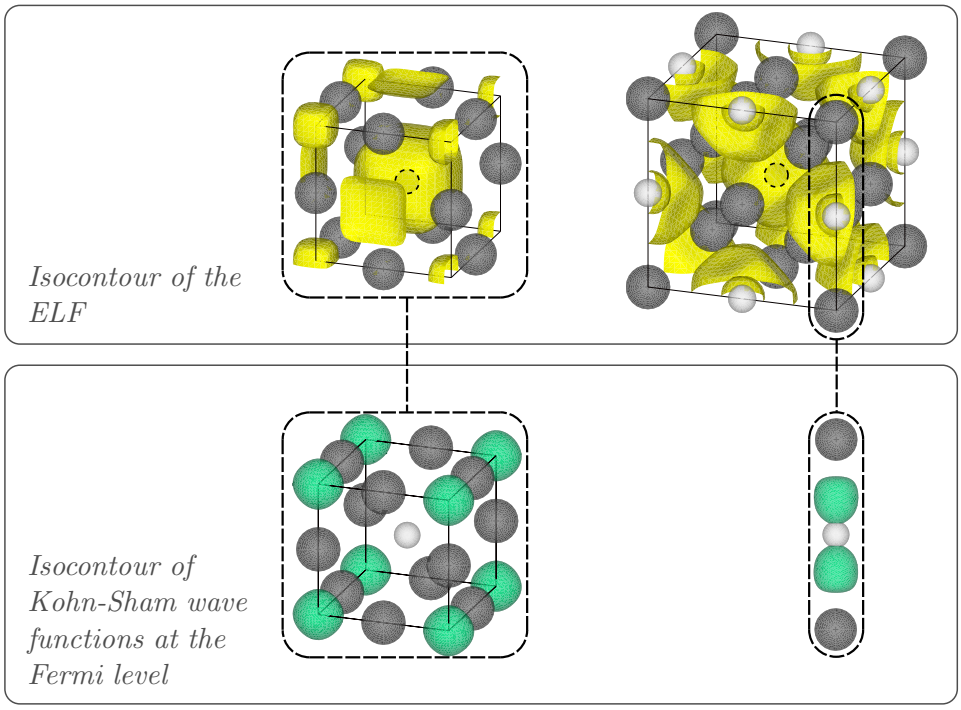

Figure 5.6: Electron localization functions (isocontour:0.65) and Kohn-Sham orbitals at the Fermi level (see Fig. 5.4a and 5.4b), for Li_3S $Pm\bar{3}m$ (left) and $Fm\bar{3}m$ (right). For $Pm\bar{3}m$ the orbitals are localized in the interstitial space; for $Fm\bar{3}m$ the orbitals localize along the long Li-S bonds on the cube edges.

spectra extend up to approximately 180 meV, but the intensity and the spectral distribution display a totally different behavior [2]. As can be seen, the $Pm\bar{3}m$-spectrum has an intensity which is about 5 times smaller than for $Fm\bar{3}m$ and displays a very uniform contribution over the whole spectral range. In contrast, the $Fm\bar{3}m$ spectrum shows a strong enhancement in the spectral region corresponding to phonon modes of Li2 atoms in the [001]-direction [2]. In order to give an optical impression of the electronic states involved in the superconducting pairing, we have choosen two representative $\boldsymbol{k}$-points, indicated by red points in Fig. 5.4a and 5.4b, and plotted the real-space Kohn-Sham wavefunctions for the states close to ε_F. Fig. 5.6 shows the orbitals together with isocontours of the electron localization function. Indeed, in the $Pm\bar{3}m$ case, the states at the Fermi level correspond to interstitial electron pairs. Since electrons localized in the interstitial voids of the lattice are barely affected by lattice displacements, very small electron-phonon matrix elements are observed. In contrast, for $Fm\bar{3}m$ the orbitals localize along the second-nearest neighbor Li-S bonds. The different nature of the electronic states leads to a significant increase in the lattice contribution η for the $Fm\bar{3}m$ structure (see Table 5.1).

The difference in λ is even more remarkable [2].

The example above has shown that pressure-induced interstitial electron localization can be an important limiting factor for conventional superconductivity, if the charge transfer affects states at the Fermi level. This is an important issue that has to be taken into account when searching for high-T_c superconductivity in high-pressure electride phases.

5.4.3 Discussion of the S-rich phases: Li_2S ($P6_3/mmc$), LiS_2 ($I4/mmm$) and LiS_3 ($Im\bar{3}m$)

In the following we compactly summarize the properties of the remaining phases on the sulfur-rich side (see Fig. 4.8). In Fig. 5.7, 5.8a and 5.8b we plotted the bands along the high symmetry directions in the first Brillouin and the projected DOS's as for the other phases. Fig. 5.9a, 5.9b and 5.9c show the Eliashberg spectral functions.

Li_2S ($P6_3/mmc$) displays a moderate lattice contribution to the electron-phonon coupling constant. However, this phase is a semiconductor at pressures smaller than 221 GPa which has been metallized by band overlap, thus the DOS at the Fermi level and the electron-phonon coupling constant λ are intrinsically low [2].

LiS_2 and LiS_3 both display moderate critical temperatures. Fig. 5.9b and 5.9c display a clear separation between the S and the Li modes in the phonon density of states. The intensity in the Eliashberg function is very low for the Li modes, thus the coupling to electronic states at the Fermi level is very weak. Here, the low critical temperatures are mainly caused by the mass effect, *i.e* by the small logarithmic average phonon frequencies [2].

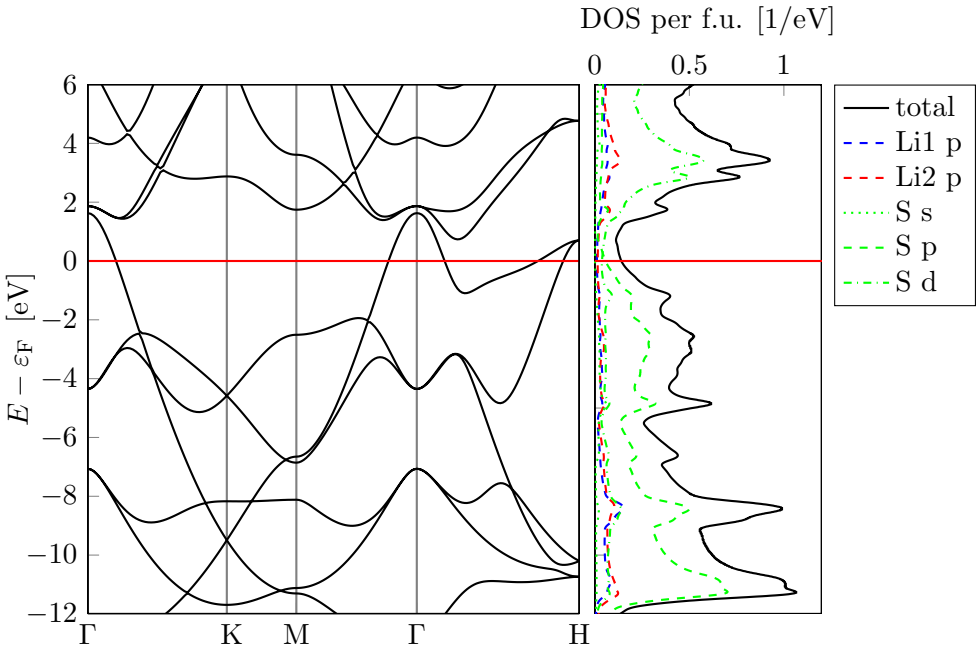

Figure 5.7: Electronic band structure and total, as well as projected DOS on differnt angular momentum channels for Li_2S ($P6_3/mmc$) at 500 GPa

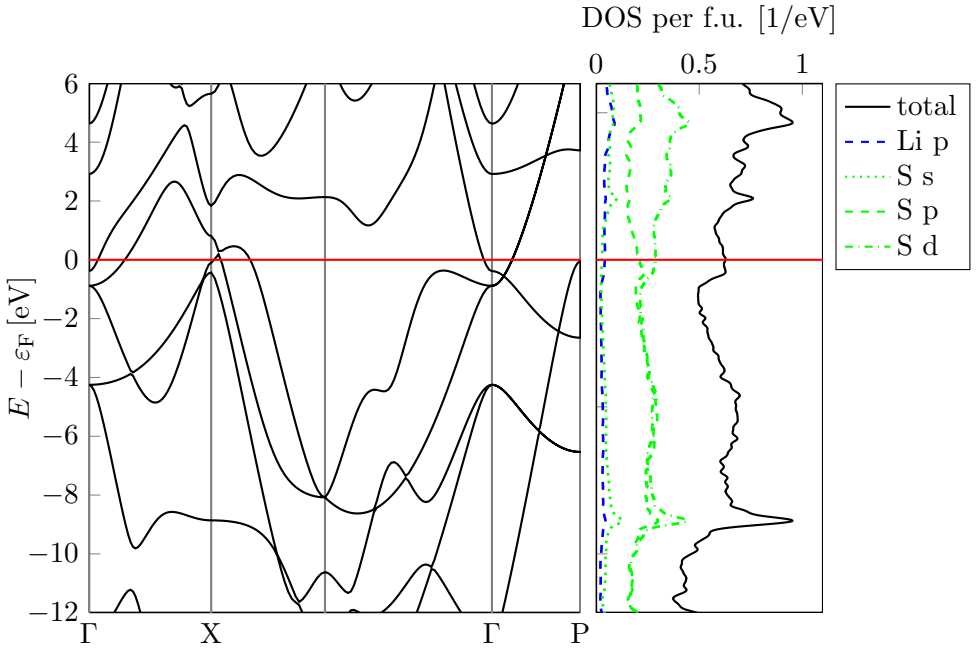

(a) **LiS_2 ($I4/mmm$)** at 500 GPa

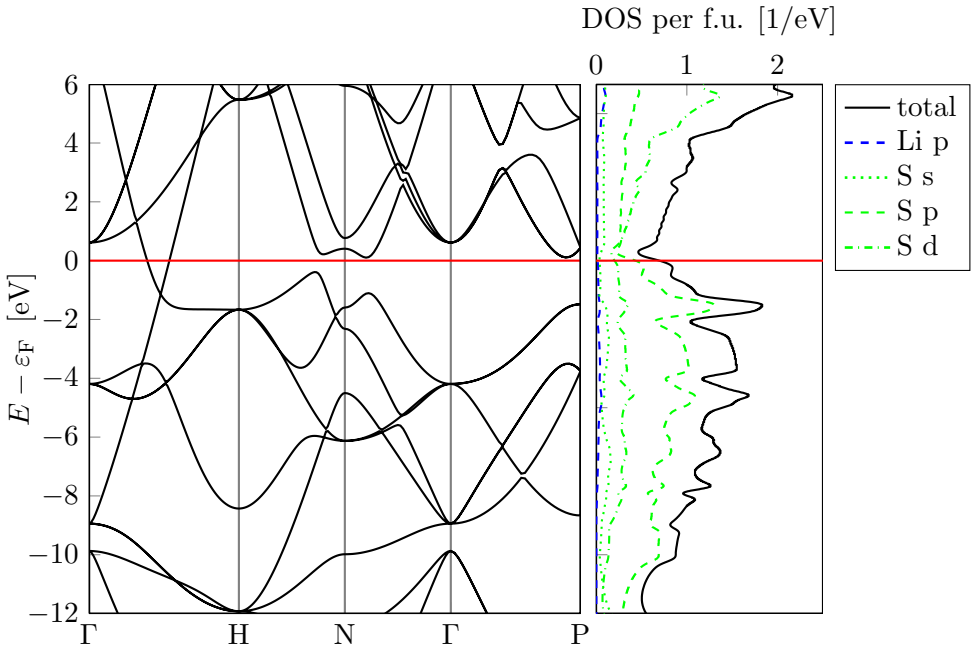

(b) **LiS_3 ($Im\bar{3}m$)** at 500 GPa

Figure 5.8: Electronic band structures and total, as well as projected DOS on differnt angular momentum channels for Li_2S ($P6_3/mmc$) and LiS_2 ($I4/mmm$) at 500 GPa.

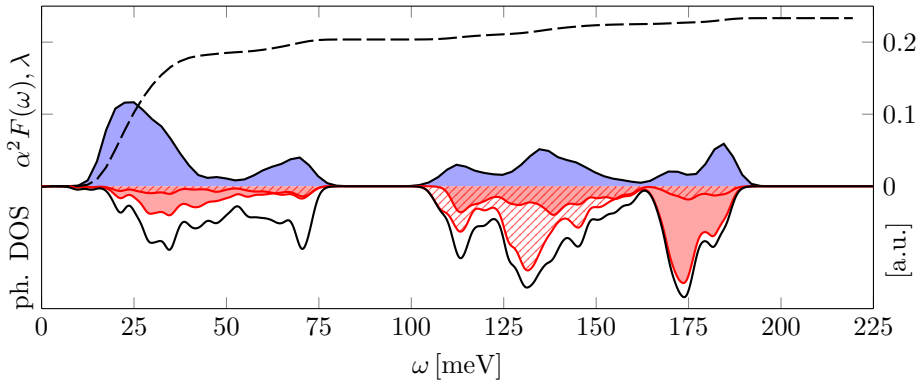

(a) **Li_2S ($P6_3/mmc$)** at 500 GPa

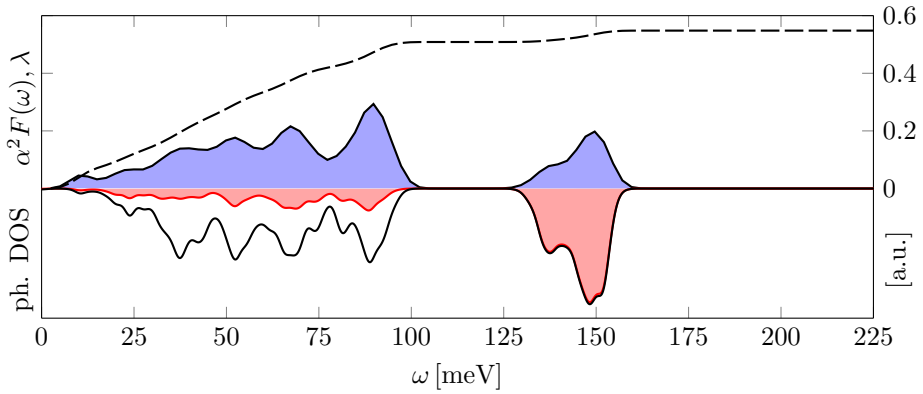

(b) **LiS_2 ($I4/mmm$)** at 500 GPa

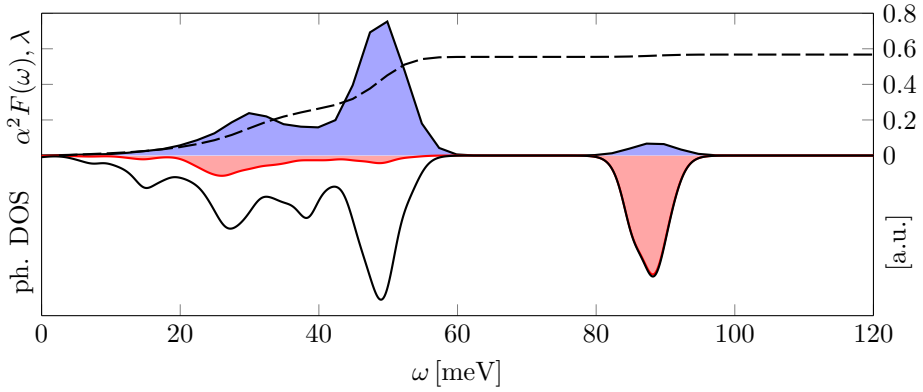

(c) **LiS_3 ($Im\bar{3}m$)** at 100 GPa

Figure 5.9: Eliashberg electron-phonon spectral functions (blue) for Li_2S and LiS_2 at 500, and for LiS_3 at 100 GPa. Phonon DOS's are plotted in negative direction. The red functions represent partial Li contributions.

Chapter 6

Conclusions

In conclusion, we extensively investigated the high-pressure Li-S system to pressures up to 700 GPa using techniques of evolutionary crystal structure prediction. Our calculations revealed that at elevated pressures several new stoichiometries become thermodynamically stable. By analytically calculating the transition pressures, we were able to obtain a high-pressure phase diagram of the system, formed by phases with a maximum of 24 atoms per cell and 6 atoms per formula unit. It has to be mentioned that the calculated phase boundaries can be shifted by taking into account the phonon zero point energies. Except Li_2S below 221 GPa, all predicted phases exhibit a metallic behavior. Most phases located on the Li-rich side of the phase diagram are high-pressure electrides, with clear maxima in the electron localization function in the interstitial space.

We investigated the superconducting properties of the predicted phases, using density functional linear response calculations. We found that most phases exhibit no or low-T_c superconductivity [2]. We attribute this behavior mainly to two detrimental effects due to the presence of core states in lithium:

i.) An increasing insulating behavior due to $2s$-$2p$ hybridization of the valence electrons.

ii.) The tendency to interstitial electron localization due to avoided core-valence overlap, which can bring states to the Fermi level that are not intrinsically coupled to lattice vibrations and cause the appearence of very small electron-phonon matrix elements.

High-T_c conventional superconductivity as in the hydrides was only observed in the Li_3S $Fm\bar{3}m$ structure, where the external pressure is high enough that close-packed structures with extremely low specific volume are energetically preferable with respect to electride phases. This phase displays a critical

temperature of 50 K at 640 GPa, where it is thermodynamically stable, which increases to 80 K at 500 GPa. One has to note that the stability range of this phase could be changed by large anharmonic effects, as observed in the hydrides [28].

We thus find that high-T_c conventional superconductivity can be observed in Li-rich compounds. However, the tendency of $2s$-$2p$ hybridization and the associated localization of electron pairs in the interstitial region will limit the possible range of pressures an dopings.

As an outlook for future investigations we suggest the extension to ternary systems. It is easy to see, that atoms with smaller ionic radii could easily fit into the interstitial voids of the Li-S lattice. Therefore, the ternary H-Li-S system would be a natural choice. Because of the comparatively high electronegativity of hydrogen with respect to lithium, we don't expect that hydrogen atoms will force the charge away from the interstitial space. However, if the charge is localized on the hydrogen-sites, large electron-phonon matrix elements could be observed due to lattice vibrations in the hydrogen sublattice.

The ideas described in the paragraph above should in principle be applicable to other H-Li-X ternaries. As described by Zurek *et.al* [5], a small amount of lithium can significantly reduce the metallization pressure of hydrogen. Hence, H-Li-X ternary compounds are an interesting alternative to search for high-T_c conventional superconductivity. Additionally, the hybridization of the $2s$-orbitals in lithium can produce Fermi surface nesting effects, which could possibly enhance the superconducting properties, as it is the case in pure lithium.

Acknowledgements

Everyone who has created a master thesis is familiar with the ups and downs associated with it. The uncounted hours where things didn't work, and the setbacks when calculations went in a wrong direction. On the other hand it is a great occasion to look deeper into a special field of interest. I would like to express this experience in Murray Gell-Mann's words:

> *Enthusiasm is followed by disappointment and even depression, and then by renewed enthusiasm.*

At this point, I would like to thank all those who supported me during the last few years, and in the process of creating the thesis.

First of all, I would like to express my gratitude to my supervisor Dr. Lilia Boeri, who gave me the opportunity to work on this very interesting topic and enabled me to produce my first scientific publication. She always had time for inspiring discussions and has been a great supervisor.

Second, I would like to thank Christoph Heil for his substantial support especially at the beginning of the thesis and for his valuable suggestions. He made significant contributions to awake my interest in the field.

Special acknowledgements go to my good friend Richard Meister, who always had an open ear for my problems. His ingenious ideas enabled me to avoid some detours.

Last but not least I would like to thank my family and friends for their support over the last years. Special gratitude goes to my girlfriend Mia and my mother Judith with Gustl as well as to my brothers Markus and Dorian. Particular thanks are directed to my grandparents Stefanie and Egon, as well as to Gudrun, Johann and Petra for always being there for me.

Bibliography

[1] D. Duan, Y. Liu, F. Tian, D. Li, X. Huang, Z. Zhao, H. Yu, B. Liu, W. Tian, and T. Cui. Pressure-induced metallization of dense (H2S)2H2 with high-Tc superconductivity. Scientific Reports, **4**:6968 EP – (Nov 2014). Article.

[2] C. Kokail, C. Heil, and L. Boeri. Search for high-T_c conventional superconductivity at megabar pressures in the lithium-sulfur system. Phys. Rev. B, **94**:060502 (Aug 2016).

[3] J. A. Flores-Livas, M. Amsler, C. Heil, A. Sanna, L. Boeri, G. Profeta, C. Wolverton, S. Goedecker, and E. K. U. Gross. Superconductivity in metastable phases of phosphorus-hydride compounds under high pressure. Phys. Rev. B, **93**:020508 (Jan 2016).

[4] A. P. Drozdov, M. I. Eremets, I. A. Troyan, V. Ksenofontov, and S. I. Shylin. Conventional superconductivity at 203 kelvin at high pressures in the sulfur hydride system. Nature, **525**(7567):73–76 (Sep 2015). ISSN 0028-0836. Letter.

[5] E. Zurek, R. Hoffmann, N. W. Ashcroft, A. R. Oganov, and A. O. Lyakhov. A little bit of lithium does a lot for hydrogen. Proceedings of the National Academy of Sciences, **106**(42):17640–17643 (2009).

[6] J. Feng, R. G. Hennig, N. Ashcroft, and R. Hoffmann. Emergent reduction of electronic state dimensionality in dense ordered Li-Be alloys. Nature, **451**(7177):445–448 (2008).

[7] F. Peng, M. Miao, H. Wang, Q. Li, and Y. Ma. Predicted Lithium–Boron Compounds under High Pressure. Journal of the American Chemical Society, **134**(45):18599–18605 (2012). PMID: 23088280.

[8] Y. Shen, A. R. Oganov, G. Qian, J. Zhang, H. Dong, Q. Zhu, and Z. Zhou. Novel lithium-nitrogen compounds at ambient and high pressures. Sci Rep, **5**:14204 (Sep 2015). ISSN 2045-2322. PMID: 26374272.

[9] K. Cai, M.-K. Song, E. J. Cairns, and Y. Zhang. Nanostructured Li2S–C Composites as Cathode Material for High-Energy Lithium/Sulfur Batteries. Nano Letters, **12**(12):6474–6479 (2012). PMID: 23190038.

[10] S. S. Zhang. Liquid electrolyte lithium/sulfur battery: Fundamental chemistry, problems, and solutions. Journal of Power Sources, **231**:153 – 162 (2013). ISSN 0378-7753.

[11] A. Grzechnik, A. Vegas, K. Syassen, I. Loa, M. Hanfland, and M. Jansen. Reversible antifluorite to anticotunnite phase transition in Li 2 S at high pressures. Journal of Solid State Chemistry, **154**(2):603–611 (2000).

[12] A. R. Oganov and C. W. Glass. Crystal structure prediction using ab initio evolutionary techniques: Principles and applications. The Journal of chemical physics, **124**(24):244704 (2006).

[13] C. W. Glass, A. R. Oganov, and N. Hansen. USPEX—evolutionary crystal structure prediction. Computer Physics Communications, **175**(11):713–720 (2006).

[14] A. R. Oganov, A. O. Lyakhov, and M. Valle. How Evolutionary Crystal Structure Prediction Works and Why. Accounts of chemical research, **44**(3):227–237 (2011).

[15] J. Bardeen, L. N. Cooper, and J. R. Schrieffer. Theory of Superconductivity. Phys. Rev., **108**:1175–1204 (Dec 1957).

[16] On the theory of superconductivity. In D. T. HAAR, editor, Collected Papers of L.D. Landau, pages 546 – 568. Pergamon (1965). ISBN 978-0-08-010586-4.

[17] M. Tinkham. Introduction to superconductivity. Courier Corporation (1996). ISBN 0-486-43503-2.

[18] A. Migdal. Interaction between electrons and the lattice vibrations in a normal metal. Zhur. Eksptl'. i Teoret. Fiz., **Vol: 34** (Jun 1958).

[19] G. Eliashberg. Interactions between electrons and lattice vibrations in a superconductor. Sov. Phys.-JETP (Engl. Transl.);(United States), **11**(3) (1960).

[20] J. G. Bednorz and K. A. Müller. Possible High T c Superconductivity in the Ba — La — Cu — O System, pages 267–271. Springer Netherlands, Dordrecht (1993). ISBN 978-94-011-1622-0.

[21] S. K. Bose and J. Kortus. Electron-phonon coupling in metallic solids from density functional theory. Vibronic and Electron-Phonon Interactions and Their Role in Modern Chemistry and Physics, pages 1–62.

[22] Y. Kamihara, T. Watanabe, M. Hirano, and H. Hosono. Iron-Based Layered Superconductor La [O1-x F x] FeAs (x= 0.05-0.12) with T c= 26 K. Journal of the American Chemical Society, **130**(11):3296–3297 (2008).

[23] Y. Kamihara, H. Hiramatsu, M. Hirano, R. Kawamura, H. Yanagi, T. Kamiya, and H. Hosono. Iron-based layered superconductor: LaOFeP. Journal of the American Chemical Society, **128**(31):10012–10013 (2006).

[24] Z. Huang, R. Meng, X. Qiu, Y. Sun, J. Kulik, Y. Xue, and C. Chu. Superconductivity, structure and resistivity in HgBa2Ca2Cu3O8+ δ. Physica C: Superconductivity, **217**(1-2):1–5 (1993).

[25] N. W. Ashcroft. Metallic Hydrogen: A High-Temperature Superconductor? Phys. Rev. Lett., **21**:1748–1749 (Dec 1968).

[26] P. Cudazzo, G. Profeta, A. Sanna, A. Floris, A. Continenza, S. Massidda, and E. K. U. Gross. *Ab Initio* Description of High-Temperature Superconductivity in Dense Molecular Hydrogen. Phys. Rev. Lett., **100**:257001 (Jun 2008).

[27] J. M. McMahon and D. M. Ceperley. High-temperature superconductivity in atomic metallic hydrogen. Phys. Rev. B, **84**:144515 (Oct 2011).

[28] M. Borinaga, I. Errea, M. Calandra, F. Mauri, and A. Bergara. Anharmonic effects in atomic hydrogen: Superconductivity and lattice dynamical stability. Phys. Rev. B, **93**:174308 (May 2016).

[29] M. Eremets, I. Troyan, and A. Drozdov. Low temperature phase diagram of hydrogen at pressures up to 380 GPa. A possible metallic phase at 360 GPa and 200 K. arXiv preprint arXiv:1601.04479 (2016).

[30] P. Dalladay-Simpson, R. T. Howie, and E. Gregoryanz. Evidence for a new phase of dense hydrogen above 325 gigapascals. Nature, **529**(7584):63–67 (Jan 2016). ISSN 0028-0836. Letter.

[31] N. W. Ashcroft. Hydrogen Dominant Metallic Alloys: High Temperature Superconductors? Phys. Rev. Lett., **92**:187002 (May 2004).

[32] I. Errea, M. Calandra, C. J. Pickard, J. Nelson, R. J. Needs, Y. Li, H. Liu, Y. Zhang, Y. Ma, and F. Mauri. High-Pressure Hydrogen Sulfide from First Principles: A Strongly Anharmonic Phonon-Mediated Superconductor. Phys. Rev. Lett., **114**:157004 (Apr 2015).

[33] A. Drozdov, M. Eremets, and I. Troyan. Superconductivity above 100 K in PH3 at high pressures. arXiv preprint arXiv:1508.06224.

[34] A. Shamp, T. Terpstra, T. Bi, Z. Falls, P. Avery, and E. Zurek. Decomposition Products of Phosphine Under Pressure: PH2 Stable and Supercon-

ducting? Journal of the American Chemical Society, **138**(6):1884–1892 (2016). PMID: 26777416.

[35] Y. Fu, X. Du, L. Zhang, F. Peng, M. Zhang, C. J. Pickard, R. J. Needs, D. J. Singh, W. Zheng, and Y. Ma. High-Pressure Phase Stability and Superconductivity of Pnictogen Hydrides and Chemical Trends for Compressed Hydrides. Chemistry of Materials, **28**(6):1746–1755 (2016).

[36] J. B. Neaton and N. W. Ashcroft. Pairing in dense lithium. Nature, **400**(6740):141–144 (Jul 1999). ISSN 0028-0836.

[37] S. K. C. N. E. Hanfland, M. and D. L. Novikov. New high-pressure phases of lithium. Nature, **408**(6809):174–178 (Nov 2000). ISSN 0028-0836.

[38] R. Rousseau, K. Uehara, D. D. Klug, and J. S. Tse. Phase Stability and Broken-Symmetry Transition of Elemental Lithium up to 140 GPa. ChemPhysChem, **6**(9):1703–1706 (2005). ISSN 1439-7641.

[39] J. Lv, Y. Wang, L. Zhu, and Y. Ma. Predicted Novel High-Pressure Phases of Lithium. Phys. Rev. Lett., **106**:015503 (Jan 2011).

[40] I. I. Naumov, R. J. Hemley, R. Hoffmann, and N. Ashcroft. Chemical bonding in hydrogen and lithium under pressure. The Journal of chemical physics, **143**(6):064702 (2015).

[41] M.-S. Miao and R. Hoffmann. High Pressure Electrides: A Predictive Chemical and Physical Theory. Accounts of Chemical Research, **47**(4):1311–1317 (2014). PMID: 24702165.

[42] K. Shimizu, H. Ishikawa, D. Takao, T. Yagi, and K. Amaya. Superconductivity in compressed lithium at 20 K. Nature, **419**(6907):597–599 (Oct 2002). ISSN 0028-0836.

[43] A. Rodriguez-Prieto, A. Bergara, V. M. Silkin, and P. M. Echenique. Complexity and Fermi surface deformation in compressed lithium. Phys. Rev. B, **74**:172104 (Nov 2006).

[44] I. Errea, M. Martinez-Canales, and A. Bergara. *Ab initio* study of superconducting hexagonal Be_2Li under pressure. Phys. Rev. B, **78**:172501 (Nov 2008).

[45] T. Matsuoka, M. Debessai, J. J. Hamlin, A. K. Gangopadhyay, J. S. Schilling, and K. Shimizu. Pressure-Induced Superconductivity in $CaLi_2$. Phys. Rev. Lett., **100**:197003 (May 2008).

[46] Y. Xie, A. R. Oganov, and Y. Ma. Novel High Pressure Structures and Superconductivity of $CaLi_2$. Phys. Rev. Lett., **104**:177005 (Apr 2010).

[47] G. Kresse and J. Hafner. *Ab initio* molecular dynamics for liquid metals. Phys. Rev. B, **47**:558–561 (Jan 1993).

[48] G. Kresse and J. Hafner. *Ab initio* molecular-dynamics simulation of the liquid-metal˘amorphous-semiconductor transition in germanium. Phys. Rev. B, **49**:14251–14269 (May 1994).

[49] G. Kresse and J. Furthmüller. Efficiency of ab-initio total energy calculations for metals and semiconductors using a plane-wave basis set. Computational Materials Science, **6**(1):15–50 (1996).

[50] G. Kresse and J. Furthmüller. Efficient iterative schemes for *ab initio* total-energy calculations using a plane-wave basis set. Phys. Rev. B, **54**:11169–11186 (Oct 1996).

[51] J. P. Perdew and S. Kurth. Density functionals for non-relativistic coulomb systems in the new century. In A primer in density functional theory, pages 1–55. Springer (2003).

[52] M. Levy. Universal variational functionals of electron densities, first-order density matrices, and natural spin-orbitals and solution of the v-representability problem. Proceedings of the National Academy of Sciences, **76**(12):6062–6065 (1979).

[53] F. Nogueira, A. Castro, and M. A. Marques. A tutorial on density functional theory. In A Primer in Density Functional Theory, pages 218–256. Springer (2003).

[54] A. Y. Toukmaji and J. A. Board. Ewald summation techniques in perspective: a survey. Computer physics communications, **95**(2):73–92 (1996).

[55] I.-C. Yeh and M. L. Berkowitz. Ewald summation for systems with slab geometry. The Journal of Chemical Physics, **111**(7):3155–3162 (1999).

[56] S. Baroni, S. de Gironcoli, A. Dal Corso, and P. Giannozzi. Phonons and related crystal properties from density-functional perturbation theory. Rev. Mod. Phys., **73**:515–562 (Jul 2001).

[57] J. P. Perdew, K. Burke, and M. Ernzerhof. Generalized Gradient Approximation Made Simple. Phys. Rev. Lett., **77**:3865–3868 (Oct 1996).

[58] C. Kittel. Introduction to Solid State Physics. John Wiley & Sons, Inc., New York, 8th edition (1986).

[59] D. R. Hamann, M. Schlüter, and C. Chiang. Norm-Conserving Pseudopotentials. Phys. Rev. Lett., **43**:1494–1497 (Nov 1979).

[60] K. Laasonen, A. Pasquarello, R. Car, C. Lee, and D. Vanderbilt. Car-Parrinello molecular dynamics with Vanderbilt ultrasoft pseudopotentials. Phys. Rev. B, **47**:10142–10153 (Apr 1993).

[61] P. E. Blöchl. Projector augmented-wave method. Phys. Rev. B, **50**:17953–17979 (Dec 1994).

[62] G. Kresse and D. Joubert. From ultrasoft pseudopotentials to the projector augmented-wave method. Phys. Rev. B, **59**:1758–1775 (Jan 1999).

[63] C. Rostgaard. The projector augmented-wave method. arXiv preprint arXiv:0910.1921.

[64] H. J. Monkhorst and J. D. Pack. Special points for Brillouin-zone integrations. Phys. Rev. B, **13**:5188–5192 (Jun 1976).

[65] M. Methfessel and A. T. Paxton. High-precision sampling for Brillouin-zone integration in metals. Phys. Rev. B, **40**:3616–3621 (Aug 1989).

[66] P. E. Blöchl, O. Jepsen, and O. K. Andersen. Improved tetrahedron method for Brillouin-zone integrations. Phys. Rev. B, **49**:16223–16233 (Jun 1994).

[67] F. Giustino. Electron-phonon interactions from first principles. ArXiv e-prints (March 2016).

[68] G. Czycholl. Theoretische Festkörperphysik: von den klassischen Modellen zu modernen Forschungsthemen. Springer-Verlag (2013).

[69] S. de Gironcoli. Lattice dynamics of metals from density-functional perturbation theory. Phys. Rev. B, **51**:6773–6776 (Mar 1995).

[70] P. B. Allen and R. C. Dynes. Transition temperature of strong-coupled superconductors reanalyzed. Phys. Rev. B, **12**:905–922 (Aug 1975).

[71] W. L. McMillan. Transition Temperature of Strong-Coupled Superconductors. Phys. Rev., **167**:331–344 (Mar 1968).

[72] E. R. Margine and F. Giustino. Anisotropic Migdal-Eliashberg theory using Wannier functions. Phys. Rev. B, **87**:024505 (Jan 2013).

[73] E. R. Margine and F. Giustino. Two-gap superconductivity in heavily n-doped graphene: *Ab initio* Migdal-Eliashberg theory. Phys. Rev. B, **90**:014518 (Jul 2014).

[74] M. Lüders, M. A. L. Marques, N. N. Lathiotakis, A. Floris, G. Profeta, L. Fast, A. Continenza, S. Massidda, and E. K. U. Gross. *Ab initio* theory of superconductivity. I. Density functional formalism and approximate functionals. Phys. Rev. B, **72**:024545 (Jul 2005).

[75] M. A. L. Marques, M. Lüders, N. N. Lathiotakis, G. Profeta, A. Floris, L. Fast, A. Continenza, E. K. U. Gross, and S. Massidda. *Ab initio* theory of superconductivity. II. Application to elemental metals. Phys. Rev. B, **72**:024546 (Jul 2005).

[76] H. Bruus and K. Flensberg. Many-body quantum theory in condensed matter physics: an introduction. Oxford University Press (2004).

[77] A. Migdal. Interaction between electrons and lattice vibrations in a normal metal. Sov. Phys. JETP, **7**(6):996–1001 (1958).

[78] F. Marsiglio and J. P. Carbotte. Electron-Phonon Superconductivity, pages 73–162. Springer Berlin Heidelberg, Berlin, Heidelberg (2008). ISBN 978-3-540-73253-2.

[79] Y. Nambu. Quasi-Particles and Gauge Invariance in the Theory of Superconductivity. Phys. Rev., **117**:648–663 (Feb 1960).

[80] D. J. Scalapino, J. R. Schrieffer, and J. W. Wilkins. Strong-Coupling Superconductivity. I. Phys. Rev., **148**:263–279 (Aug 1966).

[81] W. E. Pickett. Generalization of the theory of the electron-phonon interaction: Thermodynamic formulation of superconducting- and normal-state properties. Phys. Rev. B, **26**:1186–1207 (Aug 1982).

[82] F. Han. A Modern Course in the Quantum Theory of Solids. World Scientific Publishing Co. Pte. Ltd. (2012).

[83] G. A. Ummarino. 13 Eliashberg Theory. Emergent Phenomena in Correlated Matter: Autumn School Organized by the Forschungszentrum Jülich and the German Research School for Simulation Sciences at Forschungszentrum Jülich 23-27 September 2013; Lecture Notes of the Autumn School Correlated Electrons 2013, **3** (2013).

[84] P. B. Allen and B. Mitrović. Theory of Superconducting Tc. volume 37 of Solid State Physics, pages 1 – 92. Academic Press (1983).

[85] G. D. Mahan. Many-particle physics. Springer Science & Business Media (2013).

[86] P. Morel and P. W. Anderson. Calculation of the Superconducting State Parameters with Retarded Electron-Phonon Interaction. Phys. Rev., **125**:1263–1271 (Feb 1962).

[87] P. B. Allen. Neutron Spectroscopy of Superconductors. Phys. Rev. B, **6**:2577–2579 (Oct 1972).

[88] S. Y. Savrasov and D. Y. Savrasov. Electron-phonon interactions and related physical properties of metals from linear-response theory. Phys. Rev. B, **54**:16487–16501 (Dec 1996).

[89] S. Y. Savrasov. Linear-response theory and lattice dynamics: A muffin-tin-orbital approach. Phys. Rev. B, **54**:16470–16486 (Dec 1996).

[90] J. P. Carbotte. Properties of boson-exchange superconductors. Rev. Mod. Phys., **62**:1027–1157 (Oct 1990).

[91] M. Calandra and F. Mauri. Theoretical Explanation of Superconductivity in C_6Ca. Phys. Rev. Lett., **95**:237002 (Nov 2005).

[92] J. Kortus, I. I. Mazin, K. D. Belashchenko, V. P. Antropov, and L. L. Boyer. Superconductivity of Metallic Boron in MgB_2. Phys. Rev. Lett., **86**:4656–4659 (May 2001).

[93] A. D. Becke and K. E. Edgecombe. A simple measure of electron localization in atomic and molecular systems. The Journal of Chemical Physics, **92**(9) (1990).

[94] E. Räsänen, A. Castro, and E. K. U. Gross. Electron localization function for two-dimensional systems. Phys. Rev. B, **77**:115108 (Mar 2008).

[95] T. Burnus, M. A. L. Marques, and E. K. U. Gross. Time-dependent electron localization function. Phys. Rev. A, **71**:010501 (Jan 2005).

[96] A. Savin. The electron localization function (ELF) and its relatives: interpretations and difficulties. Journal of Molecular Structure, **727**(1–3):127 – 131 (2005). ISSN 0166-1280. Dedicated to Ramon Carbo´-Dorca on the Occasion of his 65th Birthday.

[97] J. Pannetier, J. Bassas-Alsina, J. Rodriguez-Carvajal, and V. Caignaert. Prediction of crystal structures from crystal chemistry rules by simulated annealing. Nature, **346**(6282):343–345 (1990).

[98] R. Martoňák, D. Donadio, A. R. Oganov, and M. Parrinello. Crystal structure transformations in SiO2 from classical and ab initio metadynamics. Nature materials, **5**(8):623–626 (2006).

[99] R. Martoňák, A. Laio, M. Bernasconi, C. Ceriani, P. Raiteri, F. Zipoli, and M. Parrinello. Simulation of structural phase transitions by metadynamics. Zeitschrift für Kristallographie-Crystalline Materials, **220**(5/6):489–498.

[100] Y. Wang, J. Lv, L. Zhu, and Y. Ma. Crystal structure prediction via particle-swarm optimization. Phys. Rev. B, **82**:094116 (Sep 2010).

[101] M. Amsler and S. Goedecker. Crystal structure prediction using the minima hopping method. The Journal of chemical physics, **133**(22):224104 (2010).

[102] B. Rost and C. Sander. Combining evolutionary information and neural networks to predict protein secondary structure. Proteins: Structure, Function, and Bioinformatics, **19**(1):55–72 (1994).

[103] A. R. Oganov and C. W. Glass. Evolutionary crystal structure prediction as a tool in materials design. Journal of Physics: Condensed Matter, **20**(6):064210 (2008).

[104] S. M. Woodley, P. D. Battle, J. D. Gale, and C. Richard A. Catlow. The prediction of inorganic crystal structures using a genetic algorithm and energy minimisation. Phys. Chem. Chem. Phys., **1**:2535–2542 (1999).

[105] N. L. Abraham and M. I. J. Probert. A periodic genetic algorithm with real-space representation for crystal structure and polymorph prediction. Phys. Rev. B, **73**:224104 (Jun 2006).

[106] E.-W. Lameijer, T. Bäck, J. N. Kok, and A. P. Ijzerman. Evolutionary algorithms in drug design. Natural Computing, **4**(3).

[107] Y. Ma, M. Eremets, A. R. Oganov, Y. Xie, I. Trojan, S. Medvedev, A. O. Lyakhov, M. Valle, and V. Prakapenka. Transparent dense sodium. Nature, **458**(7235):182–185 (2009).

[108] D. Duan, X. Huang, F. Tian, D. Li, H. Yu, Y. Liu, Y. Ma, B. Liu, and T. Cui. Pressure-induced decomposition of solid hydrogen sulfide. Phys. Rev. B, **91**:180502 (May 2015).

[109] A. R. Oganov. Modern methods of crystal structure prediction. John Wiley & Sons (2011).

[110] M. Valle and A. R. Oganov. Crystal fingerprint space – a novel paradigm for studying crystal-structure sets. Acta Crystallographica Section A, **66**(5):507–517 (Sep 2010).

[111] A. O. Lyakhov, A. R. Oganov, H. T. Stokes, and Q. Zhu. New developments in evolutionary structure prediction algorithm {USPEX}. Computer Physics Communications, **184**(4):1172 – 1182 (2013). ISSN 0010-4655.

[112] A. R. Oganov and M. Valle. How to quantify energy landscapes of solids. The Journal of chemical physics, **130**(10):104504 (2009).

[113] A. O. Lyakhov, A. R. Oganov, and M. Valle. How to predict very large and complex crystal structures. Computer Physics Communications, **181**(9):1623 – 1632 (2010). ISSN 0010-4655.

[114] A. Rogers and A. Prugel-Bennett. Genetic drift in genetic algorithm selection schemes. IEEE Transactions on Evolutionary Computation, **3**(4):298–303 (Nov 1999). ISSN 1089-778X.

[115] S. Roy, S. Goedecker, and V. Hellmann. Bell-Evans-Polanyi principle for molecular dynamics trajectories and its implications for global optimization. Phys. Rev. E, **77**:056707 (May 2008).

[116] G. Trimarchi, A. J. Freeman, and A. Zunger. Predicting stable stoichiometries of compounds via evolutionary global space-group optimization. Phys. Rev. B, **80**:092101 (Sep 2009).

[117] Q. Zhu, A. R. Oganov, and X.-F. Zhou. Crystal Structure Prediction and Its Application in Earth and Materials Sciences, pages 223–256. Springer International Publishing, Cham (2014). ISBN 978-3-319-05774-3.

[118] K. Kádas, L. Vitos, B. Johansson, and R. Ahuja. Stability of body-centered cubic iron–magnesium alloys in the Earth's inner core. Proceedings of the National Academy of Sciences, **106**(37):15560–15562 (2009).

[119] A. Jayaraman. Diamond anvil cell and high-pressure physical investigations. Rev. Mod. Phys., **55**:65–108 (Jan 1983).

[120] L. Dubrovinsky, N. Dubrovinskaia, E. Bykova, M. Bykov, V. Prakapenka, C. Prescher, K. Glazyrin, H.-P. Liermann, M. Hanfland, M. Ekholm, et al.. The most incompressible metal osmium at static pressures above 750 gigapascals. Nature, **525**(7568):226–229 (2015).

[121] F. Birch. Finite Elastic Strain of Cubic Crystals. Phys. Rev., **71**:809–824 (Jun 1947).

[122] F. D. Murnaghan. The Compressibility of Media under Extreme Pressures. Proceedings of the National Academy of Sciences of the United States of America, **30**(9):244–247 (1944). ISSN 00278424.

[123] Y. Ma, A. R. Oganov, and Y. Xie. High-pressure structures of lithium, potassium, and rubidium predicted by an *ab initio* evolutionary algorithm. Phys. Rev. B, **78**:014102 (Jul 2008).

[124] R. Steudel and B. Eckert. Solid Sulfur Allotropes Sulfur Allotropes, pages 1–80. Springer Berlin Heidelberg, Berlin, Heidelberg (2003). ISBN 978-3-540-44855-6.

[125] O. Degtyareva, E. Gregoryanz, M. Somayazulu, H.-k. Mao, and R. J. Hemley. Crystal structure of the superconducting phases of S and Se. Phys. Rev. B, **71**:214104 (Jun 2005).

[126] O. Degtyareva, E. Gregoryanz, H. Mao, and R. Hemley. Crystal structure of sulfur and selenium at pressures up to 160 GPa. High Pressure Research, **25**(1):17–33 (2005).

[127] O. Zakharov and M. L. Cohen. Theory of structural, electronic, vibrational, and superconducting properties of high-pressure phases of sulfur. Phys. Rev. B, **52**:12572–12578 (Nov 1995).

[128] E. Gregoryanz, V. V. Struzhkin, R. J. Hemley, M. I. Eremets, H.-k. Mao, and Y. A. Timofeev. Superconductivity in the chalcogens up to multimegabar pressures. Phys. Rev. B, **65**:064504 (Jan 2002).

[129] R. D. Eithiraj, G. Jaiganesh, G. Kalpana, and M. Rajagopalan. First-principles study of electronic structure and ground-state properties of alkali-metal sulfides – Li2S, Na2S, K2S and Rb2S. physica status solidi (b), **244**(4):1337–1346 (2007). ISSN 1521-3951.

[130] A. Vegas, A. Grzechnik, K. Syassen, I. Loa, M. Hanfland, and M. Jansen. Reversible phase transitions in Na_2S under pressure: a comparison with the cation array in Na_2SO_4. Acta Crystallographica Section B, **57**(2):151–156 (Apr 2001).

[131] A. Vegas, A. Grzechnik, M. Hanfland, C. Mühle, and M. Jansen. Antifluorite to Ni2In-type phase transition in {K2S} at high pressures. Solid State Sciences, **4**(8):1077 – 1081 (2002). ISSN 1293-2558.

[132] A. Lazicki, C.-S. Yoo, W. J. Evans, and W. E. Pickett. Pressure-induced antifluorite-to-anticotunnite phase transition in lithium oxide. Phys. Rev. B, **73**:184120 (May 2006).

[133] A. Lazicki, B. Maddox, W. J. Evans, C.-S. Yoo, A. K. McMahan, W. E. Pickett, R. T. Scalettar, M. Y. Hu, and P. Chow. New Cubic Phase of Li_3N: Stability of the N^{3-} Ion to 200 GPa. Phys. Rev. Lett., **95**:165503 (Oct 2005).

[134] U. Schwarz, A. Grzechnik, K. Syassen, I. Loa, and M. Hanfland. Rubidium-IV: A High Pressure Phase with Complex Crystal Structure. Phys. Rev. Lett., **83**:4085–4088 (Nov 1999).

[135] S. Giardino. Angular invariant quantum mechanics in arbitrary dimension. Revista Brasileira de Ensino de FÃsica, **35**:1 – 7 (09 2013). ISSN 1806-1117.

[136] C. J. Pickard and R. J. Needs. Predicted Pressure-Induced *s*-Band Ferromagnetism in Alkali Metals. Phys. Rev. Lett., **107**:087201 (Aug 2011).

[137] P. Giannozzi, S. Baroni, N. Bonini, M. Calandra, R. Car, C. Cavazzoni, D. Ceresoli, G. L. Chiarotti, M. Cococcioni, I. Dabo, A. D. Corso, S. de Gironcoli, S. Fabris, G. Fratesi, R. Gebauer, U. Gerstmann, C. Gougoussis, A. Kokalj, M. Lazzeri, L. Martin-Samos, N. Marzari, F. Mauri, R. Mazzarello, S. Paolini, A. Pasquarello, L. Paulatto, C. Sbraccia, S. Scandolo, G. Sclauzero, A. P. Seitsonen, A. Smogunov, P. Umari, and R. M. Wentzcovitch. QUANTUM ESPRESSO: a modular and open-source software project for quantum simulations of materials. Journal of Physics: Condensed Matter, **21**(39):395502 (2009).

[138] A. M. Rappe, K. M. Rabe, E. Kaxiras, and J. D. Joannopoulos. Optimized pseudopotentials. Phys. Rev. B, **41**:1227–1230 (Jan 1990).

[139] A. J. Flores-Livas, A. Sanna, and K. E. Gross. High temperature superconductivity in sulfur and selenium hydrides at high pressure. The European Physical Journal B, **89**(3):1–6 (2016). ISSN 1434-6036.

[140] Y. Li, L. Wang, H. Liu, Y. Zhang, J. Hao, C. J. Pickard, J. R. Nelson, R. J. Needs, W. Li, Y. Huang, I. Errea, M. Calandra, F. Mauri, and Y. Ma. Dissociation products and structures of solid H_2S at strong compression. Phys. Rev. B, **93**:020103 (Jan 2016).

[141] R. Akashi, M. Kawamura, S. Tsuneyuki, Y. Nomura, and R. Arita. First-principles study of the pressure and crystal-structure dependences of the superconducting transition temperature in compressed sulfur hydrides. Phys. Rev. B, **91**:224513 (Jun 2015).